MICROCOPY RESOLUTION TEST CHART

NATIONAL BUREAU OF STANDARDS 1964 A

AD-A156 632

AFWAL-TR-84-4172

EXPLORATORY DEVELOPMENT FOR A HIGH
RELIABILITY FLAW CHARACTERIZATION MODULE

G. J. Gruber, G. J. Hendrix, T. A. Mueller
Southwest Research Institute
6220 Culebra Road
San Antonio, TX 78284

March 1985

FINAL REPORT FOR PERIOD 31 AUGUST 1981 - 31 JANUARY 1985

Approved for Public Release; Distribution Unlimited

DTIC
ELECTE
JUL 1 5 1985
B

MATERIALS LABORATORY
AIR FORCE WRIGHT AERONAUTICAL LABORATORIES
AIR FORCE SYSTEMS COMMAND
WRIGHT-PATTERSON AIR FORCE BASE, OHIO 45433

REPORT DOCUMENTATION PAGE		READ INSTRUCTIONS BEFORE COMPLETING FORM
1. REPORT NUMBER AFWAL-TR-84-4172	2. GOVT ACCESSION NO. AD-A156 632	3. RECIPIENT'S CATALOG NUMBER
4. TITLE *(and Subtitle)* EXPLORATORY DEVELOPMENT FOR A HIGH RELIABILITY FLAW CHARACTERIZATION MODULE		5. TYPE OF REPORT & PERIOD COVERED Final Report for Period 31 Aug 81 – 31 Jan 85
		6. PERFORMING ORG. REPORT NUMBER
7. AUTHOR(s) George J. Gruber Gary J. Hendrix Theodore A. Mueller		8. CONTRACT OR GRANT NUMBER(s) F33615-81-C-5066
9. PERFORMING ORGANIZATION NAME AND ADDRESS Southwest Research Institute 6220 Culebra Road San Antonio, Texas 78284		10. PROGRAM ELEMENT, PROJECT, TASK AREA & WORK UNIT NUMBERS P.E. 62102F Proj. 2418, Task 05, WU24
11. CONTROLLING OFFICE NAME AND ADDRESS Materials Laboratory (AFWAL/MLLP) Air Force Wright Aeronautical Laboratories (AFSC) Wright-Patterson Air Force Base, Ohio 45433		12. REPORT DATE March 1985
		13. NUMBER OF PAGES 154
14. MONITORING AGENCY NAME & ADDRESS*(if different from Controlling Office)*		15. SECURITY CLASS. *(of this report)* Unclassified
		15a. DECLASSIFICATION/DOWNGRADING SCHEDULE

16. DISTRIBUTION STATEMENT *(of this Report)*

Approved for Public Release; Distribution Unlimited

17. DISTRIBUTION STATEMENT *(of the abstract entered in Block 20, if different from Report)*

18. SUPPLEMENTARY NOTES

19. KEY WORDS *(Continue on reverse side if necessary and identify by block number)*

Nondestructive evaluation, quantitative flaw characterization, ultrasonic scattering, Born inversion, internal bulk flaws, satellite pulses

20. ABSTRACT *(Continue on reverse side if necessary and identify by block number)*

Two sets of ultrasonic characterization procedures were applied under blind test conditions to 42 manufacturing flaws (inclusions and voids) embedded in titanium and IN100 alloy specimens. The Born inversion procedures (BIP) resulted in size estimates that were independent of not only flaw composition, but also shape, size, and orientation. Instead, the Born diameters were determined to be directly related to the period of the incident wave. For this

reason, the BIP results could not be reproduced with different transducers. The Born inversion algorithm correctly treats the first half-cycle of the impulse response of a volumetric flaw as the front-surface echo, but mistakes its third half-cycle for a back-surface echo (internal satellite pulse) or a creeping-wave return (external satellite pulse).

The characterization procedures based on the satellite-pulse observation technique (SPOT) proved to be insensitive to the period of the employed high-frequency transducers and, as expected, the practically constant separation between the front-surface echo and the satellite pulse was found to be directly related to flaw size. Semiautomated satellite analysis procedures (SSAP) that waive the requirement for a highly trained ultrasonic examiner were developed and qualified on 32 test flaws.

DTIC
ELECTE
JUL 1 5 1985

B

Accession For

NTIS GRA&I
DTIC TAB
Unannounced
Justification

By
Distribution/
Availability Codes
Avail and/or
Dist   Special

A-1

SUMMARY

This report presents results of measurements and calculations on backscattering of intermediate- and high-frequency ultrasonic waves by 42 voids and inclusions embedded in titanium and IN100 alloys. The primary program objective was to evaluate the Born inversion technique (BIT) in the forms developed at the Ames Laboratory, Iowa State University, and the Rockwell Science Center against nternal bulk flaws under simulated field conditions.

The program consisted of five tasks. The first task was the adaptation of the Born inversion software and testing of the assembled hardware system using the adapted software on flaws with known characteristics. The second task involved the fabrication by Pratt & Whitney Aircraft Group of titanium alloy and powder metallurgy nickel-based superalloy test specimens containing 40 volumetric flaws in the 250 to 1,300 μm size range. The third task included the development and qualification of two sets of flaw characterization procedures on the test flaws. The BIT was incorporated into the primary flaw characterization procedures along with the spectrum splicing technique (SST) that combines the backscattered amplitude data from the medium- and high-frequency regions to obtain quickly an indication of the appropriateness of a transducer for acquiring the waveforms for Born inversion. Prior to any metallographic sectioning, the test flaws were also characterized as to size, shape, and composition using procedures that incorporated the phase-comparison technique and the satellite-pulse observation technique (SPOT). The final two tasks involved metallographic sectioning of three real manufacturing flaws and comparison of the BIT and SPOT size estimates with the nominal/actual flaw dimensions.

It is concluded that multiple measurements made with waves of different mode, incidence angle, and dominant frequency and no less than three physical models for flaw-ultrasound interactions (one for voids and the other two for weakly and strongly scattering inclusions) are necessary to solve the inverse problem for flaw type and size in an unambiguous manner. Experiments with known flaws guided the model development efforts. The Born diameter estimates were determined to be independent of flaw composition, size, and shape, but linearly related to the period of the ultrasonic wave. The BIT yielded size estimates with barely acceptable accuracy for those voids and inclusions for which a transducer with a center frequency near the periodicity of the flaw's magnitude spectrum was available (coincidence rule). The BIT completely broke down, however, for 22 of the flaws in the IN100 test specimens because these flaws could not be detected by more than one transducer. The coincidence rule was violated for most of these flaws.

External satellite pulses originating from the waves that circumnavigated the flaws were observed for each flaw. Additional (internal) satellite pulses, on the other hand, were observed only for the tungsten carbide inclusions in the titanium alloy specimens. The type and size of the flaws were determined by comparing the flaw "signatures" (time-domain responses) and flaw "profiles" (frequency-domain responses) to model

predictions. The sizing errors for the 36 detectable voids and inclusions in the diffusion-bonded specimens were such that merely 100 μm (4 mils) need to be added to the SPOT estimate in order to be almost certain (i.e., 95 percent sure) that the actual flaw size does not exceed this conservative estimate. The SPOT size estimates were bracketed by the maximum linear dimensions of the three metallographically sectioned real flaws. Semiautomated satellite analysis procedures (SSAP) that waive the requirement for a highly trained ultrasonic examiner were developed and qualified on the 32 inclusions.

TABLE OF CONTENTS

TABLE OF CONTENTS (Cont'd)

TABLE OF CONTENTS (Concluded)

LIST OF ILLUSTRATIONS

LIST OF ILLUSTRATIONS (Cont'd)

LIST OF ILLUSTRATIONS (Cont'd)

LIST OF ILLUSTRATIONS (Cont'd)

LIST OF ILLUSTRATIONS (Cont'd)

LIST OF ILLUSTRATIONS (Concluded)

LIST OF TABLES

LIST OF TABLES (Concluded)

1. INTRODUCTION

1.1 Background

Turbine engine component life-extension technology now being developed under the name "retirement for cause" requires reliable and accurate ultrasonic techniques for characterizing material flaws as to type, size, location, shape, orientation, and composition. Ultrasonic techniques based solely on signal amplitude (i.e., the amplitude-comparison and amplitude-drop techniques) are incapable of characterizing flaws with the accuracy needed for component life prediction systems based on fracture mechanics. The limited capability of present-day ultrasonic techniques has become a barrier to the fulfillment of inspection requirements in a number of situations of interest to the Air Force. In situations where detailed information about a detected flaw could be used in component life extension, a Quantitative Ultrasonic Flaw Characterization Module would be a necessary supplement to the qualitative capability now available.

One objective of the Interdisciplinary Program for Quantitative Nondestructive Evaluation, established jointly by the Air Force Materials Laboratory (AFML) and the Defense Advanced Research Projects Agency (DARPA) in the mid-1970's, was to develop quantitative inspection techniques. Elements of this extensive development effort became available by 1980 for transition into production and depot ultrasonic inspection equipment. Two tasks remained, however, prior to reducing to practice the most mature of the inverse scattering algorithms developed under earlier AFML/DARPA contracts. The first task was to develop procedures featuring the Born inversion technique (BIT) supplemented by a transducer selection protocol. The second task was to qualify the Born inversion procedures (BIP) in the forms developed at Ames Laboratory (1) and Rockwell Science Center (2) against a statistically large set of simulated and real volumetric flaws (voids and inclusions). The Test Bed Program (2) resulted in a set of Born inversion procedures that requires a preliminary look at the modulated magnitude spectrum of the flaw H(f) to insure that the bandwidth of the transducer is centered on the portion of H(f) containing the first peak. These procedures were successfully applied to a natural flaw in a powder metallurgy nickel-based superalloy sample. In 1981, Southwest Research Institute (SwRI) initiated the Flaw Characterization Module Development Program to further test the Born inversion procedures against a large set of flaws under simulated field conditions.

1.2 Objectives

The first objective of the Flaw Characterization Module Program was to test the supplemented BIT on a large number of representative flaw types (not less than 40). Additionally, the approximate dimensions of the flaws were to be determined by at least one other nondestructive means ("second method") prior to any metallographic sectioning. The second objective was to implement the BIP, if proven valid, in a module compatible with state-of-the-art ultrasonic equipment.

1

1.3 Program Tasks

The first objective of the program was accomplished in five tasks. A flow diagram of the work performed to qualify the BIP for simulated and real internal bulk flaws is shown in Figure 1. Task 1 consisted of data acquisition, storage, and processing system ("hardware") assembly; zero-of-time algorithm, Born inversion algorithm, and transducer selection protocol ("software") adaptation; and functional testing of the hardware-software combination using spherical voids of known size in standard specimens. Task 2 involved the fabrication of test specimens of typical aircraft engine materials containing at least 40 isolated bulk flaws with characteristics unknown to the ultrasonic examiners. Task 3 consisted of adaptation and further development of the BIP; testing of these procedures against the flaws fabricated or collected during Task 2; and application of additional sizing techniques. After all ultrasonic examinations of the flaws in the test specimens were completed, half of the collected manufacturing (real) flaws were metallographically sectioned to determine the actual flaw characteristics (Task 4). Task 5 involved the comparison of the Born diameters and other size estimates to the nominal diameters of the flaws in the diffusion-bonded specimens and the actual dimensions of the sectioned real flaws detected in rejected parts. The second program objective was not accomplished because the Born diameter results indicated that it would be premature to construct a quantitative flaw characterization module.

1.4 Report Organization

The remaining part of the report summarizing the work accomplished during the program tasks and subtasks is divided into seven sections. Table 1 shows the organization of the report along the specific tasks and subtasks for ready reference.

Table 1

ORGANIZATION OF REPORT ALONG PROGRAM TASKS AND SUBTASKS

Task/Subtask and Title		Report Section and Title	
1.1	Technique Review	2.	Characterization Techniques
1.2	Software Transfer	3.	Software Transfer and Adapation
1.3	Hardware Assembly		
1.4	Software Adaptation		
1.5	Protocol Development	4.	Procedure Development
2.	Specimen Fabrication	5.	Test Specimens
3.	Protocol Testing	6.	Procedure Qualification
4.	Metallographic Sectioning	7.	Discussion
5.	Analysis of Results	8.	Summary
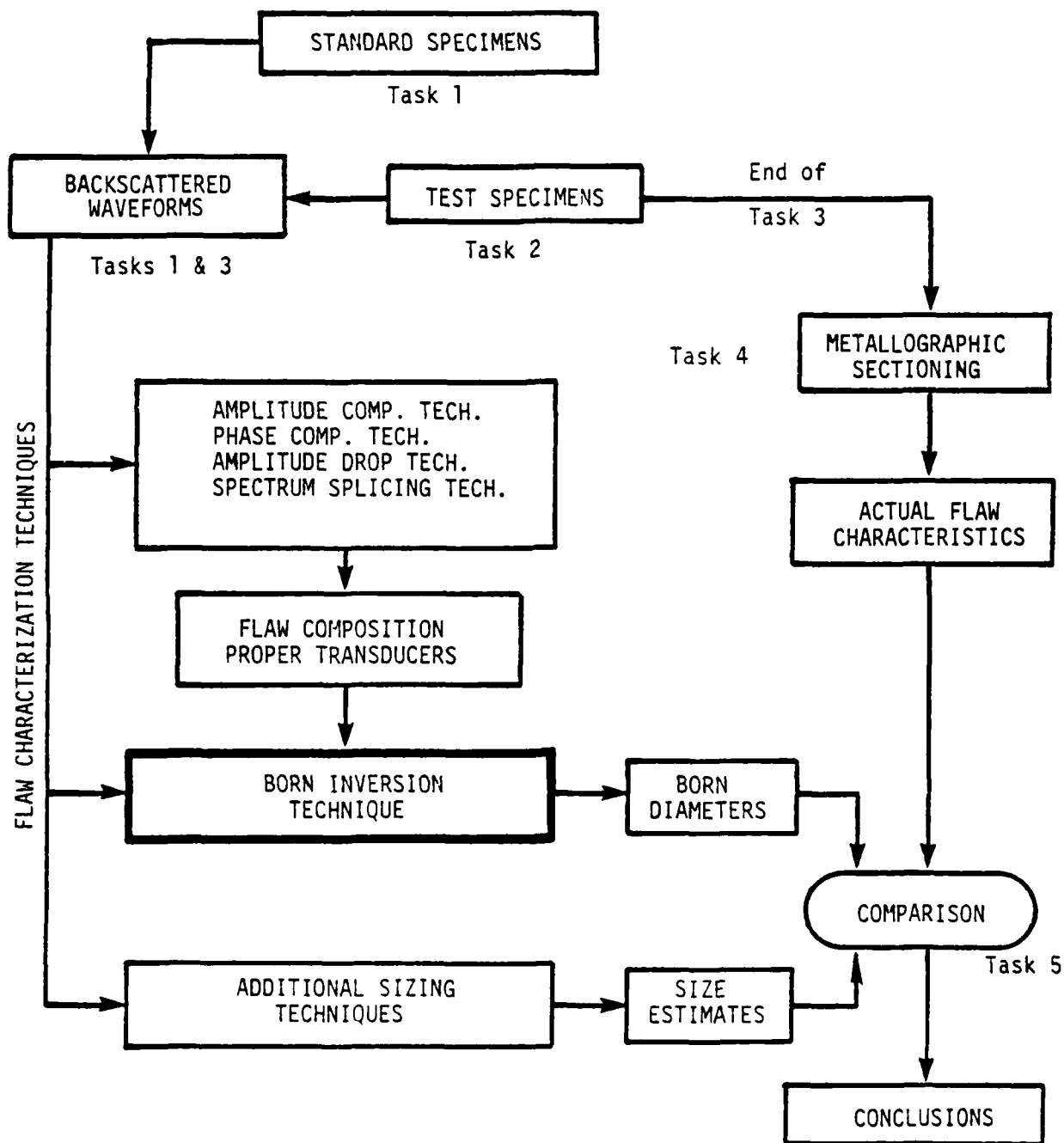
Figure 1.   Flow Diagram of Effort to Qualify the Supplemented Born
Inversion Technique (BIT) for Voids and Inclusions

2. FLAW CHARACTERIZATION TECHNIQUES

2.1   General

The inverse-scattering problem is an ill-posed mathematical problem (3,4). That is, flaws that differ significantly in size, shape, composition, etc., may produce backscattered waveforms y(t) that are essentially the same. To obtain reliable identification of flaw type and accurate estimates of flaw size, shape, orientation, and composition, this weakness of the inverse problem must be recognized and appropriately dealt with. Quantitative flaw definition requires a good understanding of the interaction of ultrasound with flaws of various characteristics. This interaction is modeled in Figure 2 for an inclusion-like (penetrable) flaw with smooth boundaries. The biggest challenge for inverse-scattering approaches to flaw characterization is the establishment of unambiguous cause-and-effect relationships among the fracture-related flaw characteristics (X_i, i=1, 2,...M) and the various extractable signal parameters (Y_j, j=1, 2,...N).

It is well known that both the frequency and angular distributions of the backscattered wave amplitudes $y_n(\vec{r},t)$ depend on the characteristics of the flaw. To solve the inverse problem, the distribution of the amplitudes of the backscattered waves must then be measured over a set of wave modes (longitudinal vs. shear), transducer center frequencies (medium vs. high), and beam angles. It follows that the inversion process sought is one that allows estimation of the ith flaw characteristic on the basis of just a few independent measurements (i.e., signal parameters).

If one knows a priori that the flaw is a spherical void, only one signal parameter needs to be extracted from y(t) to estimate the one unknown flaw characteristic (diameter). The number of flaw characteristics for a nonspherical inclusion, on the other hand, is no less than five. When M is large, determination of the effects of each X_i on a given signal parameter Y_j requires a combination of analytical, experimental, and statistical approaches. One cause (X_i) may have several effects (Y_j), and the same effect may be due to several causes.

The BIT is a method for estimating the geometrical characteristics (shape, size, and orientation) of internal bulk flaws and uses as input data the specularly reflected wave [$y_1(\cdot)$ in Figure 2(a)]. This technique needs supplementation not only in establishing the flaw's type and composition, but also in making sure that the transducer's bandwidth requirement (Born bandwidth, $0.5 \le ka \le 2.5$)* is met. The three amplitude and phase analysis techniques supplementing the BIT are described first. This is followed by discussions of the BIP (including a transducer selection protocol) and an additional sizing technique that, unlike the BIT, utilizes the trailing signals ("satellite pulses") resulting from the secondary backscattered waves [$y_2(\cdot)$ and $y_3(\cdot)$ in Figure 2(a)] in the estimation of flaw size.

---

*$k(=2\pi/\lambda)$ is wave number, $\lambda(=c/f)$ is wavelength, c is sound velocity of host material, f is transducer center frequency, and a is flaw radius.

WAVES

w(·)

FLAW

$y_1(·)$

$y_2(·)$

$y_3(·)$

Backscattered Waves

w($\vec{r}$,t) Incident
$y_1(\vec{r}$,t) Reflected
$y_2(\vec{r}$,t) Internal
$y_3(\vec{r}$,t) External (Creeping)
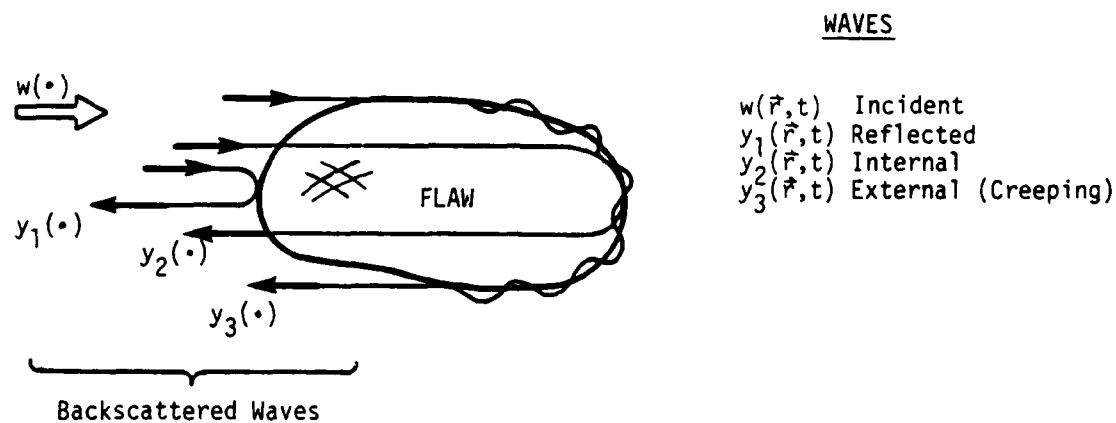
(a) Physical Model of Flaw-Ultrasound Interaction

FLAW   WAVEFORMS

w(t)   w(t) Reference
                                        y(t) Flaw
H(f)   y(t)

Causes -   Effects -
Flaw Characteristics X_i Signal Parameters Y_j
i = 1, 2,...M   j = 1, 2,...N
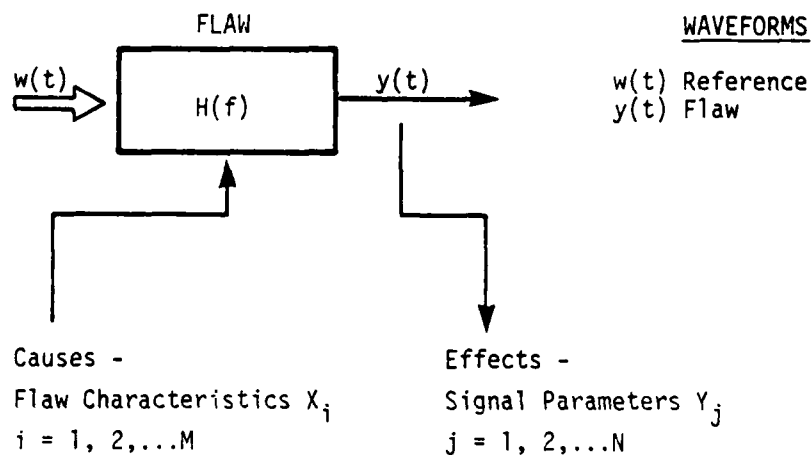
(b) Linear System Model of Flaw-Ultrasound Interaction

Figure 2. Models for Predicting the Response of a Penetrable
           Volumetric Flaw to Ultrasound

5

2.2 Amplitude-Comparison Technique

Analysis of the maximum amplitude of the rectified flaw waveform $|y(t)|$ is most useful for flaw detection. The size of flaws that are small compared to the wavelength (ka<0.5, Rayleigh region) can be estimated by the amplitude-comparison technique. However, even in the Rayleigh region, the maximum signal amplitude depends strongly on flaw composition. Only in very favorable circumstances will the maximum signal amplitude bear an unambiguous relationship to flaw size.

The amplitude-comparison technique is more reliable for distinguishing among voids and inclusions than for flaw sizing. It is known that, due to their internal waves, tungsten carbide and other weakly scattering inclusions exhibit consistently more structured "signatures" (time-domain responses) and more modulated "profiles" (frequency-domain responses) than voids (5,6). For a given void-transducer combination, the creeping-wave-to-reflected-wave amplitude ratio improves in going from longitudinal to shear waves (7).

2.3 Phase-Comparison Technique

This technique provides a more quantitative means than the amplitude-comparison technique of determining the flaw type and composition. Inclusions with a lower acoustic impedance Z* than that of the host material—void is a special case of this type of inclusion—can be readily distinguished from those inclusions that have a higher acoustic impedance than the host material by observing the phase of the specularly reflected pulse ["locomotive" of the pulse train (4,8,9,10)]. Additional flaw-composition information can be extracted from the signs of the satellite pulses ("trailers") accompanying the reflected pulse. This will be further discussed in Subsection 2.7.

2.4 Amplitude-Drop Technique

This technique is commonly used in the field for flaw sizing. When the largest dimension of an elongated, needle-like flaw exceeds that of the ultrasonic beam incident perpendicularly on it, there are generally not many sizing problems. The length of a 4-mm long natural inclusion was accurately estimated by the amplitude-drop technique using a focused transducer (2). The through-wall dimension of this flaw (about 140 ㎛) was, however, overestimated by a factor of 5 by the focused C-scan technique. The correlations were also poor for the size estimates obtained by the focused C-scan technique for the small inclusions (d<500 ㎛) in some titanium powder compacts (9).

2.5 Born Inversion Procedures

The BIT, credited to Rose and Krumhansl (11), requires a single waveform from an appropriate transducer to obtain a size estimate

---

*Z = ρc where ρ is the density of the inclusion.

(Born diameter D) corresponding to the projection of the flaw along the
direction of insonification. The transducer selection protocol features
the spectrum splicing technique. The shape and orientation of the flaw
may be estimated by moving the pulse-echo transducer around the flaw and
inverting the waveforms received from several directions or by using a
multi-viewing transducer (12).

The input to the Born inversion algorithm (BIA) consists of the pro-
perly time-shifted real part of the deconvolved flaw spectrum [A(f)]. A
deconvolution algorithm of the Wiener-filter type was derived to minimize
the effects of transducer and material properties on the output of the BIA
(i.e., the Born diameter). A zero-of-time algorithm (ZOTA) was adapted
for locating the center of the flaw along the observation direction. The
spectrum splicing technique and the three algorithms incorporated into the
BIP are described in the following paragraphs.

2.5.1 Transducer Selection Protocol

The most serious limitation of the BIT is the requirement
for a wideband ultrasonic transducer that is effective over the specific
0.5 to 2.5 ka range. This bandwidth requirement is at the limit of state-
of-the-art transducer technology. The limitation on the bandwidth dic-
tates the center frequency of the "proper" transducer (Born frequency) to
be

$$F = \frac{c(0.5 \times 2.5)^{\frac{1}{2}}}{\pi d} = \frac{2,200}{d} \tag{1}$$

where d is flaw diameter in μm, c = 6.1 km/sec for the titanium and IN100
alloys of interest, and F is in MHz. The transducer selection problem is
solved by examining the deconvolved flaw spectrum [magnitude spectrum H(f)]
obtained by using two or three longitudinal-wave transducers and splicing
the individual spectra together (2).

The spliced spectrum expected for a 1,000-μm diameter void is
shown in Figure 3 and that expected for a 500-μm diameter void is shown in
Figure 4. Note that the modulations of the theoretical magnitude spectra
are quite regular (10) and the frequency of the first peak is nearly equal
to p, the spectrum periodicity. Note also that to a good approximation
the product of p and d is a constant (2,200). It follows that the Born
frequency for a strongly scattering ("strong") flaw is given by the aver-
age periodicity of the composite magnitude spectrum obtained by splicing
together the individual spectra of two or three intermediate- and high-
frequency transducers. This is the essence of the spectrum splicing tech-
nique (SST). The bandwidth of the Born transducer not only must be suit-
ably large, but must also be centered on the first peak of H(f). It
follows from the generalization of this coincidence rule that the Born
frequency for a weakly scattering ("weak") flaw is given by 70 percent of
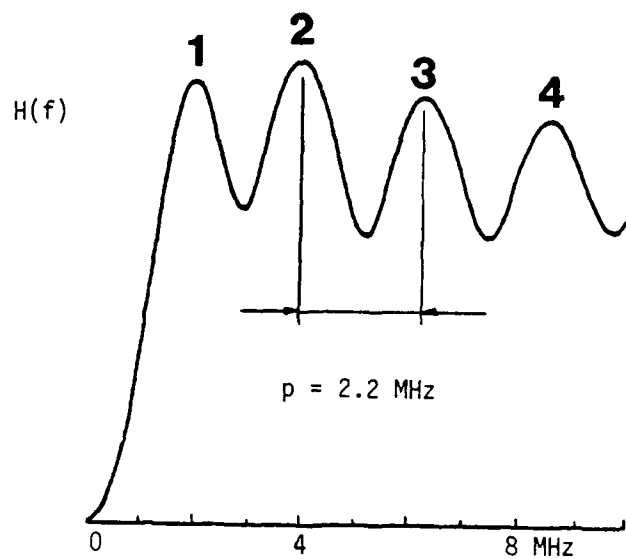
Figure 3.   Magnitude Spectrum Calculated for a 1,000-μm Diameter
Void in Titanium 6-4 or IN100
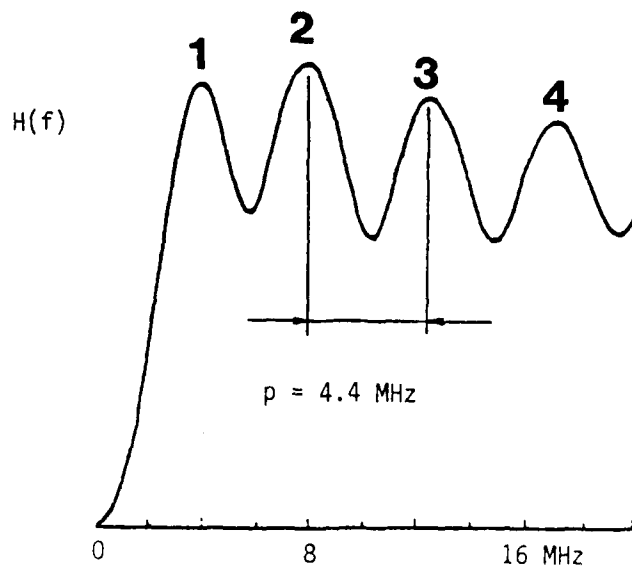
Figure 4.   Magnitude Spectrum Calculated for a 500-μm Diameter
Void in Titanium 6-4 or IN100

the periodicity of its spliced magnitude spectrum.*   In summary, the Born frequency is given by

$$F = \begin{cases} p \text{ for strong scatterers} \\ 0.7p \text{ for weak scatterers} \end{cases} \tag{2}$$

where p is the periodicity of the flaw's spliced magnitude spectrum.

2.5.2   Deconvolution Algorithm

Deconvolution to remove the effects of the data acquisition system from the flaw waveform y(t) is the first preprocessing step in the application of the BIT. All deconvolution algorithms are sensitive to noise. The deconvolution process can be performed in the frequency or the time domain. In a recently developed time-domain deconvolution algorithm (4), a trade-off is made between the ability to detect the trailing signals associated with the specularly reflected pulse (resolution) and insensitivity to material, electronic, and other types of noise. A Wiener-filter type deconvolution that is performed in the frequency domain is described. It follows from the system model of Figure 2(b) that, in the absence of noise, the flaw spectrum Y(f) is simply equal to the product of the flaw's transfer function H(f) and the reference spectrum W(f). The front or back surface of the test specimen containing the flaw is an acceptable reference reflector. A Wiener-filter type deconvolution algorithm of the form

$$H(f) = \frac{Y(f)\ W^*(f)}{|W(f)|^2 + Q^2}\ , \tag{3}$$

where the asterisk denotes complex conjugate and Q^2 is the average noise power density, can desensitize the results to the presence of noise at high and low frequencies where the transducer is inefficient. Pulse resolution can be traded for insensitivity to noise and vice versa in the selection of the Q parameter.

2.5.3   Zero-of-Time Algorithm

The deconvolved flaw spectrum that results from performing the operations required by Equation (3) is generally complex. The phase error $2\pi f \tau$ must be eliminated from H(f) before it can be input to the BIA. This requires shifting the impulse response h(t) by τ so that the centroid of the flaw is at t = 0. If the origin of time coincided with the time at which the fictitious pulse labeled C in Figure 5 returned from the center of the flaw (point Q_0), there would be no need for time shifting of h(t). If sufficient low-frequency (ka < 0.5) information was available, the required time shift could be determined by extrapolating the phase

---

*The 70 percent reflects the differences in velocities and travel paths between the externally scattered waves of a strong flaw and the internally scattered waves of a weak flaw [see Figure 2(a) for the travel path differences].

9
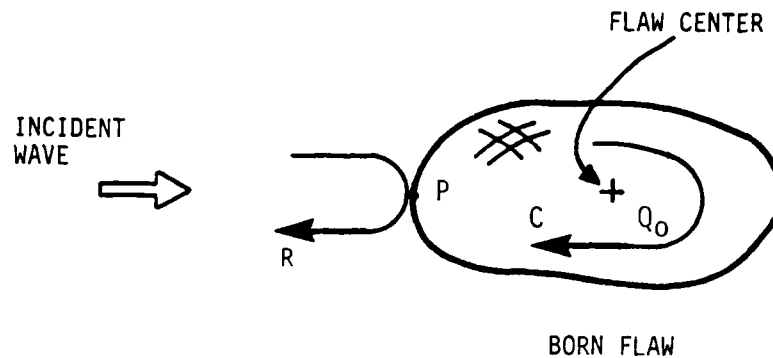
Figure 5. Physical Model for the Born Inversion Technique.
The reflected pulse (R) is real and the center
pulse (C) is fictitious.

spectrum to zero frequency. However, state-of-the-art Born transducers
(i.e., transducers centered at ka = 1.1) do not permit this extrapolation
process.

The method recommended by Ames Laboratory (1) was used in this pro-
gram to determine the zero of time for h(t). This method is based on the
premise that if H(f) contains a phase error of $2\pi f\tau$ then the peak of the
cross-sectional area function for the flaw a(z) is shifted from the proper
origin by $c\tau/2$. Figure 6 shows the cross-sectional area function and the
time-shifted impulse response obtained with a "proper" (F = 6 MHz) trans-
ducer for a 400 x 800 μm oblate spheroidal void in a titanium 6-4 specimen
(13). Note that the peak of a(z) and the peak of h(t) corresponding to
the C pulse (second half cycle) occur at the same location (i.e., at the
centroid of the impulse response) and have the same polarity. The first
half cycle of h(t) has the opposite polarity and is identified to be the R
pulse of Figure 5. The BIT reduces to a mere time-of-flight reconstruction
for the R pulse since it does not utilize the arrival time for the size-
information-carrying creeping wave (external satellite pulse S_e) clearly
seen in both y(t) and h(t) of Figure 6.

2.5.4   Born Inversion Algorithm

The one-dimensional BIA produces a characteristic function
J(r) from the real part of the flaw's transfer function A(k) according to
the inverse transformation

$$J(r) = \text{constant} \int_{k_{min}}^{k_{max}} A(k) \frac{\sin 2kr}{2kr} \, dk \qquad (4)$$

The characteristic function shown in Figure 6 has zero slope at the origin.
An estimate of the flaw radius (half of Born diameter D) can be obtained
from the characteristic function as the range at which J(r) drops to
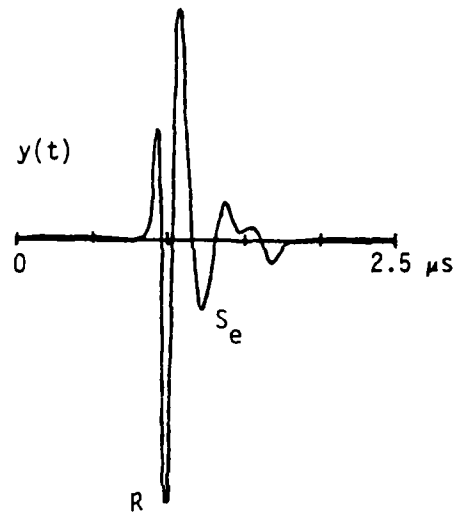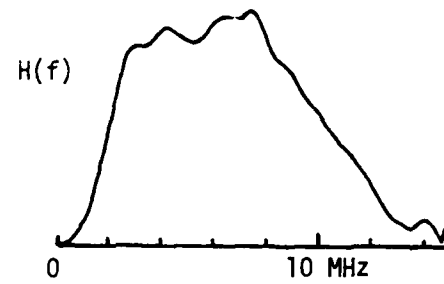
10
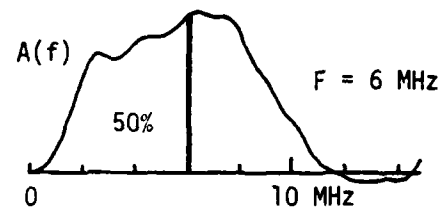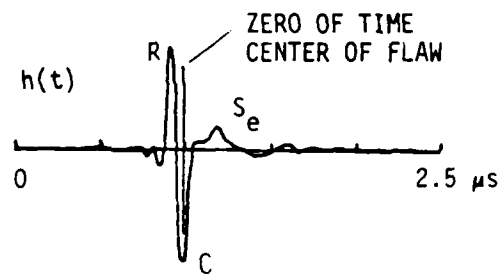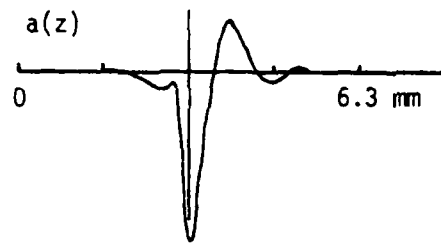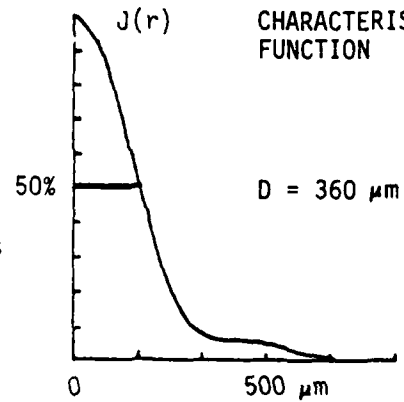
Figure 6. Born Inversion Results Obtained by Ames Laboratory
for a 400 x 800 μm Oblate Spheroidal Void

11

one half of its peak value. The Born diameter can also be calculated
according to the formula

$$D = 2 \; \frac{\text{Area under } J(r)}{\text{Peak value of } J(r)} \qquad (5)$$

Note that the product of the transducer center frequency (6 MHz) and the
Born diameter (360 ᵤm) is about 2,200 mHz. This agrees with the constant
of Equation (1).

2.6   Satellite-Pulse Observation Technique

Volumetric material flaws may be broadly classified as penetrable or
impenetrable (i.e., voids). Penetrable flaws may be divided into weak
flaws (Born-like inclusions) and strong flaws [Franz-like inclusions (14)].
The sketches on the left side of Figure 7 reveal the main differences in
the ultrasonic scattering mechanisms of voids, weak inclusions, and strong
inclusions. All types of volumetric flaws can, in principle, support tan-
gentially radiating Franz-type "creeping" waves as indicated by the wiggly
lines between the shadow boundary points Q_1 and Q_2 of the various flaws.
In addition to the externally scattered (S_e) waves, weak flaws can also
support internally scattered (S_i) waves resulting in a pair of satellite
pulses. The satellite-pulse observation technique (SPOT) is based on the
interpretation, in terms of flaw types and dimensions, of the separations
σ in time of arrival between the specularly reflected R pulse and its
generally ignored trailers (satellites S_i and S_e) contained in the flaw
waveform (15). The analytical and supporting experimental SPOT results
obtained for the three flaw types of interest are presented.

2.6.1   Physical Model for Voids

It is known that the small pulses launched in opposite direc-
tions (i.e., clockwise and counterclockwise) from the shadow boundaries of
a strong scatterer of convex shape travel in unison on the instrument
screen with the specularly reflected pulse (hence "satellite" pulses).
The upper diagrams in Figure 7 show the interaction of a high-frequency
longitudinal or shear wave with a void resulting in a reflected pulse (R)
and an externally scattered pulse (S_e). For clarity, only the clockwise
creeping wave is shown. Each time this creeping wave reaches point Q_2,
tangential reradiation in the form of a tangentially scattered wave from
the void during its circumvention is launched in the direction to be
received by the pulse-echo transducer. The separation of the first satel-
lite from the R pulse is given by

$$\sigma_e = \left(\frac{1}{c} + \frac{\pi}{2v} \right) d \qquad (6)$$

where v is the creeping-wave velocity. For longitudinal-wave (LW) inci-
dence, c = 6.1 km/sec and v is taken to be 0.87c for an average-sized
(800-ᵤm diameter standard) void insonified with a standard high-frequency
(5-MHz) transducer (16). Published creeping-wave velocities range from

12

VOID

IMPULSE RESPONSE

WEAK INCLUSION

STRONG INCLUSION
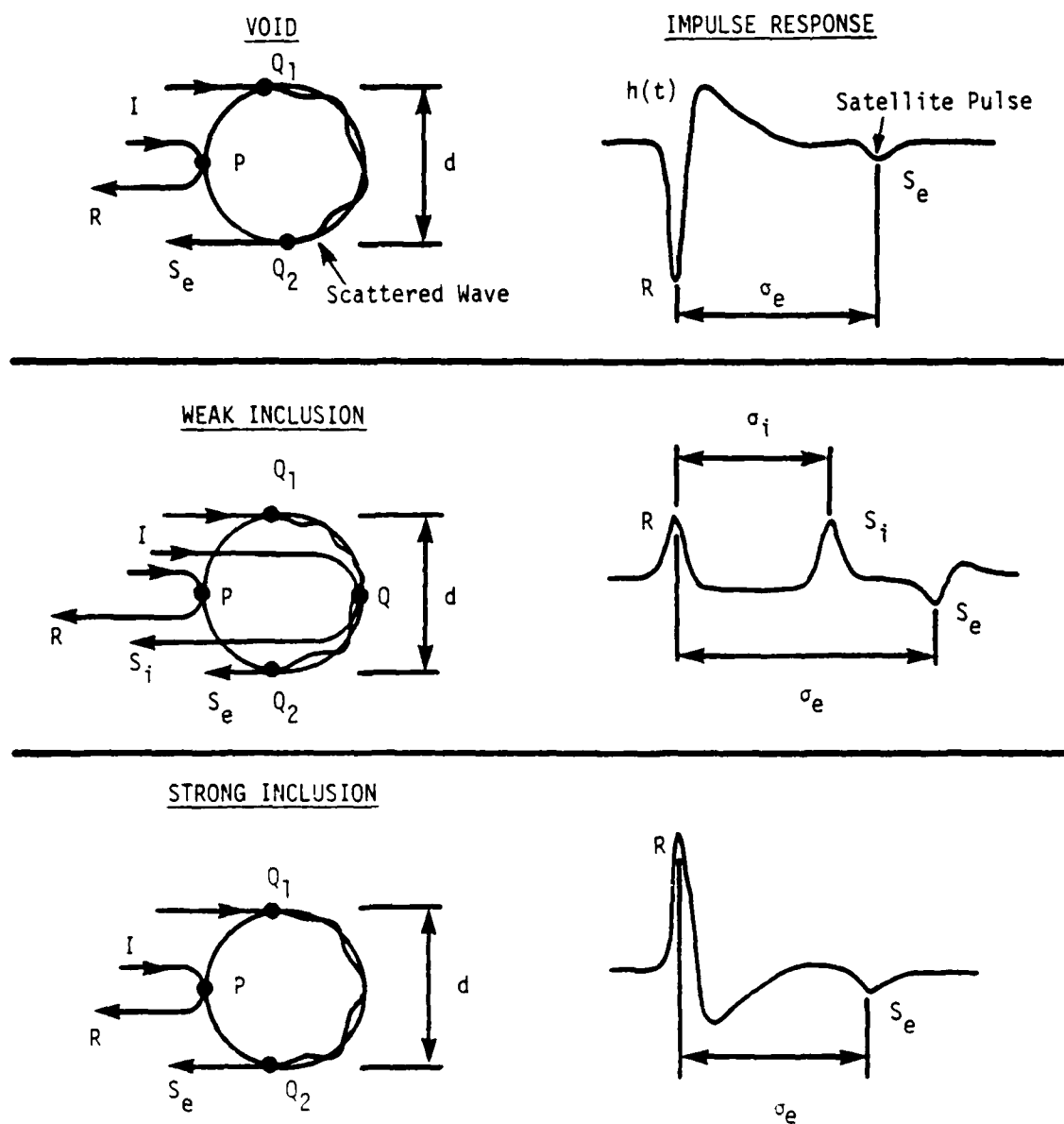
Figure 7. Physical Models for the Interaction of High-Frequency
Ultrasound With Volumetric Flaws Resulting in External
and/or Internal Scattered Waves and Satellite Pulses

13

0.80c to 0.95c (10, 17). The diameter of void-like flaws can be estimated on the basis of longitudinal-wave σ measurements by

$$d = 2.18 \, \sigma_e \qquad (7)$$

where d is in micrometers and σ_e is in nanoseconds.

For shear-wave (SW) incidence, c = 3.1 km/sec and v is equal to the Rayleigh wave velocity calculated to be 0.93c (15). On the basis of shear-wave σ measurements, the void diameter is estimated by

$$d = 1.15 \, \sigma_e \qquad (8)$$

where d is in micrometers and σ_e is in nanoseconds.

The composite waveforms obtained by interrogating a void of unknown size and shape (i.e., one of the test flaws) with high-frequency longitudinal and shear waves are reproduced in the upper diagrams of Figure 8. As expected, the separation of the SW satellite from the R pulse is nearly twice as large as that of the associated LW pulses. Note also that the reflected and the externally scattered pulses are of the same polarity. Both the leading and trailing pulses are negative because there is a drop in the acoustic impedance at the metal-void boundary.

2.6.2   Physical Model for Tungsten Carbide Inclusions

The waveform is much more structured when both externally and internally scattered waves are produced by an inclusion with sound velocities nearly the same as those of the host alloy matrix. It is well known that the back side of a tungsten carbide (WC) or other Born-like inclusion in a titanium alloy can act as an acoustic lens (10,18,19). Because of this focusing effect, the amplitude of the internally scattered pulse (S_i in the middle diagrams of Figures 7 and 8) can be comparable to that of the R pulse. The incident longitudinal wave (I in Figure 7) can propagate through the middle of a Born-like inclusion and be scattered from its back surface either as a longitudinal or a shear wave (18,20). The same mode-conversion phenomena can also be observed with incident shear waves (5). For longitudinal-wave incidence, the separation of the first satellite pulse (S_i) from the R pulse is given by 2d/c where c = 6.6 km/sec for a tungsten carbide inclusion. The diameter of a WC inclusion can be estimated on the basis of longitudinal-wave σ measurements by

$$d = 3.30 \, \sigma_i \qquad (9)$$

where d is in micrometers and σ_i is in nanoseconds.

It is known that longitudinal creeping waves can propagate not only on the surfaces of strong inclusions but also on the surfaces of weak inclusions (6,21,22). If observed, the separation of the second satellite pulse (S_e) from the R pulse may also be used, in accordance with

14
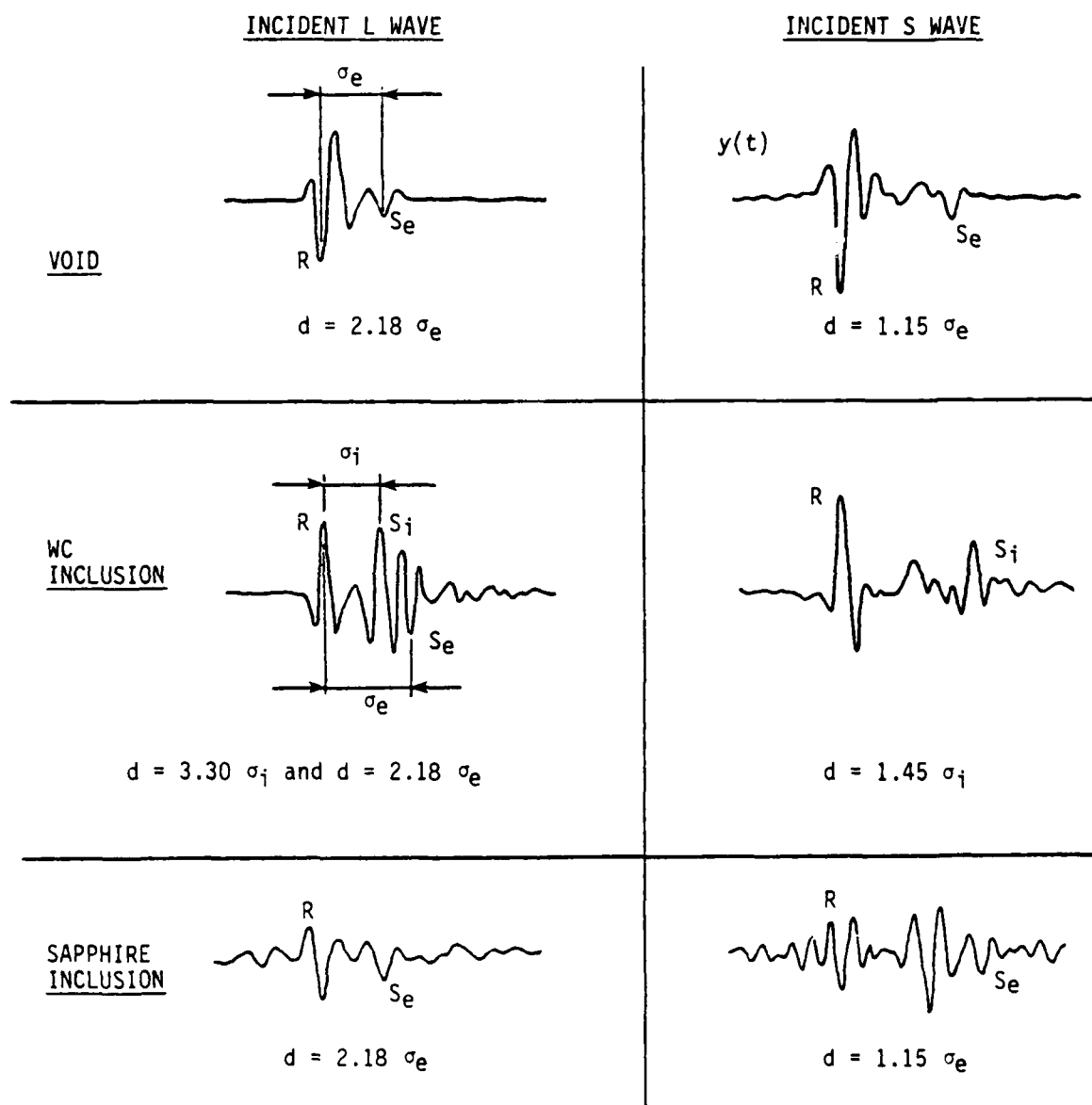
Figure 8. Analytical Models for the Estimation of Flaw Size d in Terms of Doublet Separations σ_e and σ_i Extracted From the Signatures of Three Test Flaws

Equation 7, to estimate the size of a WC inclusion. Because the density
of the WC inclusion is larger than that of the titanium alloy matrix, the
R pulse is expected to have a positive polarity. The S_i pulse has the
same polarity and the S_e pulse has the usual negative polarity.

Externally scattered (creeping) waves appear to be less
important when the WC inclusion is interrogated with a shear wave. The
handbook value for the shear-wave velocity of WC is 4 km/sec. However, in
one study of the scattering behavior of WC inclusions (10) the shear wave
velocity was allowed to vary between 2 and 4 km/sec. We decided to
determine the effective shear wave velocity from the shear-wave value of
σ_i (= 800 ns) measured for a WC test flaw and the diameter estimates
(1,160 μm and 1,180 μm) obtained for the same flaw from longitudinal-wave
σ measurements. This resulted in the desired inverse-scattering formula

$$d = 1.45 \ \sigma_i \tag{10}$$

where d is in micrometers and σ_i is in nanoseconds with an effective WC
shear-wave velocity of 2.9 km/sec.

2.6.3 Physical Model for Sapphire Inclusions

Sapphire inclusions are nearly impenetrable due to the magnitudes of their LW and SW velocities (10 km/sec and 6 km/sec, respectively)
relative to those of the IN100 alloy matrix. Except for the positive
polarity of the R pulse, the impulse response of a sapphire inclusion is
expected to resemble that of a void (see the lower and upper diagrams of
Figures 7 and 8). Equations 7 and 8 derived for voids are also valid for
sapphire inclusions.

3. SOFTWARE TRANSFER AND ADAPTATION

3.1 General

The main program objective was to independently evaluate the Born inversion software developed by others against a set of volumetric flaws under blind test conditions. To accomplish this objective, the existing software was transferred to SwRI and made operational with a newly assembled hardware system.

3.2 Software Transfer

To initiate the Born-inversion-software adaptation task, a subcontract was let to Ames Laboratory for (1) delivering the software to SwRI in a computer language suitable for the inversion of deconvolved and properly time-shifted waveforms obtained for each of the test flaws, and (2) assisting SwRI in making the Born inversion software operational with a newly assembled data acquisition and inversion system.

The Ames software package was transferred in two steps. First, the data-inversion computer program (BIA) for estimating the flaw's characteristic function and effective diameter was transferred in Fortran language. In the Ames data-processing computer program (ZOTA), the origin of time is chosen at the maximal cross-sectional area. The software transfer was completed in November 1981.

A time-domain deconvolution algorithm developed at the Air Force Institute of Technology (4) was also transferred to SwRI but was not used extensively after its equivalency to the existent Wiener-filter type deconvolution algorithm was established (23).

3.3 Data Acquisition and Inversion System

The hardware comprising the Data Acquisition and Inversion SYstem (DAISY) assembled for specimen testing is shown in Figure 9. This system is composed of off-the-shelf items (ultrasonic transducers, pulsers, receivers, etc.) and standard interfaces and connectors. It includes a data acquisition stage, a data storage capability, a data processing stage, and a data analysis (Born inversion) stage. These are described under two headings.

3.3.1 Data Acquisition System

The ultrasonic data were acquired using immersion and contact transducers. Because of the limited bandwidth of any transducer, three standard-frequency wideband transducers (nominal center frequencies of 2.25, 5, and 10 MHz) were made available so that at least one of the transducers would satisfy the $0.5 < ka < 2.5$ inequality for a test flaw known to be in the 250 to 1,300 um size range. The transducers were driven by a pulser-receiver unit made by Panametrics (Model 5055PR) that enables the

17

Figure 9. Block Diagram of Data Acquisition and Inversion System (DAISY)

DATA INVERSION

DATA ACQUISITION

MAIN COMPUTER

GRAPHIC TERMINAL

HARD COPY

BIT[4]

DESKTOP COMPUTER

HARD COPY

SST[2]

SSAP[3]

DIGITAL OSCILLOSCOPE

SPOT[1]

ULTRASONIC PULSER-RECEIVER

PULSE-ECHO TRANSDUCER

FLAW

TEST SPECIMEN
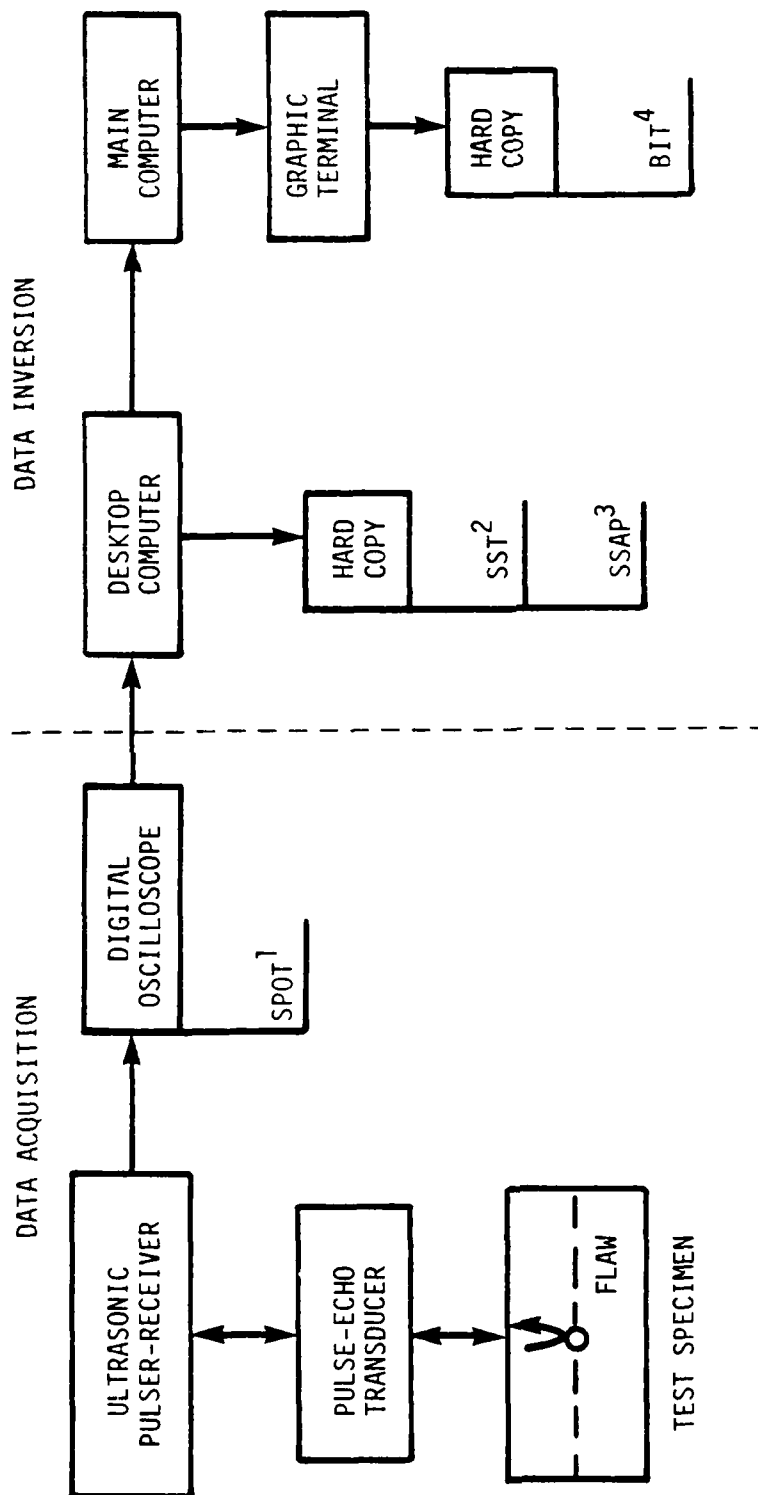
[1]SPOT = Satellite-Pulse Observation Technique
[2]SST = Spectrum Splicing Technique
[3]SSAP = Semiautomated Satellite Analysis Procedures
[4]BIT = Born Inversion Technique

18

transmission of short (three half-cycle) ultrasonic pulses into the test specimen. The receiver can provide up to 60 dB gain and 68 dB attenuation.

A digital oscilloscope made by Tektronics (Model 7854) was used to observe the received waveforms for σ (satellite pulse separation) measurements. The waveform analyzer of the oscilloscope digitizes selected portions (usually 2-μs long segments) of the radio-frequency (RF) waveforms and transfers the digitized data to a small (desktop) computer. Each waveform can be sampled up to 256 times within selectable time windows. Many samples were acquired and then averaged to minimize the background interference caused by random electronic noise.

3.3.2   Data Inversion System

The desktop computer for the DAISY is a Hewlett-Packard 85 and the main computer is a Data General Eclipse C-330. The desktop computer offers graphic capability, keyboard, and magnetic tape storage, all in a single portable unit located in the ultrasonics laboratory. The main functions of the HP-85 are to store the digitized waveforms and assist in selecting the most appropriate transducer(s) to acquire the data for Born inversion. The software package for the HP-85 includes programs for generating disk files, managing the data storage on disk, normalizing the flaw waveforms with the reference waveforms (deconvolution), and displaying the waveforms and the complex Fourier spectra (magnitude and phase or real and imaginary parts) on hard copies.

The Born inversion software from Ames Laboratory was executed on the Eclipse C-330 computer along with two deconvolution programs to ensure timely processing and Born inversion of the digitized waveforms. Several other waveform processing programs are resident in this computer, including time gating, Fourier transforming, low-frequency extrapolating, filtering, and time shifting. The signals in the digitized flaw waveforms (i.e, the main signal and any satellites captured in a record length of 2 microseconds) were software gated and Fourier transformed. The flaw waveforms were then deconvolved, time shifted, and put into the Born inversion algorithm. Hard copies of the Born inversion results of the type displayed in Figure 6 were obtained for each test flaw.

3.4   Software Adaptation

The SwRI software-hardware combination was tested against the Ames combination using an 800 μm diameter void ("standard flaw," 2,4,23-25). The experimental protocol for obtaining the Born diameter for an internal bulk flaw was established under the guidance of Ames Laboratory (1,26). This protocol consists of the steps listed in Table 2. Note that this protocol did not concern itself with a method for selecting the transducer(s) most appropriate for a flaw of unknown type and size.

The "optimum" transducer for acquiring the waveform from the standard flaw was determined by the Rockwell transducer selection protocol to be the 5-MHz transducer (1,24). According to Equation (1), however, the

"proper" transducer is the 2.25 MHz transducer. Since probably neither is the "correct" transducer (27), we decided to apply the BIT to the waveforms acquired by each of these transducers. The Born diameters obtained for the standard flaw by the Ames and the SwRI hardware systems were essentially the same (see Table 3). These test results therefore confirmed that the Born inversion software was successfully adapted by SwRI.

Table 2

EXPERIMENTAL PROTOCOL FOR THE BORN INVERSION TECHNIQUE

Step	Description
1	Digitize and store the flaw waveform y(t)
2	Digitize and store a reference waveform w(t)
3	Deconvolve y(t) with w(t) [see Equation (3)]
4	Extrapolate magnitude spectrum H(f) to low frequencies
5	Shift impulse response h(t) to make center of flaw coincide with origin of time
6	Compute characteristic function J(r) [see Equation (4)]
7	Estimate flaw size [see Equation (5)]
8	Repeat steps 1 through 7 for another viewing direction

Table 3

BORN DIAMETER ESTIMATES OBTAINED FOR AN 800-µm DIAMETER VOID
AT SOUTHWEST RESEARCH INSTITUTE AND AMES LABORATORY
WITH TWO TRANSDUCERS

BORN DIAMETER, µm

2.25 MHz		5 MHz	
SwRI	Ames	SwRI	Ames
750	640	390	410

4. PROCEDURE DEVELOPMENT

4.1 General

The primary flaw characterization procedures were developed based on the proven capabilities of the three ultrasonic techniques and the three data processing/inversion algorithms listed in Table 4. These techniques and algorithms are described in Section 2. The spectrum splicing technique needs supplementation by the amplitude- and phase-comparison techniques and the deconvolution algorithm, and the BIT needs supplementation by the SST. Thus, all data about the flaw including any a priori information are combined to produce reliable and accurate estimates of the flaw characteristics. The Born inversion procedures, collected under three headings, specifically address the critical transducer selection problem for a flaw of unknown type and size.

4.2 Flaw Identification Procedures

Preliminary examination of the "raw" composite waveforms obtained with the high-frequency (5 and 10 MHz) transducers for the spatial patterns and amplitude and phase distributions of the constituent pulses can reveal the likely flaw composition and shape. If the "locomotive" of the pulse train (i.e., the R pulse originating from the front surface of the flaw) has a positive polarity and if the pulses that follow closely are of comparable amplitude and like polarity, then the flaw is likely to be a weak inclusion (e.g., tungsten carbide). If the R pulse with a positive polarity is not followed by a discernible pulse of like polarity, then the flaw is likely to be a strong inclusion (e.g., sapphire). Finally, if the R pulse has a negative polarity, then the flaw is likely to be a void.

Table 4

SOURCES AND EXPECTED RESULTS/OUTPUTS OF TECHNIQUES/
ALGORITHMS INCORPORATED INTO THE PRIMARY
FLAW CHARACTERIZATION PROCEDURES

Technique/Algorithm	Result/Output	Source
Amplitude comparison Phase comparison	Likely flaw composition and shape	Unknown
Deconvolution	Magnitude spectra	SwRI, Air Force
Spectrum splicing	Appropriate transducer(s)	Ames, Rockwell, SwRI
Zero-of-time[1]	Shifted impulse response	Ames
Born inversion[1]	Flaw size estimate	Ames

---

[1]These algorithms are the essence of the Born inversion technique.

4.3   Transducer Selection Procedures

Qualitative examination of the deconvolved flaw spectrum H(f) obtained with a LW transducer for its extent of modulation can reveal the appropriateness of that transducer for inclusion into the Born inversion protocol (Table 2). Four transducers were used to obtain a set of deconvolved spectra for each of three spherical voids of known size in an effort to test the ability of the SST to quickly rule a transducer "appropriate" or "inappropriate" for that flaw. The spectra obtained for a 550-μm diameter void in an IN100 specimen are shown in Figure 10 against the backgrounds of the individual transducer spectra (dashed curves). The orders of the spectral (resonance) peaks, defined in Figure 3, can be readily identified. The center frequencies of the 10-MHz probes are distant from the flaw's fundamental (n=1) resonance frequency. These probes are then inappropriate for acquiring Born inversion data for this flaw. Note that the center frequency of the 5-MHz probe lies to the right of the first spectral peak and that of the 2-MHz probe lies to the left of the first spectral peak. Both of these probes are, therefore, appropriate for acquiring Born inversion data for this flaw. Note that the "proper" transducer with a center frequency equal to the average spectrum periodicity (3.4 MHz) was not available.

The magnitude spectra obtained for the 800-μm diameter (standard) void by sequentially acquiring waveforms with transducers having successively lower center frequencies are shown in Figure 11. The 2.5-MHz transducer whose bandwidth is almost perfectly centered on the first peak of H(f) is the most appropriate one for acquiring the backscattered waveforms for Born inversion.

As expected, the smallest spectrum periodicities (p values) were measured for the largest void (see Figure 12). While the high-frequency transducers served quite well in determining the Born frequency for this strong flaw (F = 2 MHz), none of these transducers is appropriate for acquiring the waveforms for Born inversion.

The spectral peaks can be more reliably ordered when the individual spectra obtained for the same flaw are spliced together (see Figure 13). Note that for only one of the three flaws did the required frequency F (=p) coincide with the effective center frequency of one of the three standard-frequency transducers (i.e., for the largest flaw).

The purpose of the transducer selection protocol is to rule at least one of the three standard-frequency transducers inappropriate for acquiring the Born inversion data. The gates (time windows) for the SST waveforms must include all trailers of the R pulse recognized during the qualitative flaw-identification process. The protocol for selecting the most appropriate Born transducer(s) consists of the steps listed in Table 5.

4.4   Flaw Sizing Procedures

A subcontract was let to Rockwell Science Center to assure that the Ames sizing procedures featuring the BIT are basically the same as the Rockwell sizing procedures (i.e., they yield essentially the same size

22
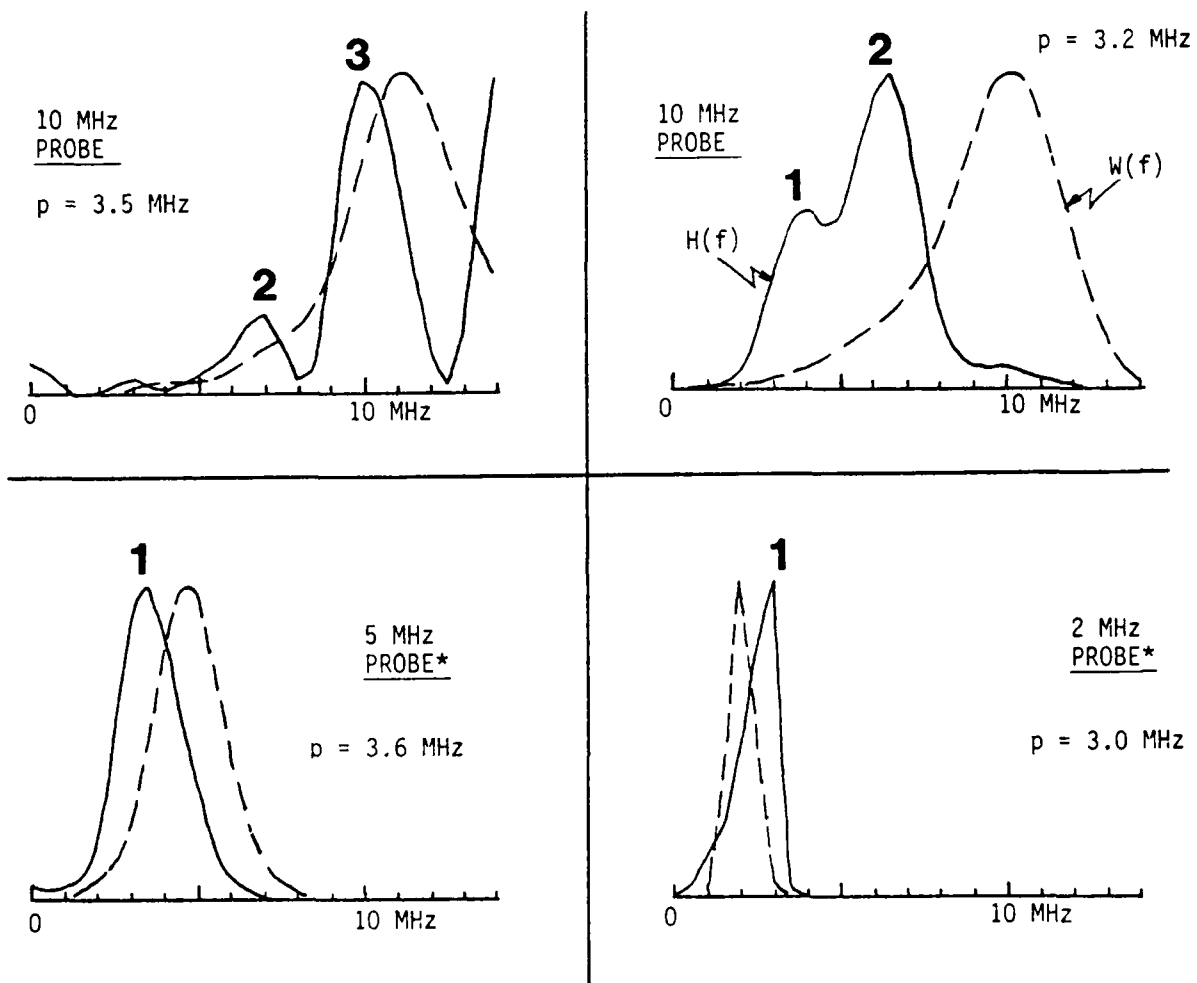
Figure 10. Magnitude Spectra Obtained for a 550-μm Diameter IN100 Void
With Four Longitudinal-Wave Transducers. The asterisks denote
the two most appropriate Born transducers. Note that the
fundamental resonance frequency of this flaw is 3.4 MHz.
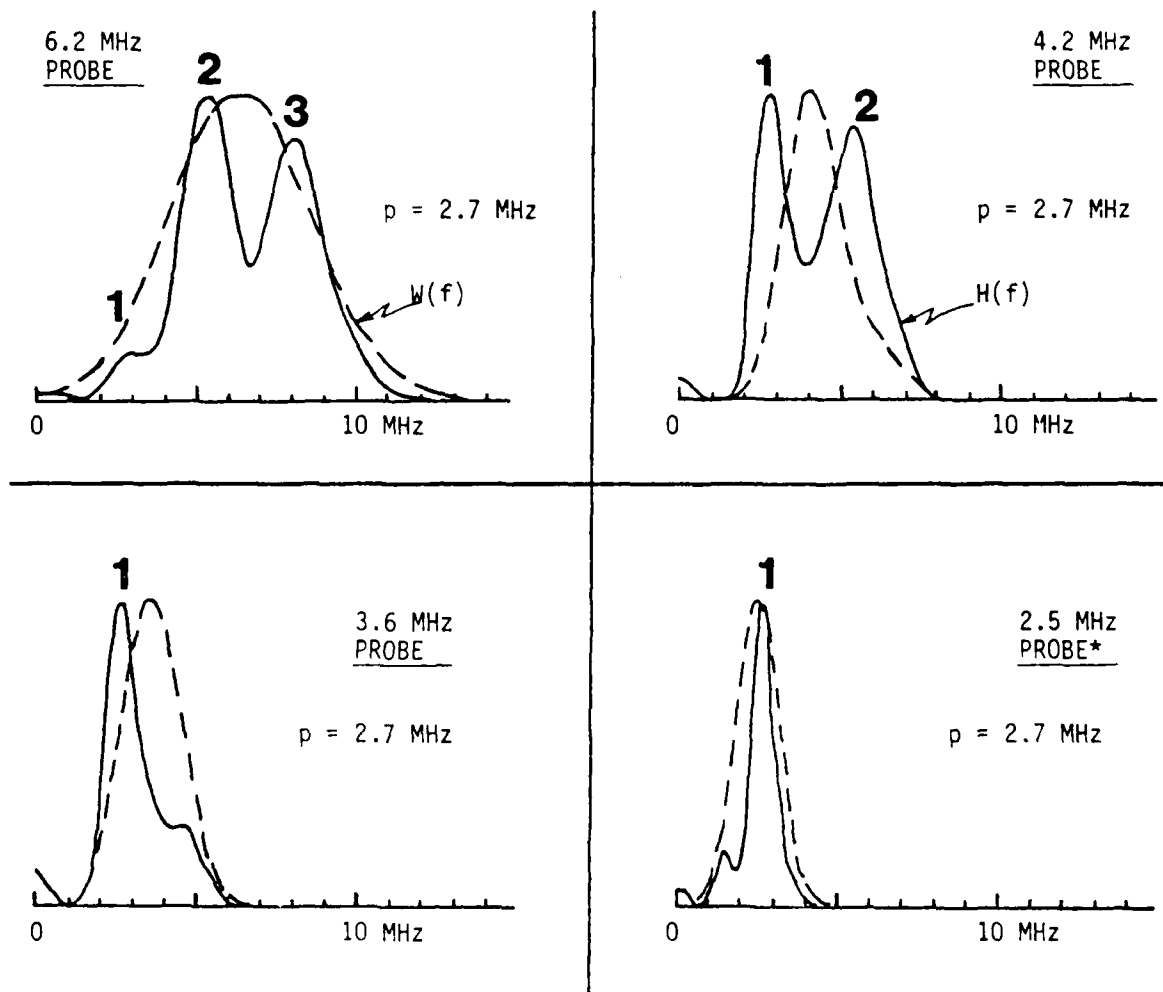
Figure 11. Magnitude Spectra Obtained for an 800-μm Diameter Titanium Void (Standard Flaw) With Four Longitudinal-Wave Transducers. The asterisk denotes the most appropriate Born transducer. Note that the fundamental resonance frequency of this flaw is 2.7 MHz.
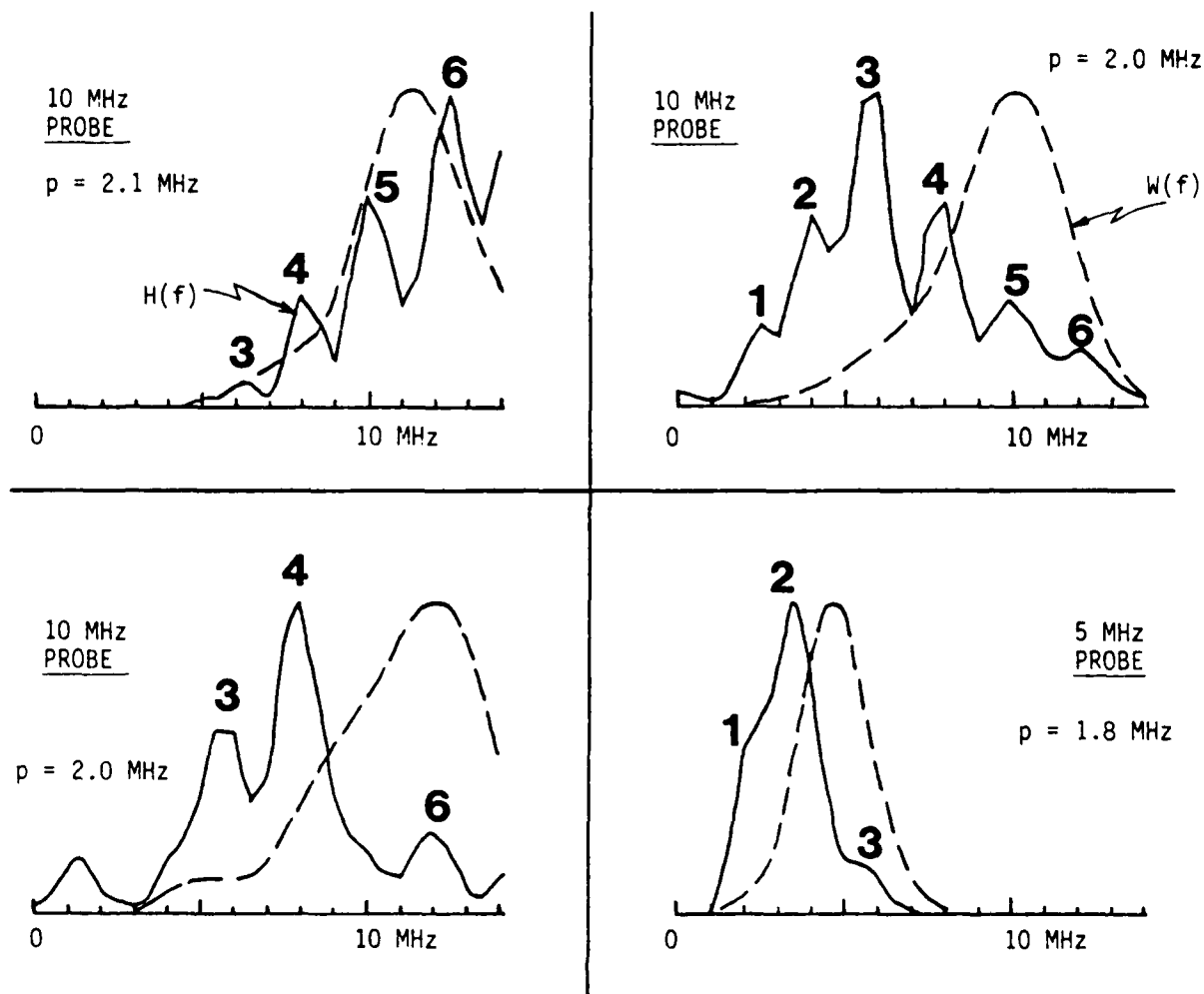
Figure 12. Magnitude Spectra Obtained for a 1,050-μm Diameter IN100 Void With Four Longitudinal-Wave Transducers. Note that the fundamental resonance frequency of this flaw is 2.0 MHz.

550-µm DIAMETER
VOID IN IN100

p = 3.4 MHz

H(f)

1   **2**   **3**   **4**

0   10 MHz
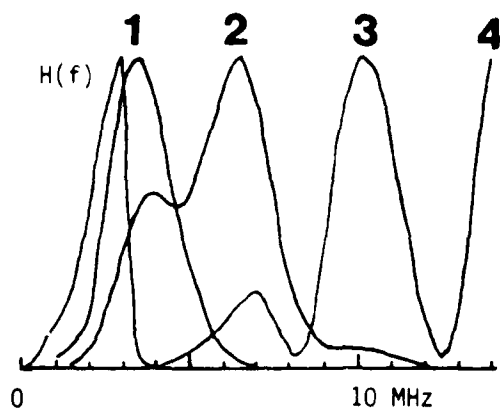
800-µm DIAMETER
VOID IN TITANIUM

p = 2.7 MHz

1   **2**   **3**

0   10 MHz
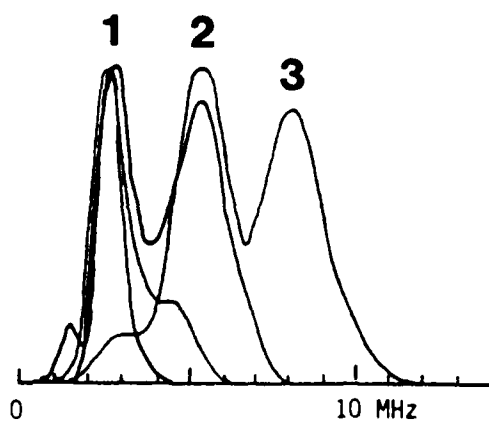
1,050-µm DIAMETER
VOID IN IN100

p = 2.0 MHz

1   **2**   **3**   **4**   **5**   **6**
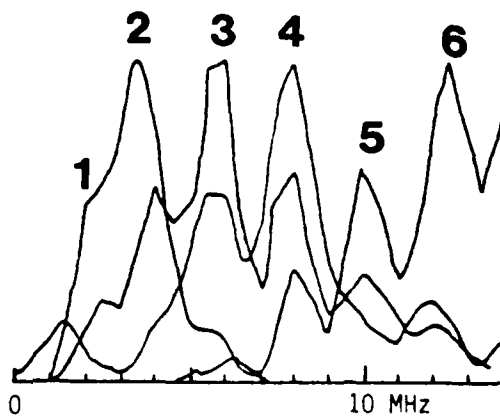
0   10 MHz

Figure 13.   Application of the Spectrum Splicing Technique (SST)
to Three Spherical Voids.

26

Table 5

EXPERIMENTAL PROTOCOL FOR THE SPECTRUM SPLICING TECHNIQUE

Step	Description
1	Set the gate for the flaw waveform y(t) obtained with the 10-MHz transducer
2	Digitize and store y(t)
3	Digitize and store a gated reference waveform w(t)
4	Deconvolve y(t) with w(t) [see Equation (3)]
5	Repeat steps 1 through 4 with the 5-MHz transducer
6	Repeat steps 1 through 4 with the 2.25-MHz transducer
7	Splice the individual magnitude spectra H(f) together (see Figure 13)
8	Determine average spectrum periodicity p
9	Calculate required frequency F [see Equation (2)]
10	Eliminate the inappropriate transducer(s) from the Born inversion protocol (Table 2)

estimates for the same set of stored waveforms). The standard flaw was the basis of comparison. Figures 14 through 17 contain the Born plots H(f), h(t), A(f), and J(r) obtained by applying the Ames sizing procedures (1,13,26) to the waveforms acquired at SwRI with transducers having successively lower center frequencies. The amplitude spectrum A(f) and the characteristic function J(r) form a transform pair [see Equation (4)]. The deconvolved flaw spectrum H(f) and the impulse response h(t) are also known to form a transform pair. It can be shown (15) that the periodicity of the flaw's magnitude spectrum is governed by the extent of its impulse response (i.e., $p = 1/\sigma$). A similar reciprocal relationship appears to exist between the width of the characteristic function and the mean frequency of the amplitude spectrum (i.e., $a^* = 1/k^*$). The mean frequency is, in turn, governed by the transducer center frequency. Other parameters being the same, the larger the transducer center frequency, the smaller the Born diameter (see Table 6).

Figures 18 through 21 contain the Born plots H(f), $D(\tau)$, and J(t) obtained by applying the Rockwell sizing procedures (2) to the waveforms acquired either at SwRI or Rockwell with transducers having successively lower center frequencies. The main difference between the Rockwell and Ames Born inversion procedures is in the way the center of the flaw is located. The Ames ZOTA is described in connection with Figures 5 and 6.

27

MAGNITUDE SPECTRUM

H(f)

2

3

1

p = 2.8 MHz

W(f)

0   10 MHz

"IMPROPER" BORN TRANSDUCER

IMPULSE RESPONSE

h(t)   σ = 380 ns

0   1.5 μs

S_e

R

AMPLITUDE SPECTRUM

A(f)

f* = 5.7 MHz

50%

0   f*   10 MHz

CHARACTERISTIC FUNCTION

J(r)

50%   d* = 290 μm

0   a*   500 μm

Figure 14.   Transform Pairs Obtained for an 800-μm Diameter Void With
a 6.2 MHz Longitudinal-Wave Transducer Using the Ames
Sizing Procedures. Note that pσ = 1.06 and k*a* = 0.85.

MAGNITUDE SPECTRUM

1   **2**

H(f)

p = 2.6 MHz

W(f)

0   10 MHz

"IMPROPER" BORN TRANSDUCER

IMPULSE RESPONSE

h(t)   σ = 370 ns

0   2 μs

S_e

R

AMPLITUDE SPECTRUM

A(f)

f* = 3.6 MHz

50%

0   f*   10 MHz

CHARACTERISTIC FUNCTION

J(r)

50%   d* = 490 μm

0   a*   500 μm

Figure 15.   Transform Pairs Obtained for an 800-μm Diameter Void With
a 4.2 MHz Longitudinal-Wave Transducer Using the Ames
Sizing Procedures.   Note that pσ = 0.96 and k*a* = 0.91.

29

MAGNITUDE SPECTRUM

H(f)
W(f)

p = 2.9 MHz

0   10 MHz

"IMPROPER" BORN TRANSDUCER

IMPULSE RESPONSE

h(t)   σ = 390 ns

0   2 μs

S_e

R

AMPLITUDE SPECTRUM

A(f)

f* = 2.7 MHz

50%

0   f*   10 MHz

CHARACTERISTIC FUNCTION

J(r)

50%   d* = 650 μm

0   a*   500 μm

Figure 16.   Transform Pairs Obtained for an 800-μm Diameter Void With
              a 3.6 MHz Longitudinal-Wave Transducer Using the Ames
              Sizing Procedures.   Note that pσ = 1.13 and k*a* = 0.90.

30

MAGNITUDE SPECTRUM

H(f)

p = 2.7 MHz

W(f)

0   10 MHz

"PROPER" BORN TRANSDUCER

IMPULSE RESPONSE

h(t) σ = 370 ns

0   2.5 μs

S_e

R

AMPLITUDE SPECTRUM

A(f)

f* = 2.3 MHz

50%

0   f*   10 MHz

CHARACTERISTIC FUNCTION

J(r)

50%   d* = 790 μm

0   a* 500 μm
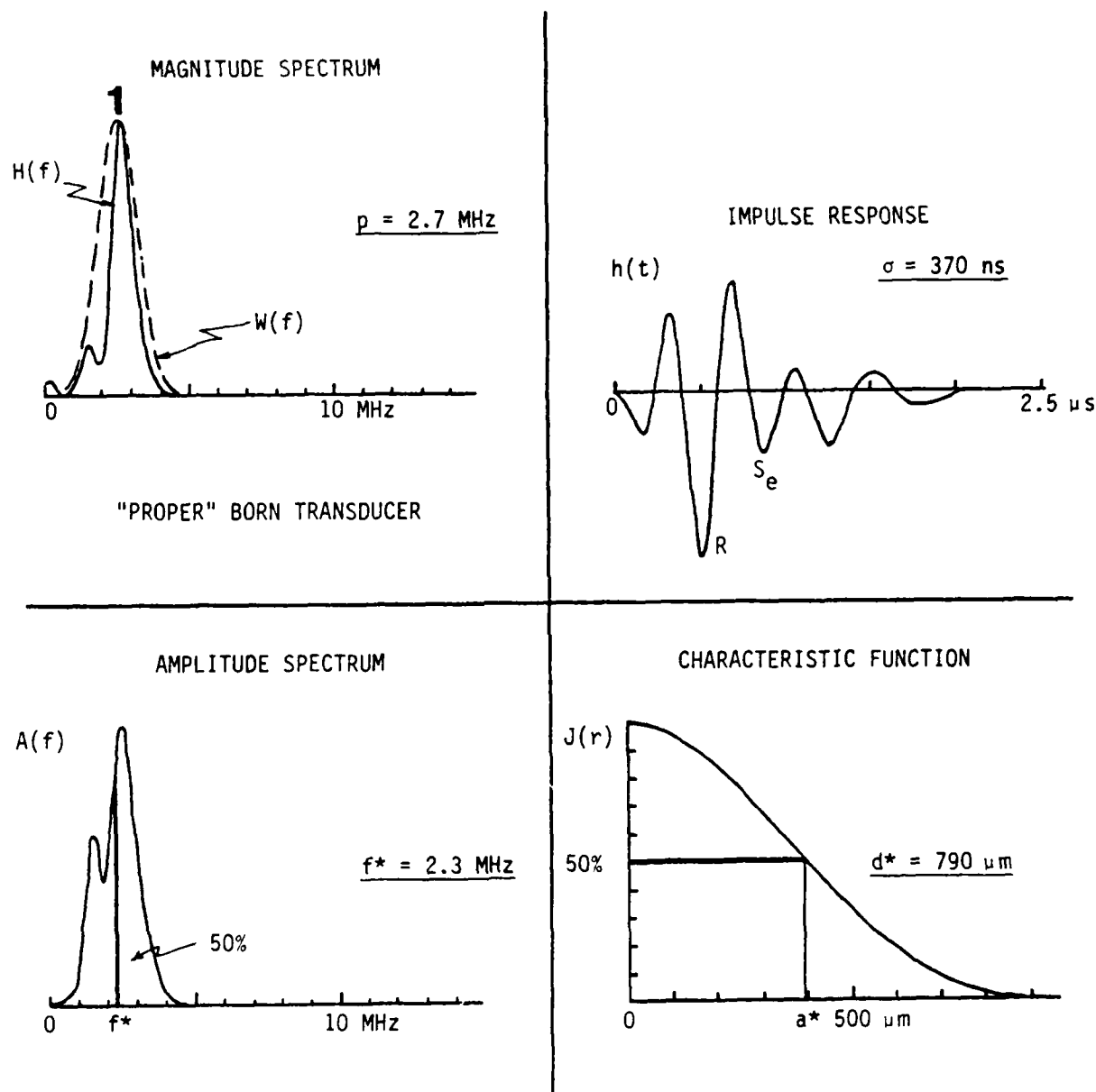
Figure 17.   Transform Pairs Obtained for an 800-μm Diameter Void With
a 2.5 MHz Longitudinal-Wave Transducer Using the Ames
Sizing Procedures.   Note that pσ = 1.00 and k*a* = 0.94.

31

MAGNITUDE SPECTRUM

"IMPROPER" BORN TRANSDUCER

$f_0 = 8.3$ MHz

W(f)

H(f)

3

0   f_0 16 MHz

VARIATION OF BORN DIAMETER
WITH TIME SHIFT τ

D(τ)

400 μm

$d_0 = 280$ μm

0

-20   0   60 ns
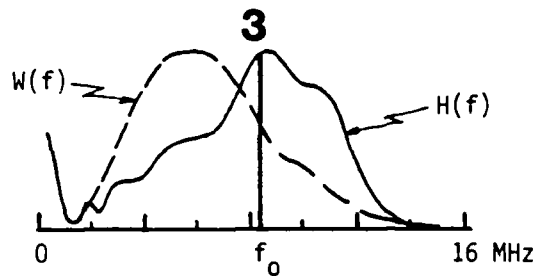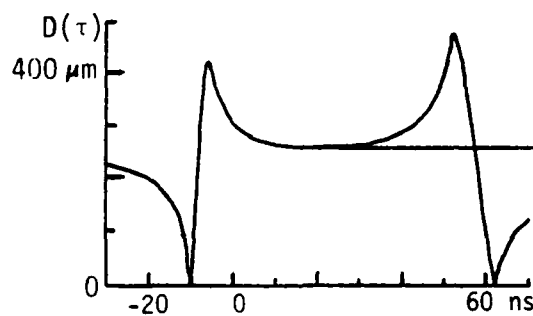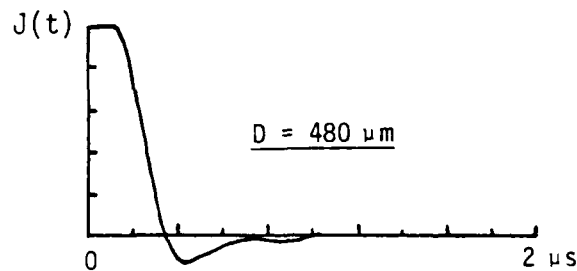
CHARACTERISTIC FUNCTION
FOR $\tau = 52$ ns

J(t)

D = 480 μm

0   2 μs

Figure 18. Born Diameters Obtained for an 800-μm Diameter Void With
a 6.2 MHz Longitudinal-Wave Transducer Using the Rockwell
Sizing Procedures. Note that $k_0 a_0 = 1.20$.
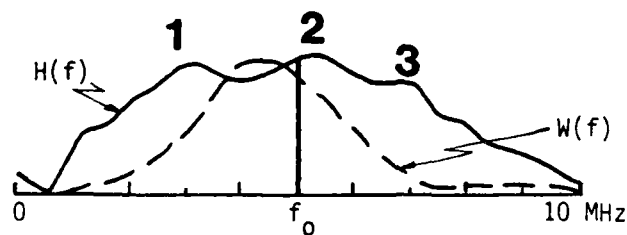
MAGNITUDE SPECTRUM
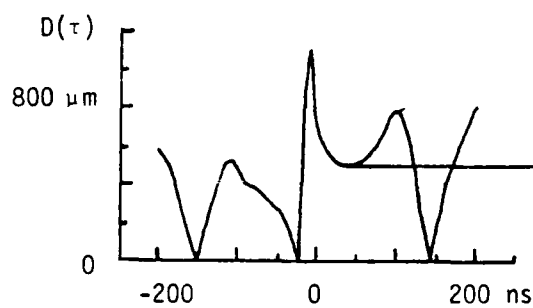
"PROPER" BORN TRANSDUCER

f_o = 5.0 MHz

VARIATION OF BORN DIAMETER
WITH TIME SHIFT τ

d_o = 510 μm
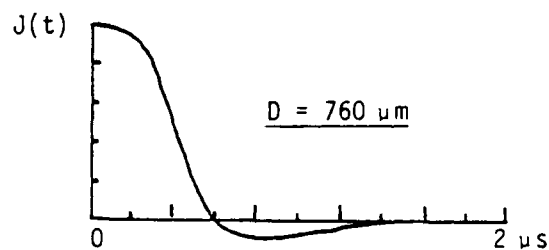
CHARACTERISTIC FUNCTION
FOR τ = 96 ns

D = 760 μm

Figure 19. Born Diameters Obtained for an 800-μm Diameter Void With
a 4.3 MHz Longitudinal-Wave Transducer Using the Rockwell
Test Bed System (Reference 2) and Sizing Procedures.
Note $k_o a_o$ = 1.31.

33
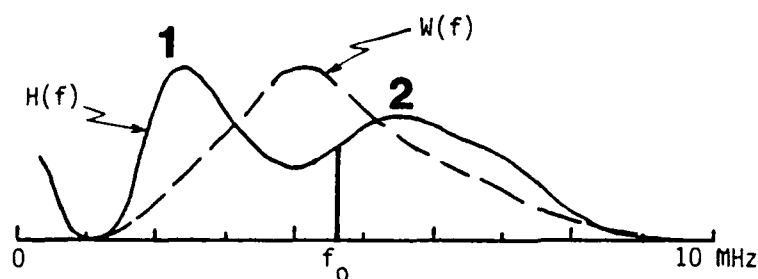
MAGNITUDE SPECTRUM

"PROPER" BORN TRANSDUCER

$f_0 = 4.6$ MHz

VARIATION OF BORN DIAMETER
WITH TIME SHIFT τ

$d_0 = 480$ μm
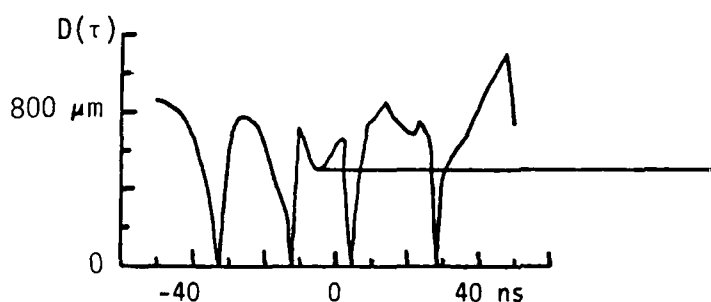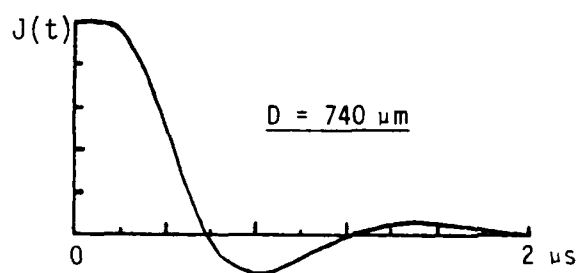
CHARACTERISTIC FUNCTION
FOR $\tau = 10$ ns

Figure 20. Born Diameters Obtained for an 800-μm Diameter Void With
a 4.2 MHz Longitudinal-Wave Transducer Using the Rockwell
Sizing Procedures. Note that $k_0 a_0 = 1.14$.
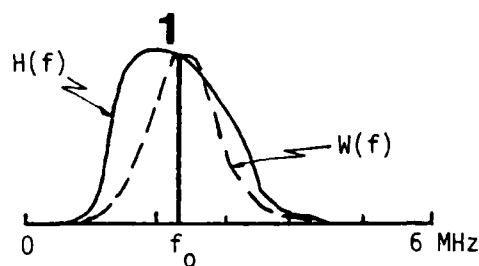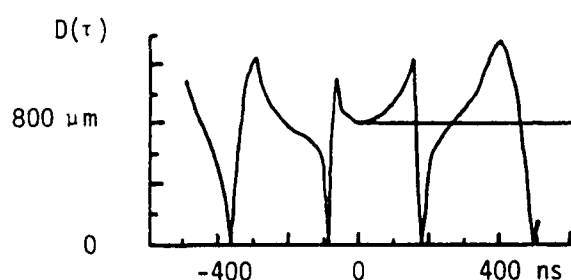
34

MAGNITUDE SPECTRUM

"IMPROPER" BORN TRANSDUCER

f_o = 2.3 MHz

H(f)

W(f)

0   f_o 6 MHz

VARIATION OF BORN DIAMETER
WITH TIME SHIFT τ

D(τ)

800 μm

d_o = 800 μm

0

-400   0   400 ns

CHARACTERISTIC FUNCTION
FOR τ = 140 ns

J(t)

D = 1,250 μm
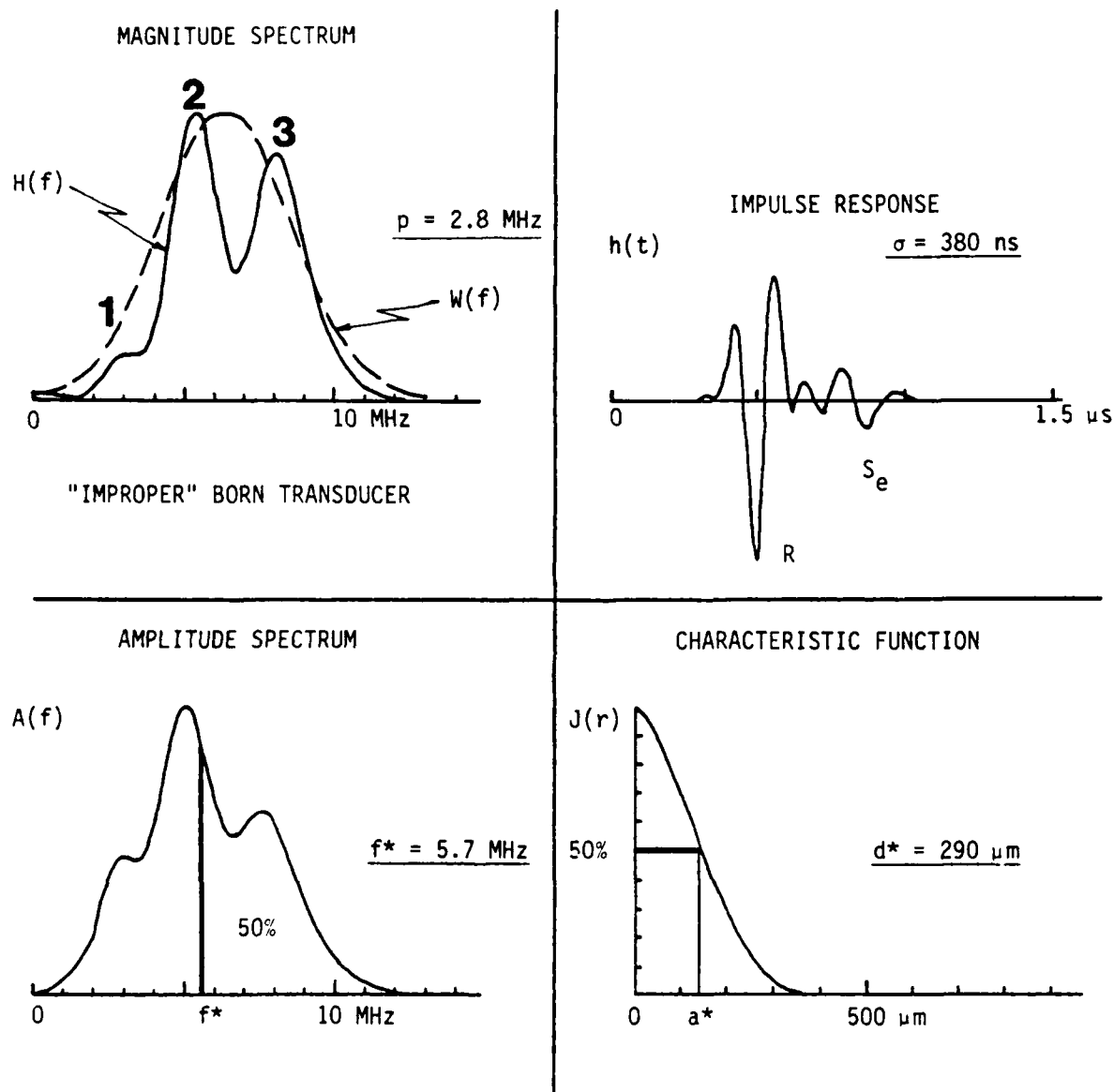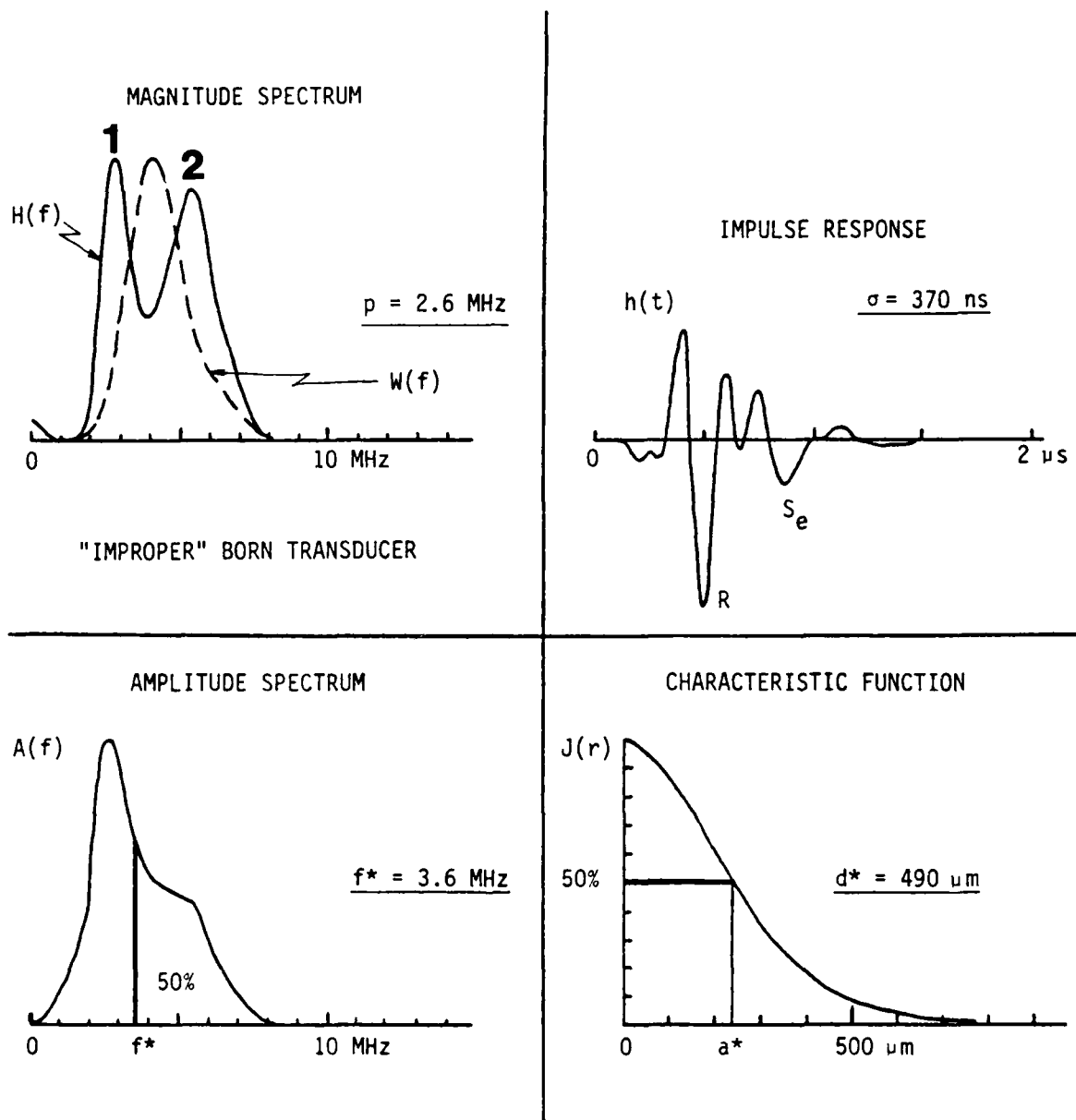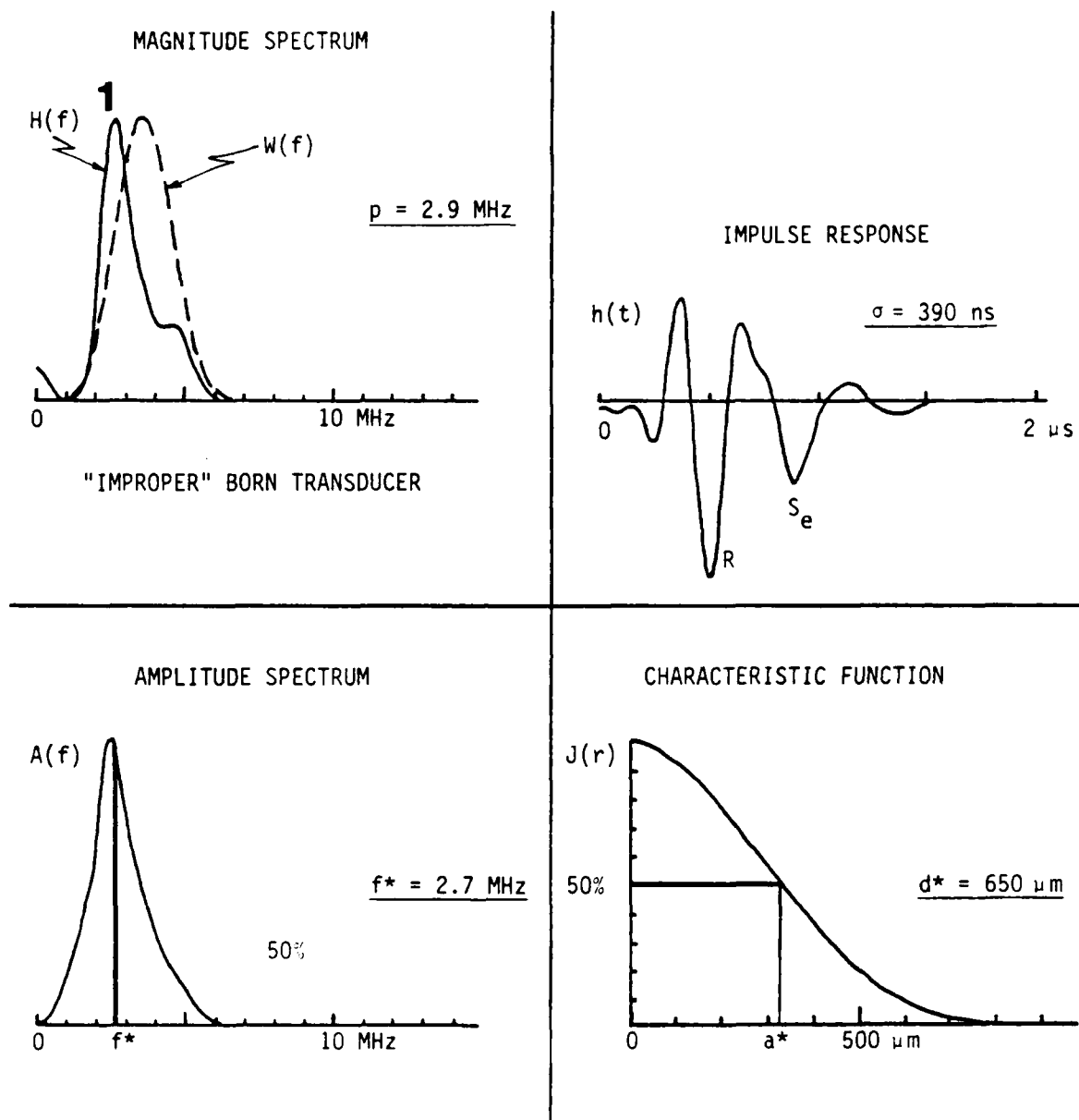
0   2 μs
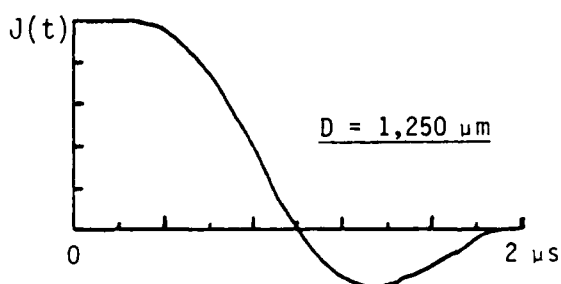
Figure 21.   Born Diameters Obtained for an 800-μm Diameter Void With
             a 2.5 MHz Longitudinal-Wave Transducer Using the Rockwell
             Sizing Procedures.   Note that $k_o a_o$ = 0.95.

Table 6

BORN DIAMETER ESTIMATES OBTAINED WITH FIVE TRANSDUCERS
FOR AN 800-μm DIAMETER VOID AT SOUTHWEST RESEARCH
INSTITUTE AND ROCKWELL SCIENCE CENTER

Transducer Center Frequency, MHz		Born Diameter, μm [1]			
Nominal	Effective	SwRI (σ_e, ns)[4]		Rockwell	d_o
10	6.2	290	(370)	480	230
5	4.2	490	(370)	740	480
5	4.3[2]	---	(---)	760	510
5	3.6	650	(370)	---	---
2.25	2.5[3]	790	(370)	1,250	800

[1] Size estimates obtained with the most appropriate (SST-approved) transducers are underlined.
[2] "Optimum" transducer per Rockwell procedures (Reference 2).
[3] "Proper" transducer per SwRI procedures [Equation (1)].
[4] $\sigma_e = 1/p$ (Figure 11).

The Rockwell ZOTA has no physical basis. An empirical technique has been found (2) which works when the transducer's bandwidth is well centered on the first peak of the magnitude spectrum (see upper diagram in Figure 21). This technique requires that the characteristic function J(t) have maximum flatness at t=0.

Two steps are involved in obtaining the required time shift for the impulse response. First, the Born diameter is determined for a wide range of time shifts (see middle diagram of Figure 19). It is known that the center of the flaw is located near the second maximum of $D(\tau)$ and displaced to the left of it. Next, a series of characteristic functions is generated for time shifts ranging from $\tau=0$ to 100 ns. The characteristic function was maximally flat for $\tau=96$ ns and it resulted in a Born diameter of 760 μm (see lower diagram in Figure 19). However, in another case when the transducer bandwidth was also well centered on the first peak of the magnitude spectrum (see upper diagram of Figure 21), the Born diameter corresponding to the maximally flat characteristic function was 1,250 μm.

The Rockwell column in Table 6 contains the Born diameters obtained by maximizing the flatness of the characteristic function at t=0. Rather than these estimates, the Born diameters denoted by d_o in Figures 18 through 21 and collected in the last column of Table 6 appear to correspond to those obtained with the Ames procedures and included in the SwRI column of Table 6. This established the equivalency of the Ames and Rockwell Born inversion procedures.

5. TEST SPECIMENS

5.1 General

In order to qualify the developed flaw characterization procedures it is necessary to have test specimens that contain a statistically large number of internal bulk flaws with characteristics (other than locations) unknown to the ultrasonic examiners. A subcontract was let to Pratt & Whitney Aircraft Group (PWA) for the fabrication of titanium alloy and powder metallurgy nickel-based superalloy test specimens containing 40 simulated flaws and the collection of up to 10 real-world flaws. Flaw locations and characteristics (composition, shape, size, and orientation) were documented by PWA during specimen design. However, only the flaw locations, the 250 to 1,300 μm size range, and the list of possible flaw compositions were submitted to SwRI with the specimens to preserve the credibility of the test results. This section describes the material and flaw types, the test specimens, and the procedures employed to produce these specimens.

5.2 Material and Flaw Types

Titanium alloys and nickel-based superalloys are the two basic material types used to make rotor components for gas turbine engines. In each alloy, flaws of different composition have been found according to the differences in the chemical activity of the alloy base elements and in the manufacturing processes used to form these materials into engine disks.

Three types of manufacturing flaws have been identified in titanium alloys--porosity, chemical segregation, and tungsten carbide (WC) inclusion. Voids and WC inclusions are readily detectable with ultrasonic waves. Manufacturing flaws are found more frequently in nickel alloys than in titanium alloys because melt practice is not yet sufficiently developed to prevent the introduction of voids and hard oxide inclusions (e.g., sapphire).

Disk material specimens containing 46 separately identifiable voids and inclusions were provided by PWA of West Palm Beach, Florida (28). The shapes of the 40 electro-discharge machined (EDM) flaws were limited to spheres. Flaw sizes were to be in the 250 to 1,300 μm range. The distribution of the disk materials, flaw types, and number of flaws per specimen is shown in Table 7. Inclusions in the diffusion-bonded titanium specimen were to be tungsten carbide inclusions and those in the diffusion-bonded IN100 specimens were to be sapphire (Al_2O_3) inclusions.

Manufacturing processes (machining, bonding, heat treating, and surface finishing) on the test specimens were the same as on turbine engine components. Special attempts were made to allow for a clear line of sight to the test flaws from all sides of the diffusion-bonded specimens.

Table 7

TEST SPECIMENS PROVIDED BY PRATT & WHITNEY AIRCRAFT GROUP

Specimen No.	Material	Flaw Type	No. of Flaws (ID Nos.)
FML 97413	Ti 6-4	Void	5 (01-05)
FML 97414	IN100	Void	5 (06-10)
FML 97416	Ti 6-4	Inclusion	5 (11-15)
FML 97474-1	IN100	Inclusion	3 (16-18)
-2	IN100	Inclusion	3 (19-21)
-3	IN100	Inclusion	3 (22-24)
-4	IN100	Inclusion	3 (25-27)
-5	IN100	Inclusion	3 (28-30)
-6	IN100	Inclusion	3 (31-33)
-7	IN100	Inclusion	4 (34-37)
-8	IN100	Inclusion	3 (38-40)
FML 97600-1	IN100	Unknown	3 (41-43)
-2			3 (44-46)
		Total	46

5.3   Voids in Titanium Specimen No. FML 97413

This specimen consists of three diffusion-bonded plates of varying thickness. Five spherical voids with diameters ranging from 320 to 1,230 μm are located in the two bondplanes.* The manufacturing processes for this specimen are listed in the second column of Table 8.

5.4   Inclusions in Titanium Specimen No. FML 97416

This specimen is configured the same way as specimen No. FML 97413. Five spherical WC inclusions with diameters ranging from 480 to 1,210 μm are located in the two bondplanes. The manufacturing processes were different for this titanium specimen (see third column in Table 8). A hot isostatic press (HIP) process was used to close the holes around the inclusions after the plates were bonded together. This was done to ensure continuous contact between the host material and the WC spheres.

5.5   Voids in IN100 Specimen No. FML 97414

This specimen consists of three super powder metallurgy IN100 plates diffusion-bonded with nickel foil. Five spherical voids with diameters

---

*The ultrasonic examiners did not know that the voids were spherical.

38

Table 8

MANUFACTURING PROCESS PLANS FOR TITANIUM 6-4 TEST SPECIMENS

Sequence	Void Specimen No. FML 97413	Inclusion Specimen No. FML 97416
1	Cut raw material from stock	Cut raw material from stock
2	Rough cut and drill two position holes	Rough cut and drill two position holes
3	Grind and lap bonding surfaces	Grind and lap bonding surfaces
4	Mark plates	Mark plates
5	EDM voids (5)	EDM holes for inclusions (5)
6	Deburr holes by light lap	Deburr holes by light lap
7	Fabricate two position pins	Fabricate two position pins
8	Assemble and diffusion-bond plates	Assemble and diffusion-bond plates
9	Heat treat to Spec. PWA 1215	Hot isostatic press (HIP)
10	Final machine	Heat treat to Spec. PWA 1215
11	Ultrasonic examination	Final machine
12	Ship to SwRI	Ultrasonic examination
13		Ship to SwRI

ranging from 320 to 1,230 μm are located in the two bondplanes. The manu-facturing processes for this specimen are listed in the second column of Table 9.

5.6   Inclusions in IN100 Specimen Nos. FML 97474-1 through -8

Eight IN100 specimens containing a total of 25 spherical sapphire inclusions were fabricated. Each test specimen is made up of two diffusion-bonded plates of equal thickness. The inclusions with diameters ranging from 410 to 990 μm are located in the bondplane. The manufacturing pro-cesses for these specimens are listed in the third column of Table 9.

5.7   Real Flaws in IN100 Specimen Nos. FML 97600-1 and -2

Two IN100 specimens were provided with six flaws of unknown composi-tion, shape, size, and orientation found during production material pro-cessing in an extruded billet. The billet was forged into a pancake from which the specimens were cut.

Table 9

MANUFACTURING PROCESS PLANS FOR IN100 TEST SPECIMENS

Sequence	Void Specimen No. FML 97414	Inclusion Specimen No. FML 97474
1	Cut raw material from stock	Cut raw material from stock
2	Rough cut and drill two position holes	Rough cut plates
3	Grind and lap bonding surfaces	Grind and lap bonding surfaces
4	Mark plates	EDM holes for inclusions (3-5)
5	EDM Voids (5)	Deburr holes by light lap
6	Deburr holes by light lap	Mark plates
7	Fabricate two position pins	Assemble and diffusion-bond plates
8	Assemble and diffusion-bond plates	HIP
9	Heat treat to modified Spec. PWA 1074	Heat treat to modified Spec. PWA 1074
10	Final machine	Final machine
11	Ultrasonic examination	Mark specimen
12	Ship to SwRI	Ultrasonic examination
13		Ship to SwRI

6. PROCEDURE QUALIFICATION

6.1 General

The simulated and real flaws in the test specimens were used solely for verification of the applicability of the selected flaw characterization technique combinations described in Section 2. In order to reconstruct the flaw from the results of the one-dimensional BIT it was necessary to acquire many flaw waveforms from regularly placed transducer positions. While the flaws were accessible from all six sides of a test specimen, no measurements were taken from the four sides intersecting the bondplanes associated with the specimen manufacturing process.

The likely compositions, shapes, and sizes for the 42 detectable test flaws are presented in four parts. The first two parts (Subsections 6.2 and 6.3) contain the results obtained by the serial applications of the supplemented SST and the BIT [i.e., the techniques incorporated into the primary flaw characterization procedures (see Table 4)]. The SPOT flaw size estimates are given in Subsection 6.4. Finally, the results obtained for the 32 detectable inclusions by an automatable version of the SPOT-SST combination that waives the need for a highly trained operator are presented in Subsection 6.5.

6.2 Born Frequency Estimates

The transducer selection results obtained by the application of the SST to the individual magnitude spectra of each test flaw are presented under four headings (i.e., voids, tungsten carbide inclusions, sapphire inclusions, and real flaws).

6.2.1 Voids in Titanium and IN100 Specimens

The amplitude- and phase-comparison techniques were applied first to the flaws in titanium specimen No. FML 97413 and IN100 specimen No. FML 97414. As the 10-MHz (or 5-MHz) immersion LW transducer was moved around a given flaw, the received waveforms were noted to contain essentially the same key signal parameters (pulse polarities, pulse train durations, and echo dynamic patterns). Based on these observations, the flaws in specimen Nos. FML 97413 and FML 97414 were identified to be spherical voids.*

The individual magnitude spectra H(f) obtained for one of the voids (flaw 02) with two 10-MHz, one 5-MHz, and one 2-MHz transducers are displayed against the backgrounds of the appropriate transducer spectra W(f) in Figure 22.** The first five external resonances (spectral peaks 1 through 5) of this flaw were readily identified in each of the

---

*These preliminary conclusions were later substantiated by SW measurements (see Subsection 6.4).
**Appendix A contains a full set of magnitude spectra.
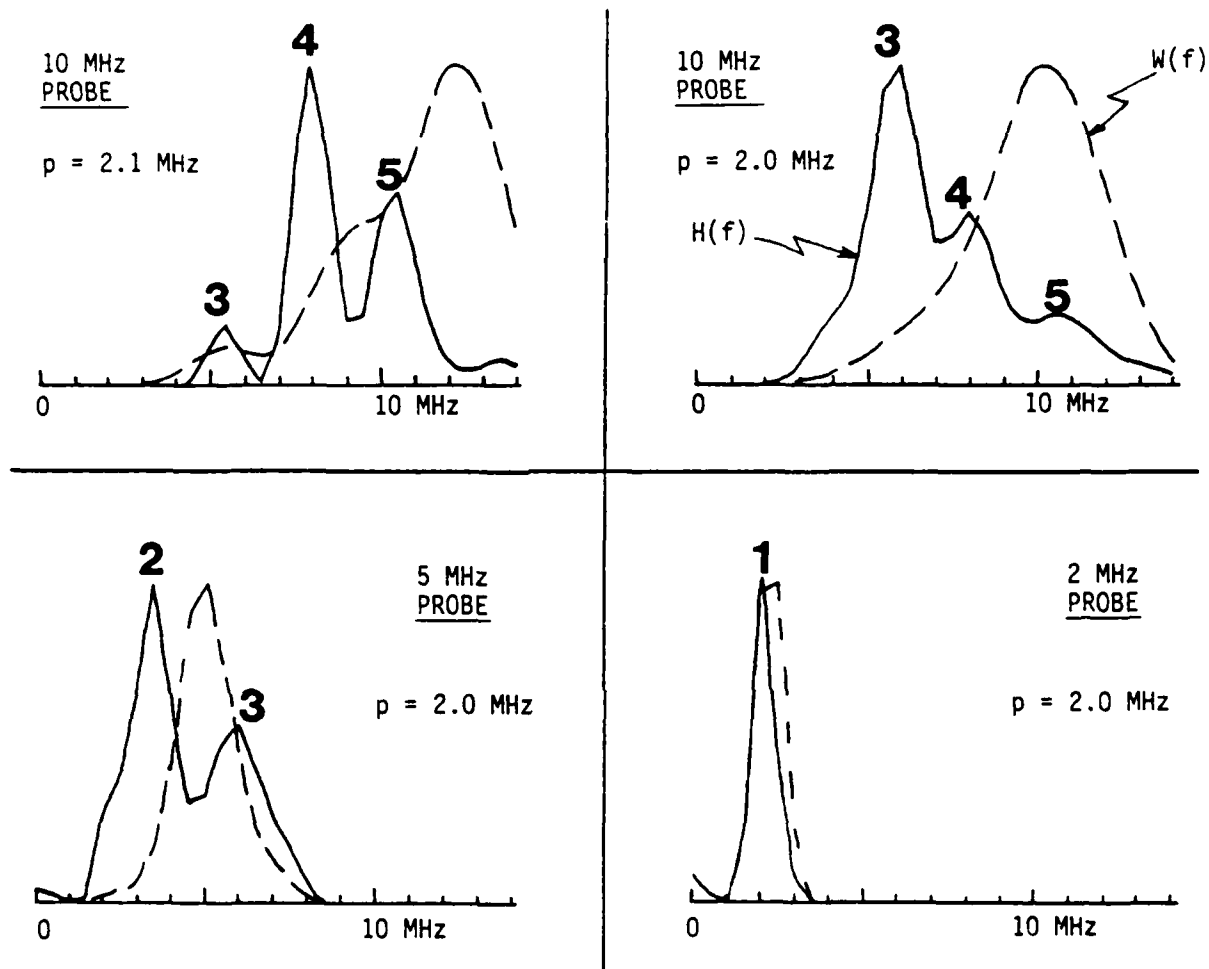
Figure 22. Magnitude Spectra Obtained for Titanium Void No. 02
With Four Longitudinal-Wave Transducers

individual plots. However, the first two spectral peaks of flaw 01 were
not identified until the individual spectra obtained with the two 10-MHz
transducers were spliced together (see Figure 23). The improved visibil-
ity of the spectral peaks is the merit of the SST. The flaw profiles
(spliced frequency-domain responses) of Figure 23 indicate that the 2-MHz
transducer is the proper one for flaws 02 and 05, while the 5-MHz and the
10-MHz transducers should be used in acquiring the Born data on the other
three flaws. The profiles obtained for flaws 06 through 10 are reproduced
in Figure 24. The effective transducer center frequencies (F) required by
the ten voids are listed in the last column of Table 10.

6.2.2 Tungsten Carbide Inclusions in Titanium Specimen

The application of the amplitude- and phase-comparison tech-
niques to the flaws in titanium specimen No. FML 97416 revealed that these
flaws are spherical tungsten carbide inclusions.* Figure 25 shows the
individual magnitude spectra obtained for one of the WC inclusions (flaw
11) with four immersion LW transducers.** The profiles obtained for the
five WC inclusions are shown in Figure 26. The effective transducer center
frequencies required by these inclusions are obtained by multiplying the

Table 10

BORN FREQUENCY ESTIMATES OBTAINED FOR THE VOIDS IN TITANIUM
SPECIMEN NO. FML 97413 AND IN100 SPECIMEN NO. FML 97414 BY
THE SPECTRUM SPLICING TECHNIQUE (SST)

Flaw ID No.	Transducer Center Frequency				Average Spectral Period, MHz[1]
	Low	Med. Low	Med. High	High	
01	--(2)	--(2)	6.5	5.6	6.0
02	2.0	2.0	2.0	2.1	2.0
03	--(2)	3.2	2.7	2.5	2.8
04	--(2)	2.8	2.5	2.5	2.6
05	2.0	1.7	2.0	2.0	1.9
06	2.7	3.0	2.7		2.8
07	1.2	1.4	--(3)		1.3
08	--(2)	5.4	6.4		5.9
09	--(2)	2.1	2.3		2.2
10	2.5	2.1	2.4		2.3

[1]The Born frequency for a void is given by the average periodicity of its
magnitude spectra (spectral period, F=p).
[2]Magnitude spectrum peaked at the transducer center frequency (feedthrough).
[3]Unmodulated magnitude spectrum.

---

*These preliminary conclusions were borne out by SW measurements (see
Subsection 6.4).
**Appendix A contains a full set of magnitude spectra.
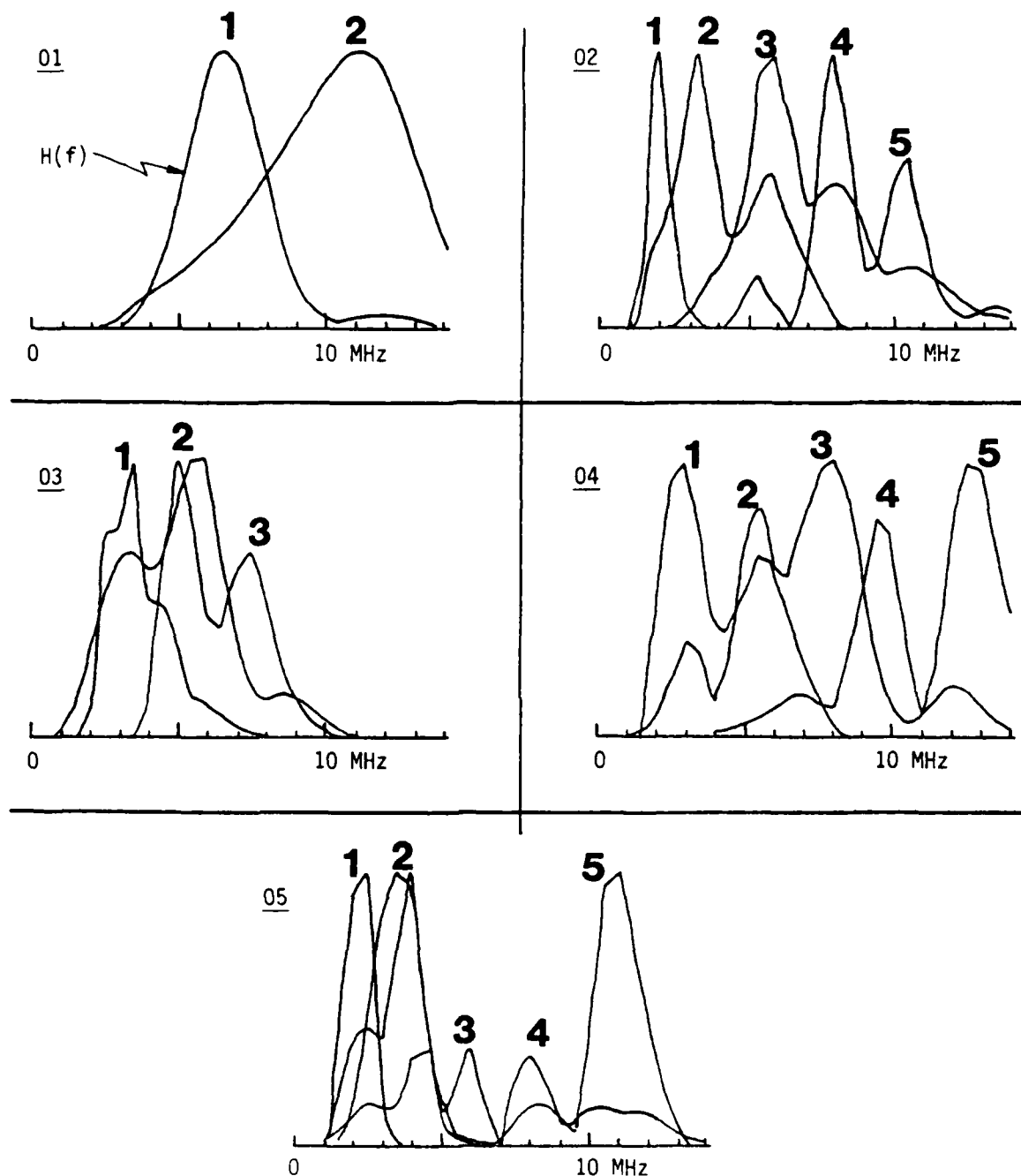
Figure 23. Application of the Spectrum Splicing Technique (SST) to the Voids in Titanium Specimen No. FML 97413 (Flaws 01 Through 05)
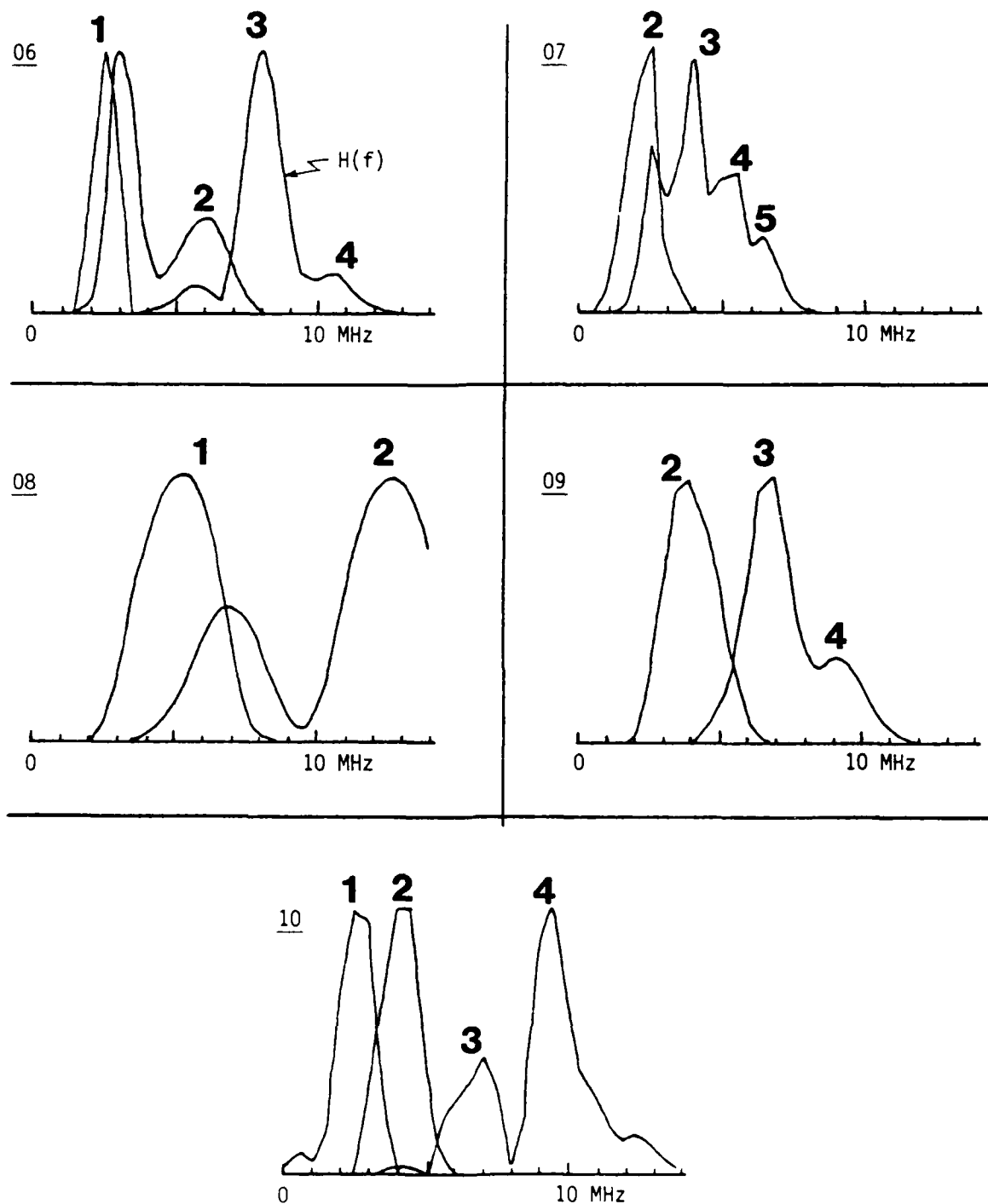
Figure 24. Application of the SST to the Voids in IN100
Specimen No. FML 97414 (Flaws 06 Through 10)
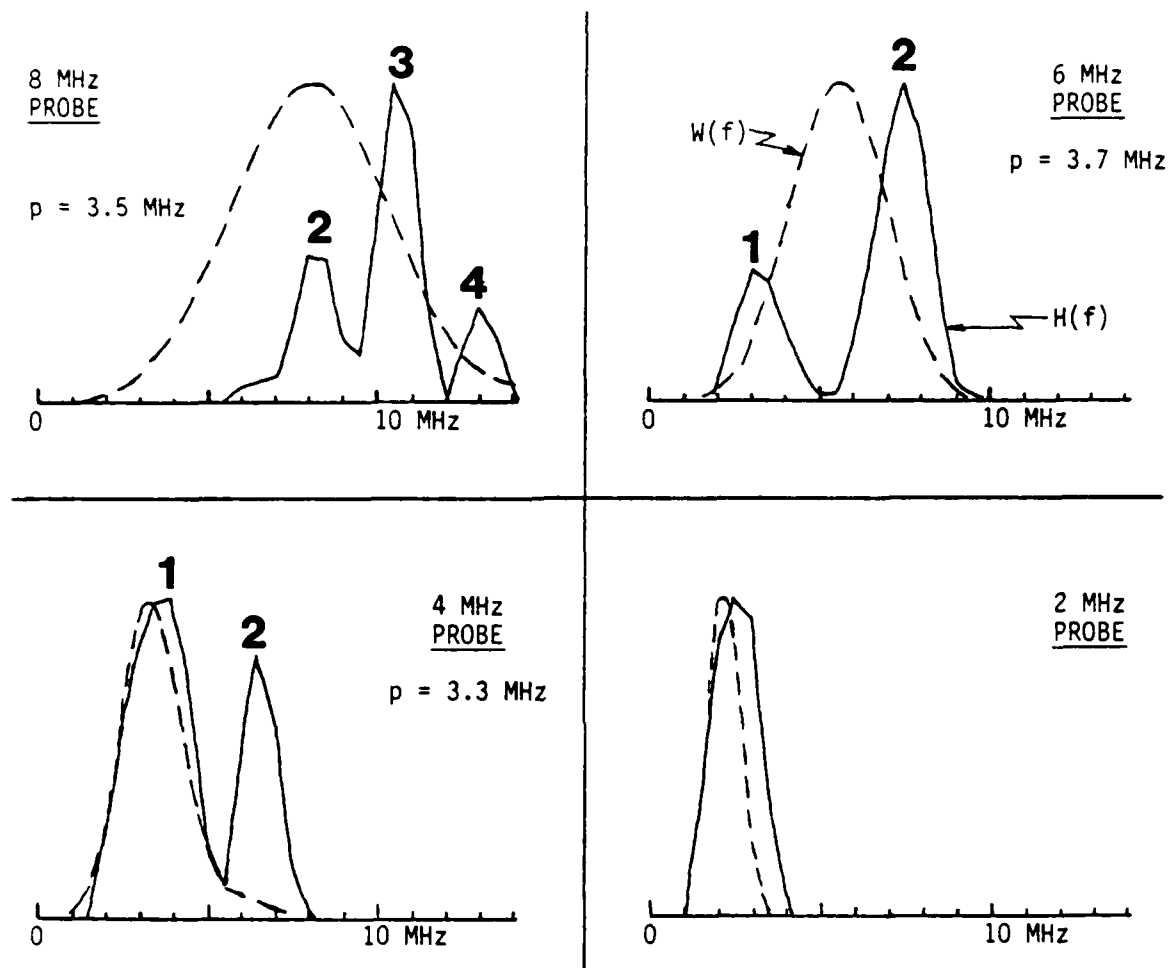
Figure 25. Magnitude Spectra Obtained for Titanium Inclusion
No. 11 With Four Longitudinal-Wave Transducers
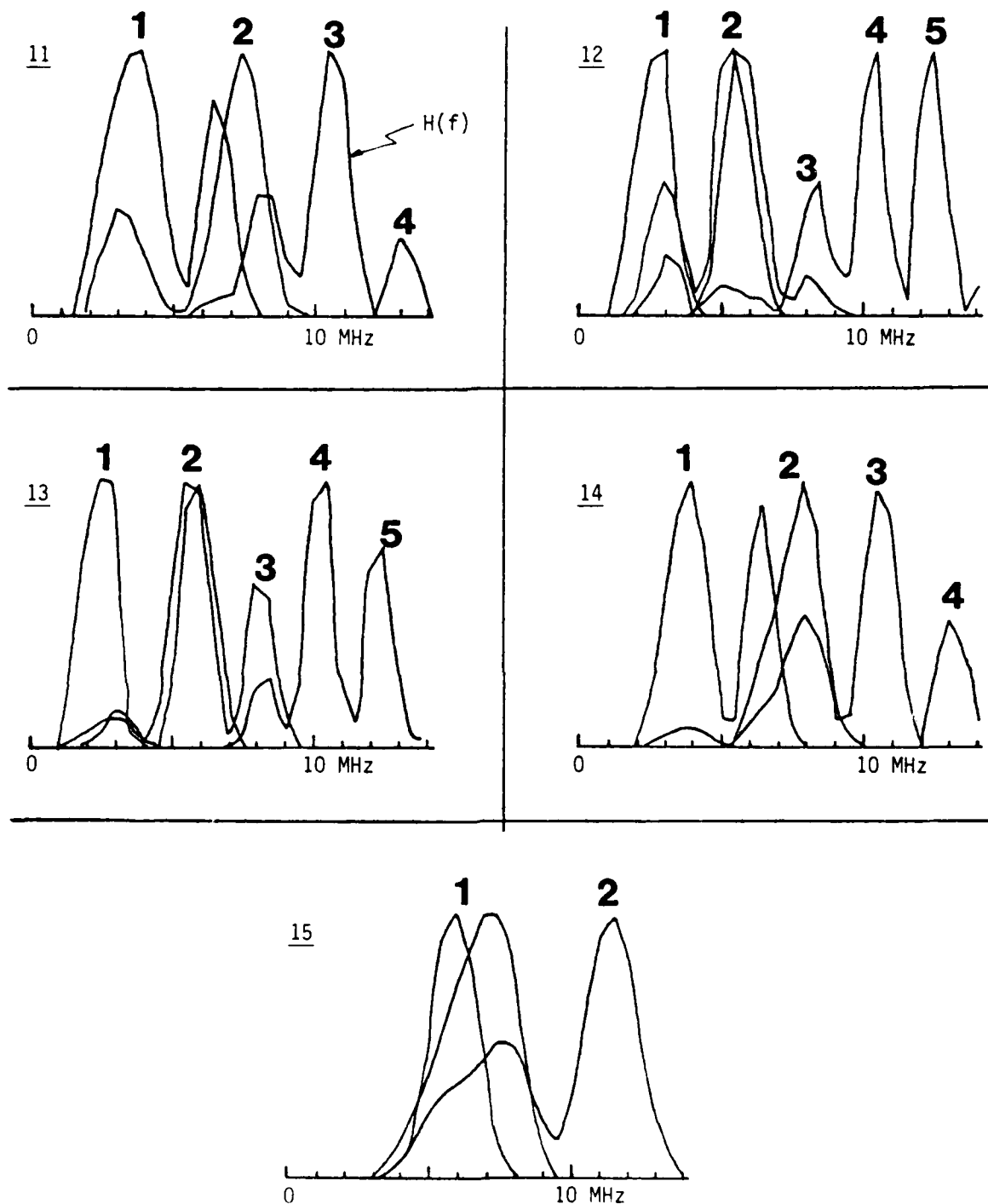
Figure 26. Application of the SST to the Inclusions in Titanium
Specimen No. FML 97416 (Flaws 11 Through 15)

47

average spectral periods listed in the last column of Table 11 by 0.7 [see Equation (2)].

6.2.3   Sapphire Inclusions in IN100 Specimens

Due mainly to the low impedance mismatch between the flaws and host material in the IN100 specimen Nos. FML 97474-1 through -8, four out of the total of 25 flaws were not detected at all, and only five flaws were detected with more than one immersion LW transducer. The low signal amplitudes, the positive polarities of the specularly reflected signals, the absence of internal echoes, and the invariance of the main features of the flaw waveform with specimen rotation have led us to conclude that these flaws are spherical sapphire inclusions.* Figure 27 contains the profiles obtained for the five sapphire inclusions that were detected more than once. The effective transducer center frequencies required by these inclusions are listed in the last column of Table 12.

6.2.4   Real Flaws in IN100 Specimens

The SST could not be applied to the manufacturing flaws in IN100 specimen Nos. FML 97600-1 and -2 because only one immersion LW transducer was effective in detecting these flaws. The magnitude spectra obtained for flaws 41 through 46 with this transducer are collected in Figure A-19.

6.3   Born Diameter Estimates

Originally, the BIT was to be applied only to the waveforms obtained with a transducer appropriate for the flaw (see the last columns in Tables

Table 11

BORN FREQUENCY ESTIMATES OBTAINED FOR THE INCLUSIONS IN
TITANIUM SPECIMEN NO. FML 97416 BY THE SST

Flaw ID No.	Transducer Center Frequency				Average Spectral Period, MHz[1]
	Low	Med. Low	Med. High	High	
11	--[2]	3.3	3.7	3.5	3.5
12	2.7	2.7	2.6	2.5	2.6
13	2.6	3.0	2.7	2.5	2.7
14	--	3.2	3.9	3.5	3.5
15	--	6.0	7.0	5.7	6.2

[1]The Born frequency for a weak inclusion (Born flaw) is given by 70 percent of the average spectral period ($F = 0.7_p$).
[2]Magnitude spectrum peaked at the transducer center frequency (feedthrough).

---

*The same conclusions were reached later by SW measurements (see Subsection 6.4).

48
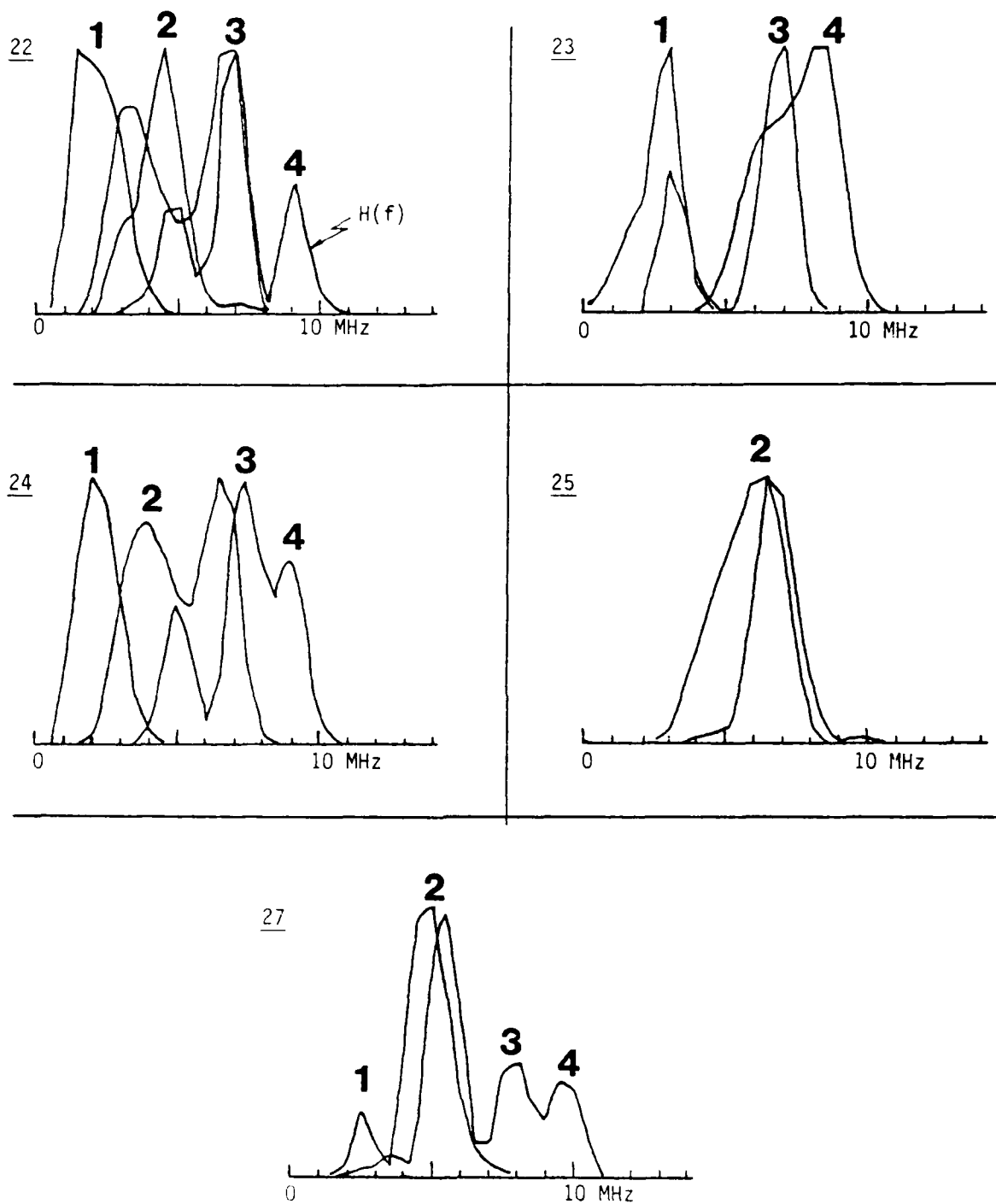
Figure 27.   Application of the SST to the Inclusions in IN100
             Specimen Nos. FML 97474-3 and 4 (Flaws 22, 23, 24,
             25, and 27)

Table 12

BORN FREQUENCY ESTIMATES OBTAINED FOR THE INCLUSIONS IN
IN100 SPECIMEN NOS. FML 97474-3 AND -4 BY THE SST

Flaw ID No.	Transducer Center Frequency			Average Spectral Period, MHz[1]
	Low	Medium	High	
22	2.2	2.2	2.3	2.2
23	2.4	2.3	2.1	2.3
24	2.2	2.2	2.2	2.2
25	--[2]	3.3	3.2	3.3
27	--	2.5	2.5	2.5

---

[1] The Born frequency for a strong inclusion (Franz flaw) is given by the average spectral period (F=p).

[2] Magnitude spectrum peaked at the effective transducer center frequency (feedthrough).

10 through 12 for the desired effective transducer center frequencies). However, for most of the flaws a transducer of the required effective center frequency was not available or efficient. It was also recognized that a large inadvertent error in the SST results would lead to a corresponding error in the Born diameter by forcing the choice of an incorrect transducer (27). For these reasons, the data acquired for a flaw with a seemingly inappropriate transducer were also inverted while still working under blind test conditions. These data are included to illustrate the criticality of the transducer selection process. To set the size estimates obtained with inappropriate transducers apart from those obtained with the SST-approved transducers, in the tables that follow the latter results are underlined. The results are presented separately for voids, WC inclusions, sapphire inclusions, and real flaws.

6.3.1   Voids in Titanium and IN100 Specimens

The desired effective transducer center frequencies for the ten voids are reproduced from Table 10 for ready reference in the second column of Table 13. Listed also in Table 13 are the nominal flaw diameters published by PWA (28) for comparison with the Born diameters obtained with three standard-frequency transducers. Note that the requirement made on the effective transducer center frequency by flaw 01 (i.e., 6 MHz) could not be met by any of the available 2-MHz, 4-MHz, and 8-MHz transducers. For this reason, two Born diameters (240 m and 470 m) are underlined for this flaw. The nominal flaw diameter (320 m) is properly bracketed by the underlined estimates because the SST estimate for F (6 MHz) was close to its expected value of 7 MHz [=2,200/320 per Equation (1)].

Table 13

BORN DIAMETER ESTIMATES OBTAINED FOR THE VOIDS IN TITANIUM
SPECIMEN NO. FML 97413 AND IN100 SPECIMEN NO. FML 97414
WITH THREE LONGITUDINAL-WAVE TRANSDUCERS

Flaw ID No.	Required Freq., MHz	Born Diameter, μm [1]			Nominal Diam., μm
		2 MHz	4 MHz	8 MHz	
01	6.0	1,000	470	240	320
02	2.0	1,030	450	250	1,000
03	2.8	990	510	250	600
04	2.6	960	530	240	780
05	1.9	1,000	560	230	1,230
06	2.8	800	540	240	600
07	1.3	970	530	210	1,230
08	5.9	1,050	440	230	320
09	2.2	910	480	240	780
10	2.3	910	440	220	1,000

[1]Size estimates obtained with the most appropriate transducers are
underlined.

Appendix B contains representative sets of amplitude spectra
(inputs to the BIA) and characteristic functions (outputs) from which the
Born diameters D (and d*) are derived in accordance with Equation (5).
Note that the narrower the amplitude spectrum (i.e., the smaller the mean
frequency f*), the broader the characteristic function (i.e., the larger
the Born diameter d*) and vice versa (see Figure B-1 for the definitions
of f* and d*). Note that the average value of the k*a* product is 0.91.

Flaw 02 is of special interest in that a transducer whose
effective center frequency coincided with the required frequency was indeed
available. The underlined Born diameter (1,030 μm) was a good size esti-
mate, but only because the deviation of the F estimate from the effective
transducer center frequency was acceptably low (2.0 vs. 2.2 MHz).

Flaw 03 is like flaw 01 in that the nominal flaw size
(600 μm) was properly bracketed by the underlined estimates (510 μm and
990 μm). Flaw 04 is also like flaw 01. Flaw 05 was underestimated because
a transducer with an effective center frequency lower than 2.2 MHz was not
available.

The results obtained for flaws 06 through 10 were similar to
those obtained for flaws 01 through 05. Note, however, that the diameter
of flaw 10 was not properly bracketed by the underlined estimates. This
casts a shadow on the reliability of the SST to serve as a transducer
selection protocol.

51

6.3.2 Tungsten Carbide Inclusions in Titanium Specimen

The effective transducer center frequencies required by the five WC inclusions in titanium specimen No. FML 97416 are reproduced from Table 11 for ready reference in the second column of Table 14. The nominal flaw diameters are listed in the last column. Flaws 11 and 14 are like flaw 01 in that the nominal flaw sizes were properly bracketed by the underlined estimates. Flaws 12 and 13 were underestimated because a transducer with an effective center frequency lower than 2.2 MHz was not available. Flaw 15 is like flaw 10 in that the flaw diameter was not properly bracketed by the underlined estimates.

6.3.3 Sapphire Inclusions in IN100 Specimens

The effective transducer center frequencies required by the eleven sapphire inclusions that were detected in IN100 specimens Nos. FML 97474-1 through -5 are listed in the second column of Table 15. The nominal flaw diameters are listed in the last column. The same type of information is included in Table 16 for the ten inclusions in IN100 specimen Nos. FML 97474-6 through -8. The transducer with an effective center frequency of 7 MHz was "discovered" after all other high-frequency immersion transducers failed to detect the vast majority of the sapphire inclusions. All four flaws that even this efficient transducer could not find (i.e., flaws 17, 18, 28, and 30) were small (410 μm).

Flaw 16 is one of the sixteen sapphire inclusions that only the 7-MHz immersion LW transducer could detect. Because the SST broke down for flaws 16, 26, 32, 34, and 37 (see Figures A-15 through A-17, the required frequencies listed in Tables 15 and 16 for these 410-μm diameter flaws were questionable. The Born diameters for these flaws were, therefore, underlined with caution.

Table 14

BORN DIAMETER ESTIMATES OBTAINED FOR THE INCLUSIONS IN TITANIUM SPECIMEN NO. FML 97416 WITH FOUR LONGITUDINAL-WAVE TRANSDUCERS

Flaw ID No.	Required Freq., MHz	Born Diameter, μm[1]				Nominal Diam., μm
		2 MHz	4 MHz	6 MHz	8 MHz	
11	2.5	960	580	490	230	900
12	1.8	900	570	410	250	1,210
13	1.9	910	610	390	200	1,210
14	2.5	900	540	420	250	900
15	4.3	940	410	340	300	480

---

[1]Size estimates obtained with the most appropriate transducers are underlined.

Table 15

BORN DIAMETER ESTIMATES OBTAINED FOR THE INCLUSIONS IN IN100 SPECIMEN
NOS. FML 97474-1 THROUGH -5 WITH THREE LONGITUDINAL-WAVE TRANSDUCERS

Flaw ID No.	Required Freq., MHz	Born Diameter, μm[1]			Nominal Diam., μm
		2 MHz	4 MHz	7 MHz	
16	6.8	--[2]	--	260	410
19	3.2	--	--	270	790
20	3.2	--	--	290	790
21	3.1	--	--	310	790
22	2.2	1,030	450	280	990
23	2.3	1,160	510	410	990
24	2.2	1,230	460	280	990
25	3.3	--	430	280	790
26	6.3	--	--	310	410
27	2.5	--	480	320	990
29	3.3	--	--	270	790

[1] Size estimates obtained with the most appropriate transducers are underlined.
[2] Ineffecient transducer (no signal from flaw).

Table 16

BORN DIAMETER ESTIMATES OBTAINED FOR THE INCLUSIONS IN IN100 SPECIMEN
NOS. FML 97474-6 THROUGH -8 WITH A 7 MHz LONGITUDINAL-WAVE TRANSDUCER

Flaw ID No.	Required Freq., MHz	Diameter, μm	
		Born[1]	Nominal
31	2.0	390	990
32	6.3	280	410
33	2.3	300	990
34	3.7	290	410
35	3.4	280	790
36	2.7	290	990
37	7.0	260	410
38	3.3	270	790
39	2.5	300	990
40	3.3	280	790

[1] Size estimates obtained with an SST-approved transducer are underlined.

Flaw 19 is one of the seven 790-μm diameter inclusions that only the 7-MHz transducer could detect.* In spite of this, the SST did not break down for flaws 19, 20, 21, 29, 35, 38, and 40 (see Figures A-15 through A-18) so that the required frequencies listed in Tables 15 and 16 for these flaws were considered accurate. The same is, of course, true for flaw 25 (see Figure 27).

Flaw 22 is one of the three 990-μm diameter inclusions that all three transducers could detect. These flaws are like many voids and WC inclusions in that the flaw sizes were properly bracketed by the under-lined Born diameters.

Flaw 27 is one of the five 990-μm diameter inclusions that only the 7-MHz transducer could find. Nevertheless, the SST did not break down for flaws 27, 31, 33, 36, and 39 (see Figures A-16 through A-18) so that the required frequencies listed in Tables 15 and 16 for these flaws were considered accurate.

6.3.4 Real Flaws in IN100 Specimens

The effective transducer center frequencies required by the six real flaws in IN100 specimen Nos. FML 97600-1 and -2 are listed in the second column of Table 17. These SST estimates were suspect, however, because only the 7-MHz transducer could find these flaws and the resulting magnitude spectra were unmodulated (see Figure A-19). The Born diameters were, therefore, underlined with caution.

Table 17

BORN DIAMETER ESTIMATES OBTAINED FOR THE REAL FLAWS IN IN100 SPECIMEN
NOS. FML 97600-1 and -2 WITH A 7 MHz LONGITUDINAL-WAVE TRANSDUCER

Flaw ID No.	Required Freq., MHz	Born Diam., μm [1]	Actual Flaw Dimensions, μm
41	8.5	270	140 x 610 x 110
42	7.3	250	150 x 230 x 150
43	7.3	260	--(2)
44	7.1	280	370 x 500 x 90
45	8.3	280	--
46	7.2	260	--

[1]Size estimates obtained with the SST-approved transducer are underlined.
[2]Flaw has not been metallurgically sectioned.

*Only one other flaw of this size (flaw 25) could also be found with another transducer.

None of the characteristics of these flaws were known (28). For this reason, three randomly selected flaws (41, 42, and 44) were metallographically sectioned. No less than twelve nearly equally spaced sections were made on each flaw to determine its shape, size, and orientation. The maximum linear dimensions found on sequential polishing are recorded in the last column of Table 17. The underlined Born diameters appear to be bracketed by the minimum and maximum flaw dimensions. Flaw orientations and dimensions in the line of sight had no effect on the Born diameters.

The metallographic sectioning procedures were directed not only at verifying the presence of the flaws and determining their shape, size, and orientation, but also at determining the flaw compositions. Scanning electron microscopy (SEM) analysis revealed magnesium-rich regions for flaw 41 and aluminum-rich regions for flaw 42. Flaw 44 was determined to be a void. Flaw compositions had no apparent effect on the Born diameters.
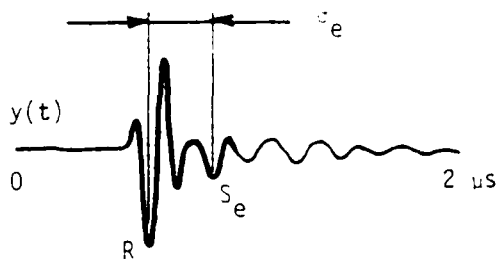
6.4 SPOT Size Estimates

The satellite-pulse observation technique was applied to the traveling composite waveforms (i.e., the doublet trains) obtained by scanning the specimens in the area of the detected flaw with high-frequency immersion (or contact) LW (or SW) transducers. The pulse separation (σ) measurements were made directly from the oscilloscope traces by examiners trained in the principles and application of the amplitude- and phase-comparison techniques and the SPOT. The examiners' most difficult tasks were to select the most appropriate physical model for the flaw being examined and to discriminate against ghost satellites (material noise and bondplane echoes). The selection of the proper physical model prior to the interpretation of σ measurements in terms of flaw dimensions is analogous to the selection of the proper transducer prior to the acquisition of the data for the BIT. The SPOT size estimates are presented separately for voids, WC inclusions, sapphire inclusions, and real flaws.

6.4.1 Voids in Titanium and IN100 Specimens

Shear-wave amplitude and phase measurements confirmed the conclusions drawn from LW measurements in Paragraph 6.2.1 that the flaws in specimen Nos. FML 97413 and 97414 are spherical voids. A complete set of typical raw waveforms for flaws 01 through 10 is included in Appendix C (see Figures C-1 through C-4). The LW composite waveforms ("signatures") for flaws 03 and 08 are reproduced from Figures C-1 and C-3, respectively, for ready reference in the upper part of Figure 28. The SW signatures of these flaws are reproduced from Figures C-2 and C-4 for ready reference in the upper part of Figure 29. The heavy trace in each signature marks the beginning and the end of the pulse train (i.e., the R and the S_e pulses) against the background of irrelevant indications (light trace). The LW train for flaw 03 (d_n = 600 μm)* was 285 ns long which translates into a size estimate of 620 m [see Equation (7)]. The SW train for this flaw was 620 ns long, giving 710 μm for the size estimate [see Equation (8)].
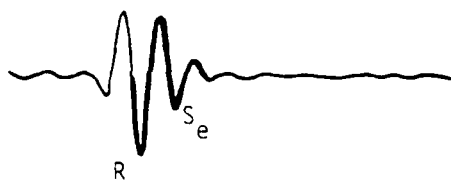
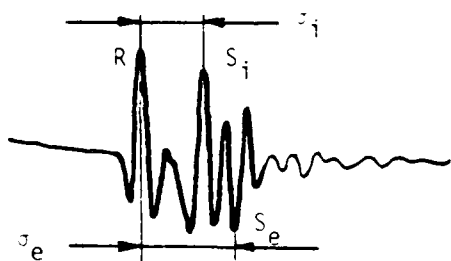---

*Nominal diameter.

FLAW WAVEFORM

$y(t)$

σ_e

0   2 μs

R S_e

VOID 03 - 600 μm

σ_e = 285 ns   d = 620 μm

S_e

R

VOID 08 - 320 μm

σ_e = 160 ns   d = 350 μm

R S_i

σ_i

σ_e S_e

INCLUSION 11 - 900 μm

σ_i = 275 ns   d = 910 μm

σ_e = 425 ns   d = 930 μm

R

S_e

INCLUSION 25 - 790 μm

σ_e = 360 ns   d = 790 μm

R

S_e
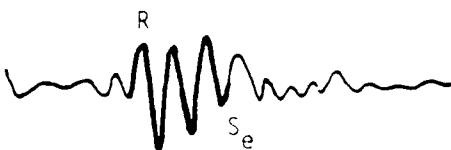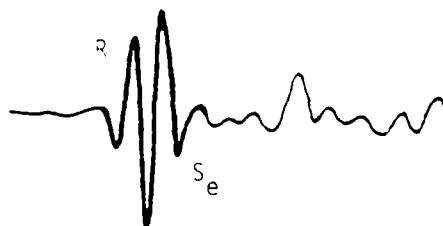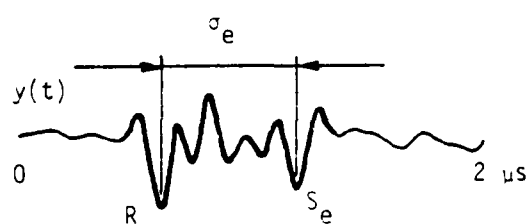
FLAW 44 - 370 x 500 x 90 μm

σ_e = 200 ns   d = 440 μm
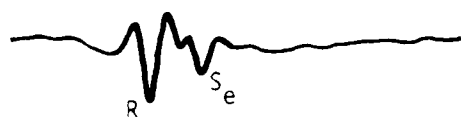
Figure 28. Longitudinal-Wave Signatures of Selected Test Flaws

56

FLAW WAVEFORM

VOID 03 - 600 μm
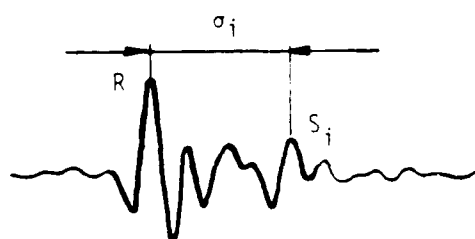
σ_e = 620 ns   d = 710 μm

VOID 08 - 320 μm

σ_e = 240 ns   d = 280 μm

INCLUSION 11 - 900 μm

σ_i = 625 ns   d = 910 μm

INCLUSION 25 - 790 μm

σ_e = 685 ns   d = 790 μm
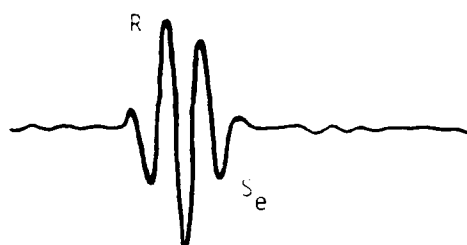
FLAW 44 - 370 x 500 x 90 μm

σ_e = 320 ns   d = 370 μm

Figure 29.   Shear-Wave Signatures of Selected Test Flaws

57

Flaw 08 (d_n = 320 μm) was difficult to size due to the presence of an unexpected, yet unidentified flaw in the vicinity of the intentionally placed void. The unexpected asynchronous dynamic curves for the first and last echoes in the pulse trains (15) gave evidence of the unintentional flaw (see the extra positive half-cycle at the beginning of the LW train in the second trace of Figure 28). Shear waves were more successful than longitudinal waves in isolating and subsequently sizing the void (see second trace in Figure 29). The LW and SW size estimates were 350 μm and 280 μm, respectively.

Typical LW and SW signatures for the other eight voids are shown in Figures C-1 through C-4. The averages of many size estimates obtained for the same void by varying the frequency, wave mode, beam angle, and observation direction are listed in Table 18.

6.4.2 Tungsten Carbide Inclusions in Titanium Specimen

Shear-wave amplitude and phase measurements confirmed the flaws in titanium specimen No. FML 97416 to be spherical WC inclusions. A complete set of raw LW and SW signatures for flaws 11 through 15 is included in Figures C-5 and C-6. The LW and SW signatures for inclusion 11 are included in Figures 28 and 29, respectively, for ready reference. The LW train attests to the simultaneous production of external and internal satellite pulses (S_e and S_i, respectively). The "internal" LW train

Table 18

SIZE ESTIMATES OBTAINED FOR THE VOIDS IN TITANIUM SPECIMEN NO. FML 97413 and IN100 SPECIMEN NO. FML 97414 BY THE SATELLITE-PULSE OBSERVATION TECHNIQUE (SPOT)

Flaw ID No.	SPOT Diameter, μm		Nominal Diam., μm
	External LW Satellites[1]	External SW Satellites[2]	
01	460	370	320
02	980	1,030	1,000
03	790	700	600
04	850	750	780
05	1,180	1,410	1,230
06	640	580	600
07	1,450	1,470	1,230
08	350	280	320
09	860	770	780
10	1,100	1,160	1,000

[1]The velocity of external longitudinal waves circumventing the voids was determined to be 5.3 km/sec.

[2]The velocity of external shear waves circumventing the voids was determined to be 2.9 km/sec.

for flaw 11 (d_n = 900 ..m) was 275 ns long, giving 910 ..m for the size esti-
mate [see Equation (9)]. The "external" LW train for this flaw was 425 ns
long, giving 930 μm for the size estimate [see Equation (7)]. The "inter-
nal" SW train for this flaw was 625 ns long, giving 910/μm for the size
estimate [see Equation (10].

Typical LW and SW signatures for the other four WC inclu-
sions are shown in Figures C-5 and C-6. The averages of many size esti-
mates obtained for the same inclusion by varying the frequency, wave mode,
beam angle, and observation direction are listed in Table 19.

6.4.3   Sapphire Inclusions in IN100 Specimens

Shear-wave amplitude and phase measurements identified the
flaws in IN100 specimen Nos. FML 97474-1 through -8 to be spherical sap-
phire inclusions. A complete set of raw LW and SW signatures for flaws 16
through 40 is included in Figures C-7 through C-13. The LW and SW signa-
tures for inclusion 25 are included in Figures 28 and 29, respectively,
for ready reference. The LW train for flaw 25 (d_n = 790 μm) was 360 ns
long, giving 790 μm for the size estimate [see Equation (7)]. The SW
train for this flaw was 685 ns long, giving 790 μm for the size estimate
[see Equation (8)].

Typical LW and SW signatures for the other twenty sapphire
inclusions are shown in Figures C-7 through C-13. The averages of many
size estimates obtained for the same inclusion by varying the frequency,
wave mode, beam angle, and observation direction are listed in Tables 20
and 21.

Table 19

SIZE ESTIMATES OBTAINED FOR THE INCLUSIONS IN TITANIUM SPECIMEN
NO. FML 97416 BY THE SPOT

Flaw ID No.	SPOT Diameter, ..m			Nominal Diam., μm
	Internal LW Satellites[1]	External LW Satellites[2]	Internal SW Satellites[3]	
11	920	930	920	900
12	1,160	1,180	1,150	1,210
13	1,170	1,160	1,140	1,210
14	910	940	930	900
15	520	480	530	480

[1]The velocity of internal longitudinal waves in the tungsten carbide
inclusion was assumed to be 6.6 km/sec (a published value).
[2]The velocity of external longitudinal waves circumventing the WC inclu-
sions was determined to be 5.3 km/sec.
[3]The velocity of internal shear waves in the WC inclusions was determined
to be 2.9 km/sec.

Table 20

SIZE ESTIMATES OBTAINED FOR THE INCLUSIONS IN IN100 SPECIMEN
NOS. FML 97474-1 THROUGH -5 BY THE SPOT

| Flaw ID No. | SPOT Diameter, μm | | Nominal Diam., μm |
	External LW Satellites[1]	External SW Satellites[2]	
16	420	--[3]	410
19	800	--	790
20	800	--	790
21	790	--	790
22	1,170	1,210	990
23	1,070	1,120	990
24	1,070	1,160	990
25	790	790	790
26	410	--	410
27	990	1,080	990
29	800	760	790

[1] The velocity of external longitudinal waves circumventing the sapphire inclusions was assumed to be 5.3 km/sec.

[2] The velocity of external shear waves circumventing the sapphire inclusions was assumed to be 2.9 km/sec.

[3] No signal from inclusion.

Table 21

SIZE ESTIMATES OBTAINED FOR THE INCLUSIONS IN IN100
SPECIMEN NOS. FML 97474-6 THROUGH -8 BY THE SPOT

| Flaw ID No. | SPOT Diameter, μm | | Nominal Diam., μm |
	External LW Satellites[1]	External SW Satellites[2]	
31	990	1,010	990
32	410	220	410
33	1,010	930	990
34	410	380	410
35	800	830	790
36	990	1,030	990
37	410	210	410
38	780	--[3]	790
39	1,010	980	990
40	770	720	790

[1] The velocity of external longitudinal waves circumventing the sapphire inclusions was assumed to be 5.3 km/sec.

[2] The velocity of external shear waves circumventing the sapphire inclusions was assumed to be 2.9 km/sec.

[3] No signal from inclusion.

6.4.4 Real Flaws in IN100 Specimens

A complete set of raw LW and SW signatures for flaws 41 through 46 is included in Figures C-14 and C-15. The LW and SW signatures for flaw 44 are included in Figures 28 and 29, respectively, for ready reference. The LW train for flaw 44 (maximum linear dimensions = 370 x 500 x 90 μm) was 200 ns long, giving 440 μm for the equivalent diameter* [see Equation (7)]. The SW train for this flaw was 320 ns long, giving 370 μm for the equivalent diameter [see Equation (8)].

Typical LW and SW signatures for the other five real flaws are shown in Figures C-14 and C-15. The averages of many size estimates obtained for the same flaw by varying the frequency, wave mode, beam angle, and observation direction are listed in Table 22.

6.5 Semiautomated Satellite Analysis Procedures (SSAP) Size Estimates

The SPOT relies heavily on the expertise of the ultrasonic examiner to extract signal parameters from an A-scan display. The satellite pulses are usually of low amplitude and are often hard to detect due to material noise. The traces [raw flaw waveforms $y(t)$] in Figure 30 reveal the difficulties facing the examiner in recognizing the associated pulses in $y(t)$ and interpreting their separations τ from the R pulse in terms of flaw size "on the spot." Even a highly trained SPOT examiner has difficulties

Table 22

SIZE ESTIMATES OBTAINED FOR THE REAL FLAWS IN IN100
SPECIMEN NOS. FML 97600-1 AND -2 BY THE SPOT

Flaw ID No.	SPOT Diameter, μm		Actual Flaw Dimensions, μm
	External LW Satellites[1]	External SW Satellites[2]	
41	380	410	140 x 610 x 110
42	390	380	150 x 230 x 150
43	390	320	--(3)
44	440	390	370 x 500 x 90
45	400	240	--
46	390	220	--

[1]The velocity of external longitudinal waves circumventing the flaws was assumed to be 5.3 km/sec.
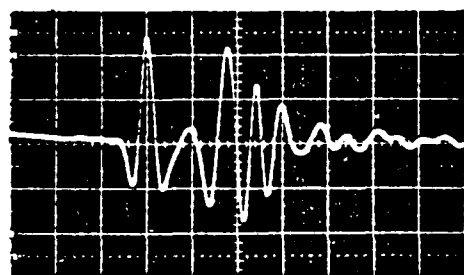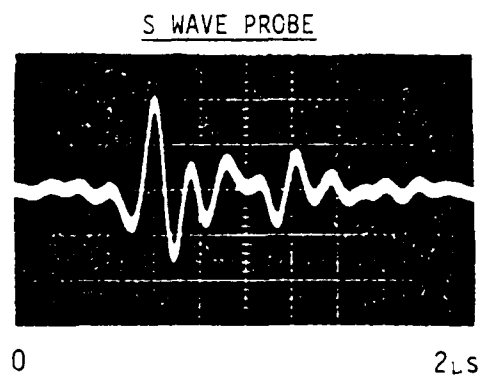
[2]The velocity of external shear waves circumventing the flaws was assumed to be 2.9 km/sec.
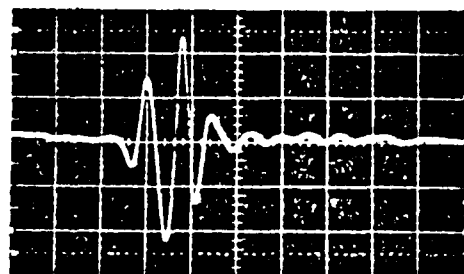
[3]Flaw has not been metallurgically sectioned.

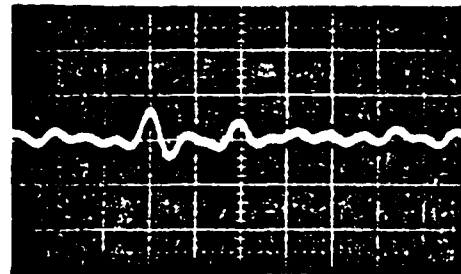*The irregular flaws were modeled as strongly scattering spheres and sized in terms of equivalent diameters.
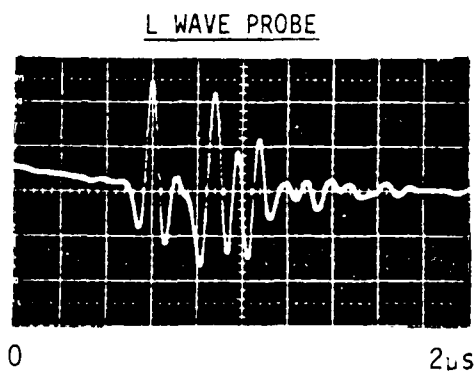
Figure 30. Longitudinal- and Shear-Wave Signatures of
Tungsten Carbide Inclusions 11, 12, and 15

in determining where the pulse train begins and ends for some flaws. In contrast, Figure 31 reveals the ease with which the spectrum periodicities p and P and, subsequently, the flaw sizes can be obtained from the flaw profiles. The automatic detection and interpretation of the periodicities clearly present in H(f) is a significant step toward eliminating the need for a highly trained examiner in the inspection loop (29). The semiautomated satellite analysis procedures (SSAP) detailed in Table 23 are the first step in automating the SPOT to make its use practical by less skilled ultrasonic examiners. Better pulse resolution can be achieved not only by using shear as well as longitudinal waves, but also by deconvolving y(t) with r(t) (i.e., its own front-surface echo). Not only can the spectrum periodicities be read easier than the pulse separations, but the accuracy of p/P measurements is also improved over that of σ measurements.

In generating the data shown in Tables 24 through 26 for the 32 detectable inclusions, the SW measurements were used to confirm the physical model applied to and the size estimates derived from the LW measurements. A complete set of profiles for these inclusions is contained in Appendix D.

Table 23

EXPERIMENTAL PROTOCOL FOR THE SEMIAUTOMATED SATELLITE ANALYSIS PROCEDURES (SSAP)

Step	Description
1	Record flaw waveform y(t) with any high-frequency LW transducer
2	Digitize and store y(t)
3	Gate out the R pulse of y(t) to serve as reference waveform r(t)
4	Digitize and store r(t)
5	Deconvolve y(t) with r(t)
6	Determine periodicity p of magnitude spectrum H(f) in MHz
7	Classify flaw as strong (void or sapphire) or weak (WC)
8	Estimate flaw size in μm by 2,180/p (strong flaw) or 3,300/p (weak flaw)
9	Repeat steps 1 through 7 with any high-frequency SW transducer
10	Estimate flaw size in μm by 1,150/P (strong flaw) or 1,450/P (weak flaw)

L WAVE PROBE

S WAVE PROBE

11

P = 1.6 MHz

H(f)

p = 3.5 MHz

2

1

3

0   10 MHz

3 4 5 6 7 8

0   10 MHz

p = 2.6 MHz

12

7

3

2

4

1

0   10 MHz

P = 1.3 MHz

6

8 9

0   10 MHz

15

1

p = 7.3 MHz

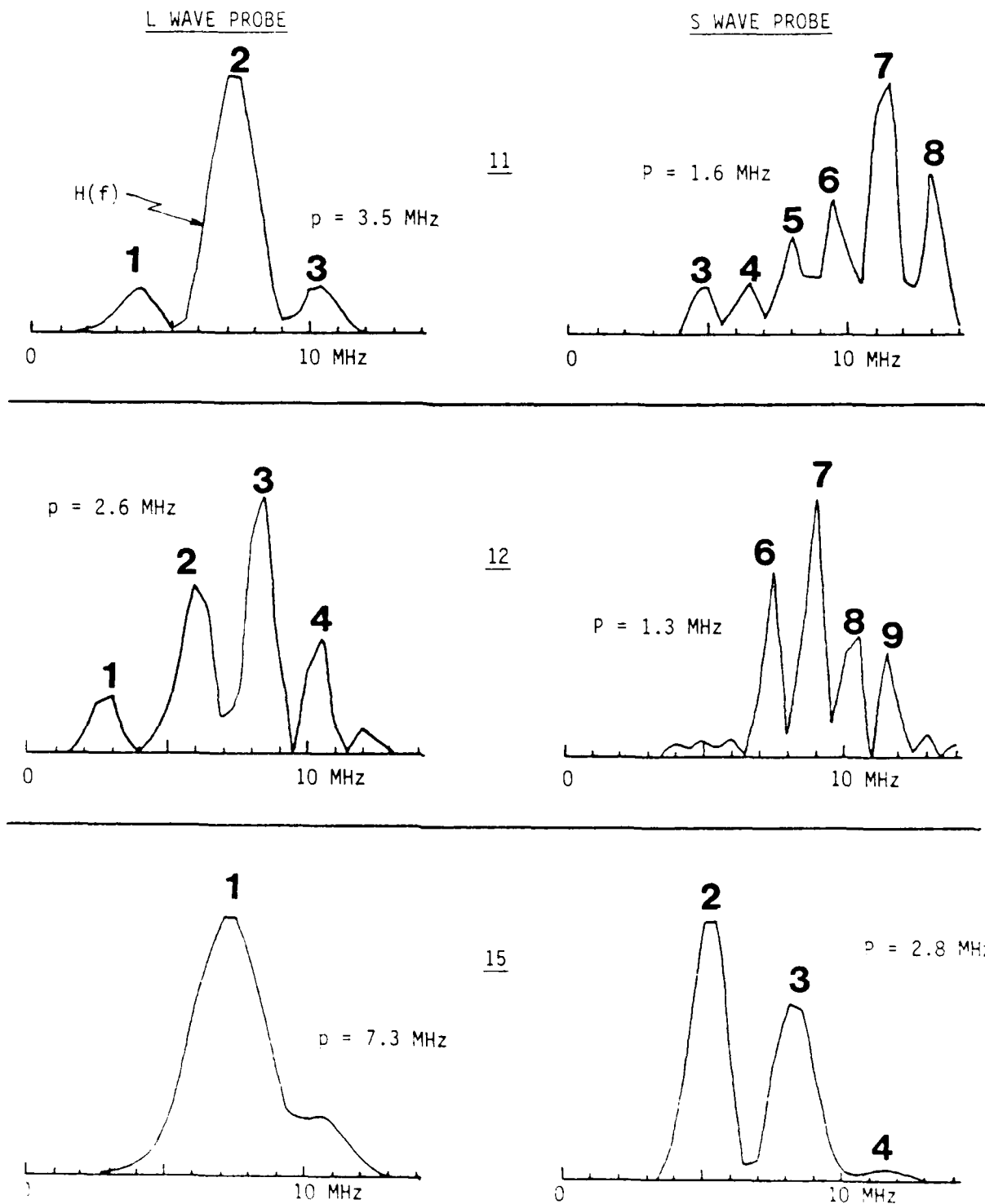0   10 MHz

2

3

p = 2.8 MHz

4

0   10 MHz

Figure 31. Longitudinal- and Shear-Wave Profiles of Tungsten
Carbide Inclusions 11, 12, and 15

Table 24

SIZE ESTIMATES OBTAINED FOR THE INCLUSIONS IN TITANIUM SPECIMEN NO. FML 97416 BY THE SSAP

Flaw ID No.	SSAP Diameter, ,m		Nominal Diam., ,m
	L Waves[1]	S Waves[2]	
11	940	910	900
12	1,270	1,120	1,210
13	1,220	1,120	1,210
14	940	910	900
15	450	520	480

[1]High-frequency contact transducer.
[2]High-frequency immersion transducer.

Table 25

SIZE ESTIMATES OBTAINED FOR THE INCLUSIONS IN IN100 SPECIMEN NOS. FML 97474-1 THROUGH -8 BY THE SSAP

Flaw ID No.	Diameter, ,m		Flaw ID No.	Diameter, ,m	
	SSAP[1]	Nominal		SSAP[1]	Nominal
16	520	410	31	1,100	990
19	690	790	32	470	410
20	670	790	33	1,100	990
21	650	790	34	510	410
22	1,100	990	35	730	790
23	1,050	990	36	1,050	990
24	960	990	37	440	410
25	690	790	38	690	790
26	500	410	39	1,100	990
27	920	990	40	710	790
29	710	790			

[1]High-frequency contact LW transducer.

Table 26

SIZE ESTIMATES OBTAINED FOR THE REAL FLAWS IN IN100 SPECIMEN
NOS. FML 97600-1 AND -2 BY THE SSAP

Flaw ID No.	SSAP Diam., μm[1]	Actual Flaw Dimensions, μm
41	230 - 450	140 x 610 x 110
42	220 - 430	150 x 230 x 150
43	250 - 500	--[2]
44	260 - 520	370 x 500 x 90
45	250 - 500	--
46	240 - 480	--

---

[1]High-frequency contact LW transducer.
[2]Flaw has not been metallurgically sectioned.

7. DISCUSSION

7.1 General

In this section, the size estimates obtained under blind test conditions for the 42 detected flaws by the primary and the additional flaw characterization procedures are discussed. The Born inversion procedures and those based on the detection of associated pulses (i.e., the SPOT and SSAP) differ fundamentally because the former procedures attempt to determine the flaw size solely from the parameters of the front-surface echo (1,22,24).

7.2 Born Inversion Procedures

As shown in Table 4, the BIT needs supplementation by the SST which, in turn, uses the results of the amplitude- and phase-comparison techniques as well as those of deconvolution in selecting the most appropriate transducer(s) to use in the acquisition of waveforms for Born inversion. The amplitude- and phase-comparison techniques were successfully applied to the raw flaw waveforms obtained with the high-frequency LW transducers. All 36 detectable flaws in the diffusion-bonded test specimens were correctly identified as spherical voids, WC inclusions, or sapphire inclusions. The appropriateness of an LW transducer for inclusion into the Born measurement protocol was determined by preliminary examination of the resulting deconvolved flaw spectrum [magnitude spectrum $H(f)$]. A transducer whose spectral response $W(f)$ encompassed more than one of the flaw's resonance peaks was declared inappropriate for acquiring Born inversion data. Flaw 02 serves to illustrate this transducer selection protocol. All of the high-frequency probes used to interrogate this flaw were considered inappropriate (see Figure 22). Note that the bandwidth of the selected 2-MHz transducer is well centered on the first peak of $H(f)$.

When none of the available transducers' bandwidth was centered on the flaw's fundamental (n=1) resonance frequency, two transducers were considered appropriate for acquiring Born inversion data. Flaws 01 and 03 serve to illustrate this transducer selection protocol. Both the 4-MHz and 8-MHz transducers* were considered appropriate for flaw 01 because the Born frequency was estimated to be 6 MHz. A Born frequency estimate of 2.8 MHz influenced the selection of the 2-MHz and 4-MHz transducers for flaw 03. Because a large error in the F estimate by the SST could have led to an unacceptable error in the D estimate by the BIT, Born inversions were performed for the waveforms acquired for a given flaw by all three standard-frequency transducers. However, only those Born diameters that were obtained with the SST-approved transducers are underlined in Tables 25 hrough 29.

The BIT yielded size estimates (D) with large inaccuracy for the 15 voids and WC inclusions as well as nine of the sapphire inclusions for

---

*The effective center frequencies of the available 2.25, 5, and 10 MHz transducers were approximately 2, 4, and 8 MHz, respectively.

which at least one transducer with an effective center frequency near the flaw's fundamental resonance was available (coincidence rule). Figure 32 shows that the correlation of the Born diameters with the nominal flaw sizes is barely significant (correlation coefficient 0.81). The sizing errors for the 24 flaws were such that 310 ..m (12 mils) need to be added to D in order to be almost certain (i.e., 95 percent sure) that the actual flaw size does not exceed this conservative size estimate.

The Born diameters were determined to be independent of flaw composition, size, and shape, but linearly related to the period of the ultrasonic wave (T) according to the equation

$$D = 1.95 \ T \tag{11}$$

where D is in micrometers and T is in nanoseconds. This relationship was found empirically by plotting the averages of the 37 Born diameters underlined in Tables 13 through 17 against the effective wave periods (see Figure 33). Equation (11) can be better understood following the derivation of the coincidence rule formulated in the time domain. It can be shown (see Table 27) that the bandwidth requirement for the Born transducer (i.e., 0.5<ka<2.5) reduces to

$$T = \sigma_e \tag{12}$$

Matching the transducer center frequency to the flaw's fundamental resonance frequency thus guarantees the smooth blending of the external satellite pulse, if one is produced, into the natural ringdown (decay) of the front-surface echo (R pulse). This explains why the presence of the satellite pulse of a strongly scattering flaw is not apparent when the flaw waveform is acquired with the "proper" transducer. Since the separation of the third half-cycle from the first half-cycle (R pulse) in the flaw waveform acquired by the Born transducer is equal to T, the BIA treats the third half-cycle in y(t) as if it were the external satellite pulse. The algorithm does not actually need a satellite pulse as long as the ringdown of the R pulse lasts for at least one period (i.e., for two more half-cycles).

Table 27

DERIVATION OF THE TIME-DOMAIN COINCIDENCE RULE FOR A STRONG SCATTERER

Quantity	Equation	Remarks
Born bandwidth	$0.5<ka<2.5$	Transducer selection
Born wave number	$Ka = (0.5 \times 2.5)^{1/2} = 1.1$	Geometric mean
Born frequency	$F = 1.1c/\pi d$	$f = kc/2\pi$
Born period	$T = 2.8 \ d/c$	$T = 1/F$
Pulse separation	$\sigma_e = 2.8 \ d/c$	Equation (6)
Coincidence rule	$T = \sigma_e$	Creeping wave reinforces reflected wave (constructive interference)

68
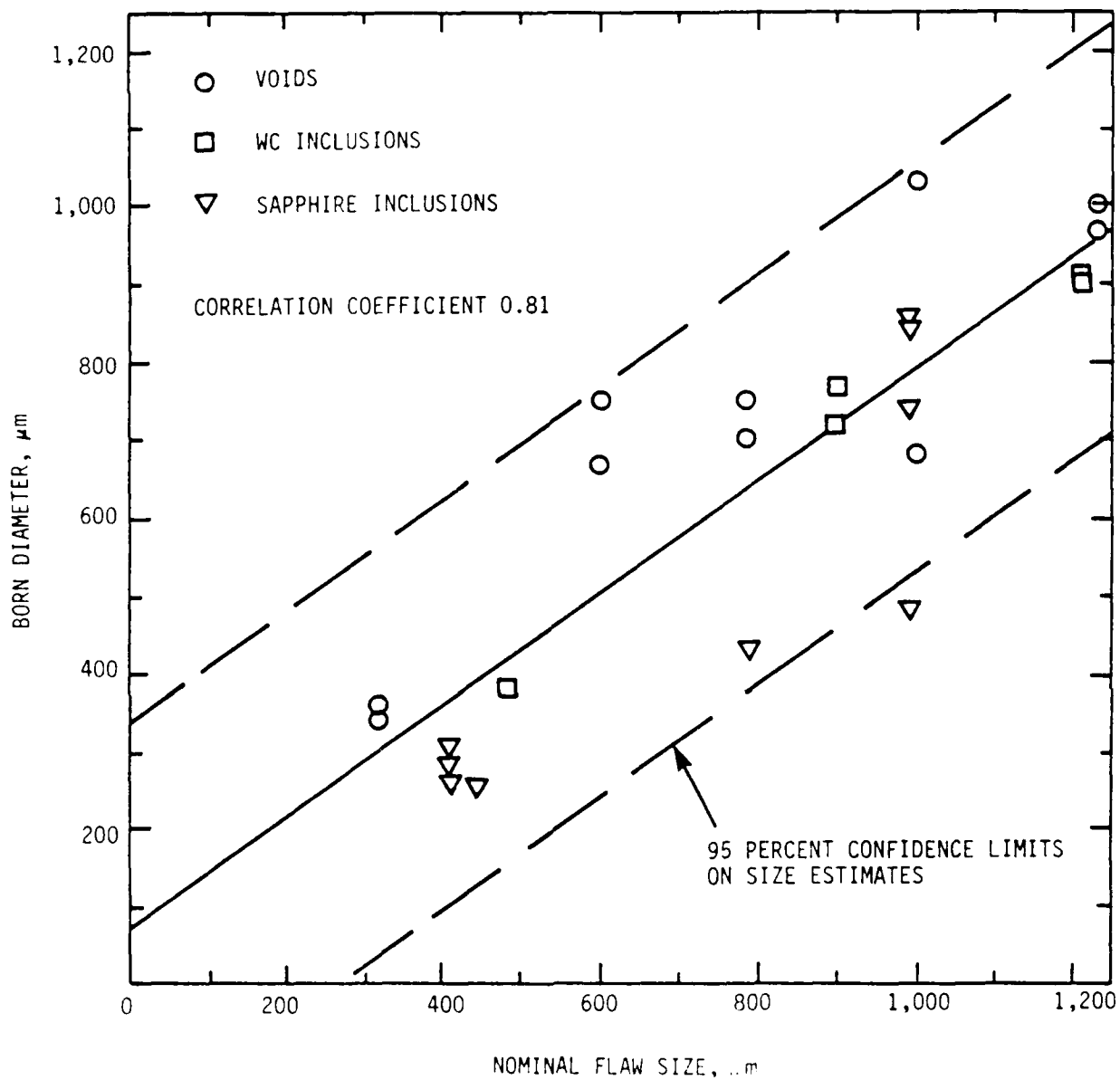
Figure 32. Correlation of Nominal Flaw Sizes With Estimates Obtained by the Born Inversion Procedures (BIP)
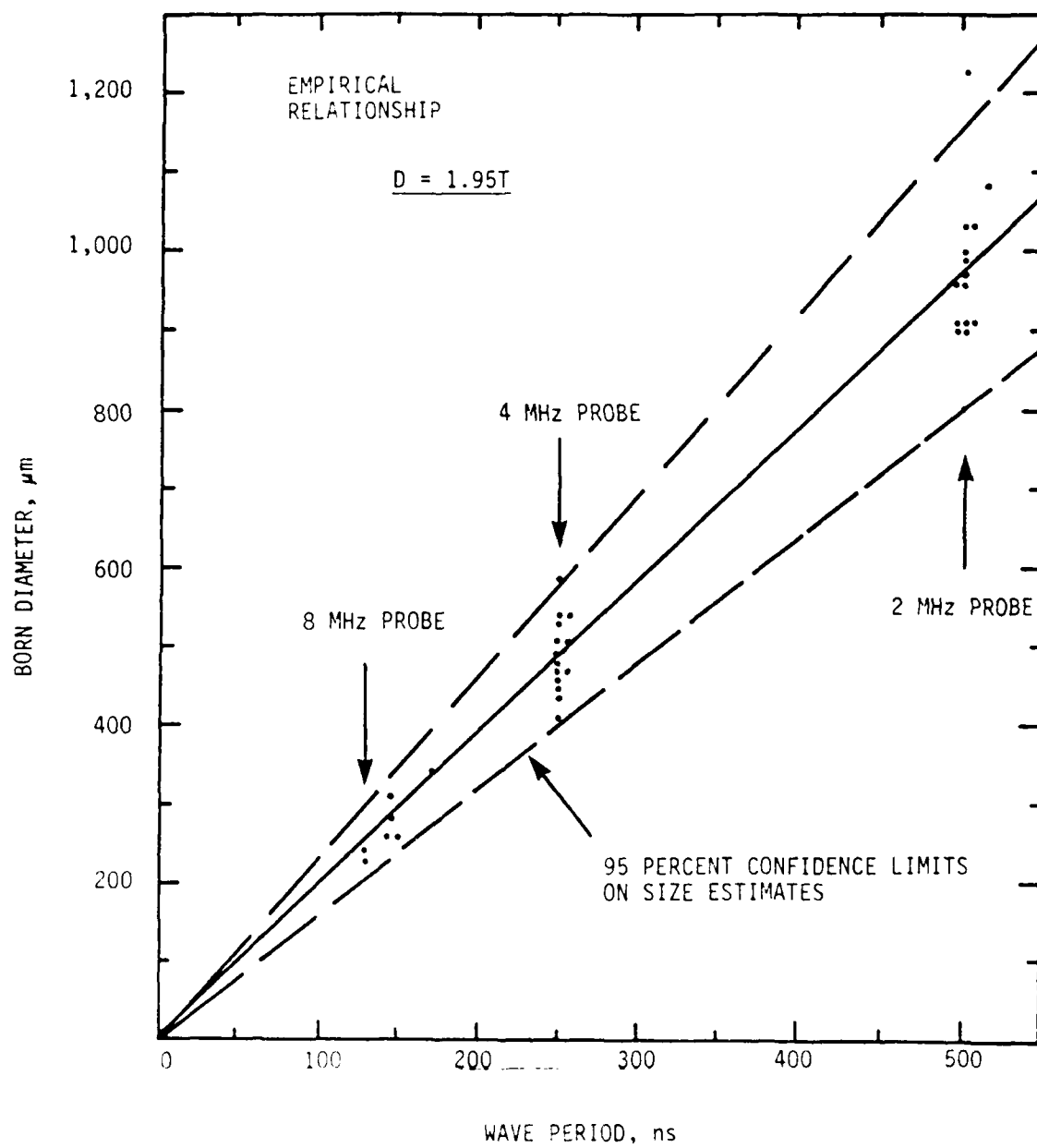
Figure 33. Correlation of Wave Period With Estimates Obtained by the BIP

The raw waveforms obtained for the five titanium voids with high-frequency LW transducers and displayed in Figure C-1 illustrate the compliance (and noncompliance) with the time-domain coincidence rule. Note that in each case the ringdown of the R pulse is no less than two half-cycles. For all but flaw 01 (d_n = 320 m), the coincidence rule was grossly violated ($\sigma_e > 2T$). Only for this flaw does the third half-cycle in y(t) coincide with the external satellite pulse (ESP) which is separated from the R pulse by $T = \sigma_c = 150$ ns. The Born diameter for this flaw is calculated by Equation (11) to be 290 m, and the SPOT diameter is calculated by Equation (7) to be 330 m. The essence of the transducer selection protocol for the BIP is to increase the period of the wave for the other four voids whose signatures are displayed in Figure C-1 until the second half-cycle following the R pulse coincides with the arrival of the ESP.

Figures 14 through 17 contain the impulse responses h(t) obtained for the standard (800-m diameter) void with four LW transducers. The results of D calculations based on the period of the reflected-wave component of h(t) are listed in Table 28 along with the measured Born diameters d*. It can be concluded that the BIA responds to the two peaks in the time-shifted impulse response near the zero of time. Since the deconvolution of y(t) is not perfect (4), the BIA locks in on the "sidelobes" of the R pulse that are T apart. Being based on the Born model (see the middle diagrams in Figure 7), the algorithm expects two pulses of comparable amplitude that are placed symmetrically about the zero of time.

The success of the BIP depends on the three factors listed below:

(1)   Reliability of the phase- and amplitude-comparison techniques to classify the flaw as strong or weak

(2)   Accuracy of the SST in estimating the Born frequency F

(3)   Availability of at least one transducer whose effective center frequency is close to F

Table 28

COMPARISON OF MEASURED AND CALCULATED BORN DIAMETERS
FOR AN 800-m DAIMETER VOID

Figure Reference	Reflected Wave		Born Diameter, m	
	f_r, MHz	T, ns	D (calculated)	d* (measured)
14	6.8	145	280	290
15	4.3	230	450	490
16	3.0	335	650	650
17	2.6	385	750	790

Born diameters were obtained with acceptable inaccuracy only when all of these conditions were met. The main difficulty with the low-frequency (ka~0.5) backscattering measurements is that flaws in materials exhibiting significant grain scattering can be easily missed. Four of the smallest sapphire inclusions in the IN100 test specimens were not found at all. The BIP completely broke down for 22 of the IN100 flaws because these flaws were not detectable by more than one transducer. The coincidence rule was violated for most of these flaws.

The Rockwell Born diameter estimates are generally higher than the Ames estimates (see Table 6). This is attributed mainly to the difference in the adapted ZOTA. The "proper" frequency for the standard flaw (800-μm diameter void) is calculated by Equation (1) to be 2.8 MHz (see Figure 17 for the Ames BIP results obtained with a 2.5-MHz transducer). Nevertheless, the Rockwell BIP produced a size estimate of 760 μm for this flaw with a 4.3-MHz "optimum" transducer by resorting to an empirical ZOTA (see Figure 19). The τ parameter was adjusted until the flatness of the characteristic function $J(r)$ was maximum at r=0. The effect was an increase in the Born diameter from d_0 = 510 μm to D = 760 μm.* It was this "success" of the BIP that prompted us to consider testing yet another ZOTA (30). This ZOTA is based on the Born model and it simply requires the time shift τ to be $\sigma_e/2$. The Born diameters obtained for five representative inclusions using the "correct" (Born) τ are compared with those obtained with the Ames BIP in Table 29. It is concluded that neither ZOTA is capable of assuring the reproducibility of Born diameters obtained for the same flaw with different transducers. The influence of the transducer center frequency on the Born diameters, exhibited in Figure 33, is much stronger and more predictable than that of τ.

Table 29

DEPENDENCE OF BORN DIAMETER ESTIMATES ON METHOD
FOR LOCATING THE FLAW CENTER

Flaw ID No.	Flaw Type	Born Diameter, μm		Nominal Diam., μm
		Ames τ	Born τ (= $\sigma_e/2$)	
11	WC	310	310	900
13	WC	380	730	1,210
15	WC	300	290	480
36	Sapphire	340	700	990
37	Sapphire	250	700	410

---

*Note, however, that when the transducer was "proper," the same empirical procedures for locating the flaw center increased the Born diameter from d_0 = 800 μm (the right answer) to D = 1,250 μm (see Figure 21).

7.3   Satellite-Pulse Observation Technique

The time-domain formalism is rich in insights to the flaw-ultrasound interaction and permits simple solutions to the inverse scattering problem (4). The flaw's response to short bursts of high-frequency insonification can be examined in conjunction with a physical model directly on the instrument screen (SPOT) or analyzed by a semiautomated pattern recognition algorithm (see Subsection 7.4 for SSAP).

Three physical models were developed to aid the ultrasonic examiner in the recognition and real-time interpretation of the satellite pulses (both internal and external) obtained for the voids, WC inclusions, and sapphire inclusions in the test specimens with high-frequency LW and SW transducers. The transducer center frequency per se is immaterial so long as its transient response is short enough to permit resolution of the ESP.

The SPOT was supplemented by the phase-comparison technique in the flaw identification task. The polarities of the associated R and S pulses for the three flaw types were as expected, i.e., the reflected pulse was either positive or negative, the internal satellite was always positive, and the ESP was always negative.* These polarity rules were of immense value in both flaw identification and sizing.

All flaws were "strong" enough to support externally scattered waves. This result was not expected. External satellite pulses were observed in all but one experimental situation (shear waves incident on WC inclusions). Since the separation of the ESP from the R pulse is independent from flaw composition, the inverse scattering formulas involving τ_e [i.e., Equations (7) and (8)] are applicable to all types of flaws with smooth boundaries.

Physical models were also developed for the production of bondplane echoes from the IN100 specimens so that these irrelevant indications could be promptly discounted in search of the often weak satellites of the R pulse (satellite-pulse hunt).

The SPOT diameters listed in Tables 18 and 19 for the ten voids and five WC inclusions represent the averages of many measurements (over 50 in most cases) performed with a multitude of transducers (shear vs. longitudinal, medium vs. high frequency, immersion vs. contact, and low vs. high beam). In addition, each flaw was viewed with the same transducer from many directions. The LW and SW τ measurements were treated on an equal footing. The shear waves were more effective in producing S_e pulses from voids, and the longitudinal waves produced stronger S_i pulses from WC inclusions. This multiprobe-and-multipulse approach has proven to be a good substitute for deconvolution, since we capitalized on the independence of τ measurements from transducer characteristics (including probe

---

*There were four exceptions out of the 42 cases to the last polarity rule.

position). The measurements were repeated in different sequence to assure reproducibility of the results.

The procedure qualification tests included one situation in which the intended flaw (void 08) was in the "shadow zone" of an unintentional, yet unidentified reflector. The SW measurements were most helpful in isolating and subsequently sizing this flaw.

The SPOT size estimates shown in Figure 34 for the 10 voids and the 26 detectable inclusions in the diffusion-bonded test specimens are seen to be in good agreement with the flaw dimensions as reported by the specimen manufacturer. The correlation of the SPOT estimates with the nominal flaw sizes is significant (correlation coefficient 0.97). For this reason, the metallographic sectioning of any of these flaws was waived. Future flaw characterization module development programs will benefit from the availability of these (now standard) specimens. The sizing errors for the 36 test flaws were such that merely 100 ..m (4 mils) need to be added to the SPOT estimate in order to be almost certain that the actual flaw size does not exceed this conservative estimate.

Three randomly selected real flaws (41, 42, and 44) were metallographically sectioned to determine how well the SPOT and the SSAP performed in a "real" test.* Real flaws are complex in shape and disagreements between actual and estimated dimensions were expected. The scanning electron microscope (SEM) photographs of the sectioned flaws are shown in Figure 35. Hand grinding was done in the YZ plane. In each case, the largest flaw dimension was in the X direction. The aluminum-rich flaw 42 was the closest to being spherical. The magnesium-rich flaw 41 was needle-like. Flaw 44 (a void) was almost two-dimensional (planar).

Figures C-14 and C-15 contain the LW and SW signatures, respectively, for the sectioned flaws. The through-wall (depth) and length dimensions cannot be ascertained from the backscattered waveforms. It was expected, however, that the interpretation of extra pulses in $y(t)$ will be similar to that described in Subsection 2.7 and that in many cases the real flaws can be approximated by regularly shaped flaws.

The SPOT and SSAP size estimates listed in Table 30 appear to be conservative for flaw 42 and bracketed by the largest two dimensions of flaws 41 and 44. All real flaws were assumed to be strong spherical scatterers. These results are good considering that these flaws were neither spherical nor homogeneous. It remains to be seen whether the other three real flaws are also irregular and inhomogeneous.

7.4   Semiautomated Satellite Analysis Procedures

It was not until well into the program, when the size estimates obtained by the primary and additional flaw characterization procedures for the first ten test flaws were compared to their nominal dimensions,

---

*Flaws 43, 45, and 46 were held for further measurements.

Figure 34.   Correlation of Nominal Flaw Sizes With Estimates Obtained
by the Satellite-Pulse Observation Technique (SPOT)
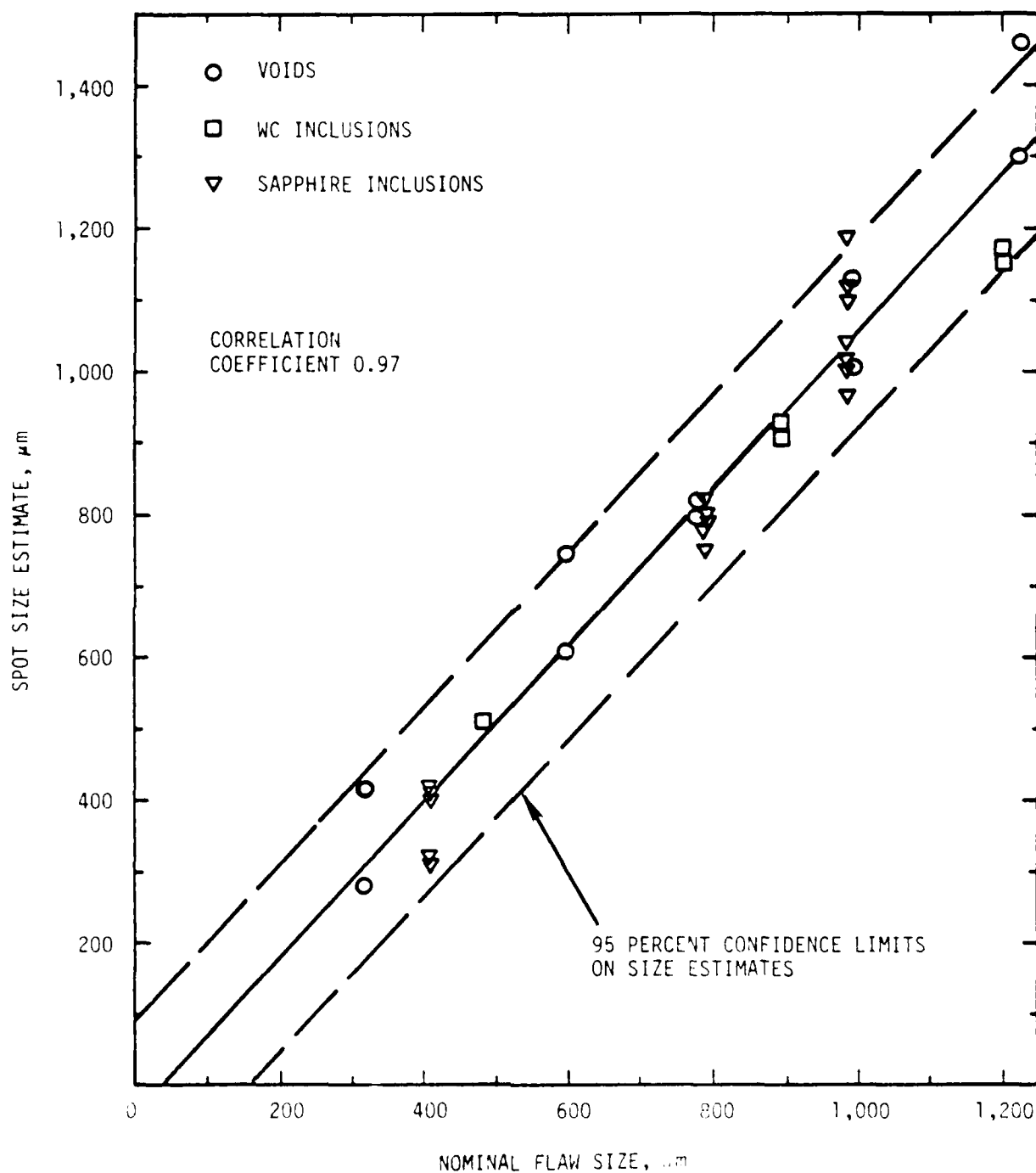
500X

FLAW 41

140 x 610 x 100 ⊔m

YXZ

Z

Y
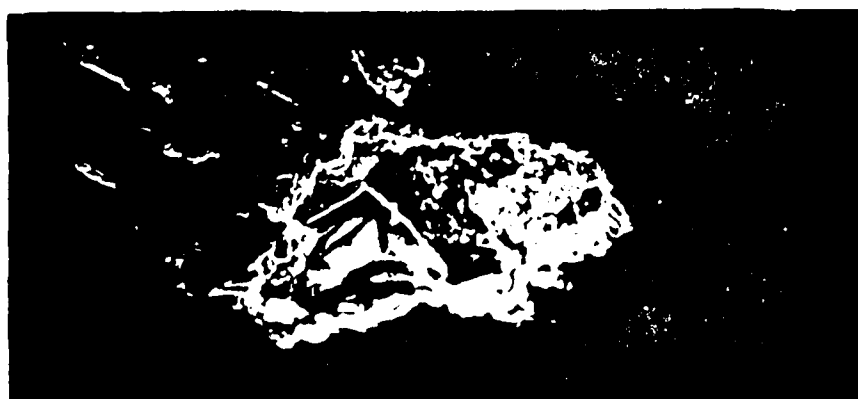
500X

FLAW 42

150 x 230 x 150 ⊔m

YXZ
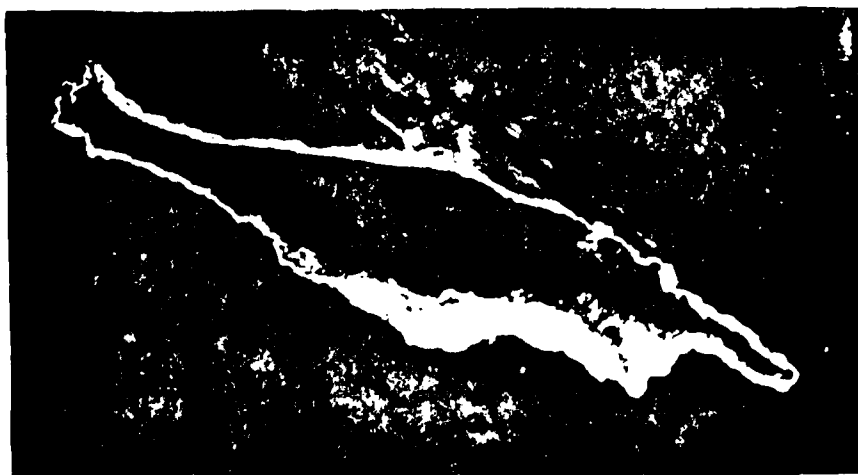
400X

FLAW 44

370 x 500 x 90 ⊔m

YXZ

Figure 5c. Scanning Electron Microscopy (SEM) Photographs of Three Real Flaws

Table 30

COMPARISON OF ACTUAL AND ESTIMATED SPOT AND SSAP
DIMENSIONS OBTAINED FOR THREE REAL FLAWS

Flaw	Equivalent Diameter, μm		Largest Two	Flaw
ID No.	SPOT	SSAP	Dimensions, μm	Composition
41	380, 410	230, 450	140, 610	Magnesium
42	380, 390	220, 430	150, 230	Aluminum
44	390, 440	260, 520	370, 500	Void

that attempts were made to automate or systematize the qualified SPOT procedures to the extent possible in order to assure reproducibility and reliability. The remaining 32 test flaws were, therefore, used not only to further test the applicability of the SST, BIT, and SPOT to inclusions but also to quantify the performance degradation associated with the elimination of the SST and/or SPOT examiner from the inspection loop.

The SSAP size estimates shown in Figure 36 for the five WC inclusions and the 21 detectable sapphire inclusions are seen to be less accurate--by 40 percent to be exact--than those obtained directly from the instrument screen by a trained examiner (see Figure 34). The correlation of the SSAP estimates with the nominal flaw sizes remains significant (correlation coefficient 0.94). The sizing errors for the 26 inclusions were such that merely 140 μm (5.5 mils) need to be added to the SSAP estimate in order to be almost sure that the actual flaw size does not exceed this conservative estimate. Sizing errors of this magnitude are acceptable for an automated flaw characterization module. The performance of the SSAP was degraded relative to that of the SPOT mainly because the SSAP cannot differentiate against the spurious echoes from the bondplanes in the IN100 specimens and only longitudinal waves were used to interrogate the sapphire inclusions.

Of course, bondplane indications were not a problem for the SSAP in the analysis of the profiles obtained for the six real flaws (see Figure D-7). The SSAP size estimates obtained for these flaws are included in Table 30. As expected, deconvolution with the front-surface echo produced estimates that were more precise (smaller) than the SPOT estimates.
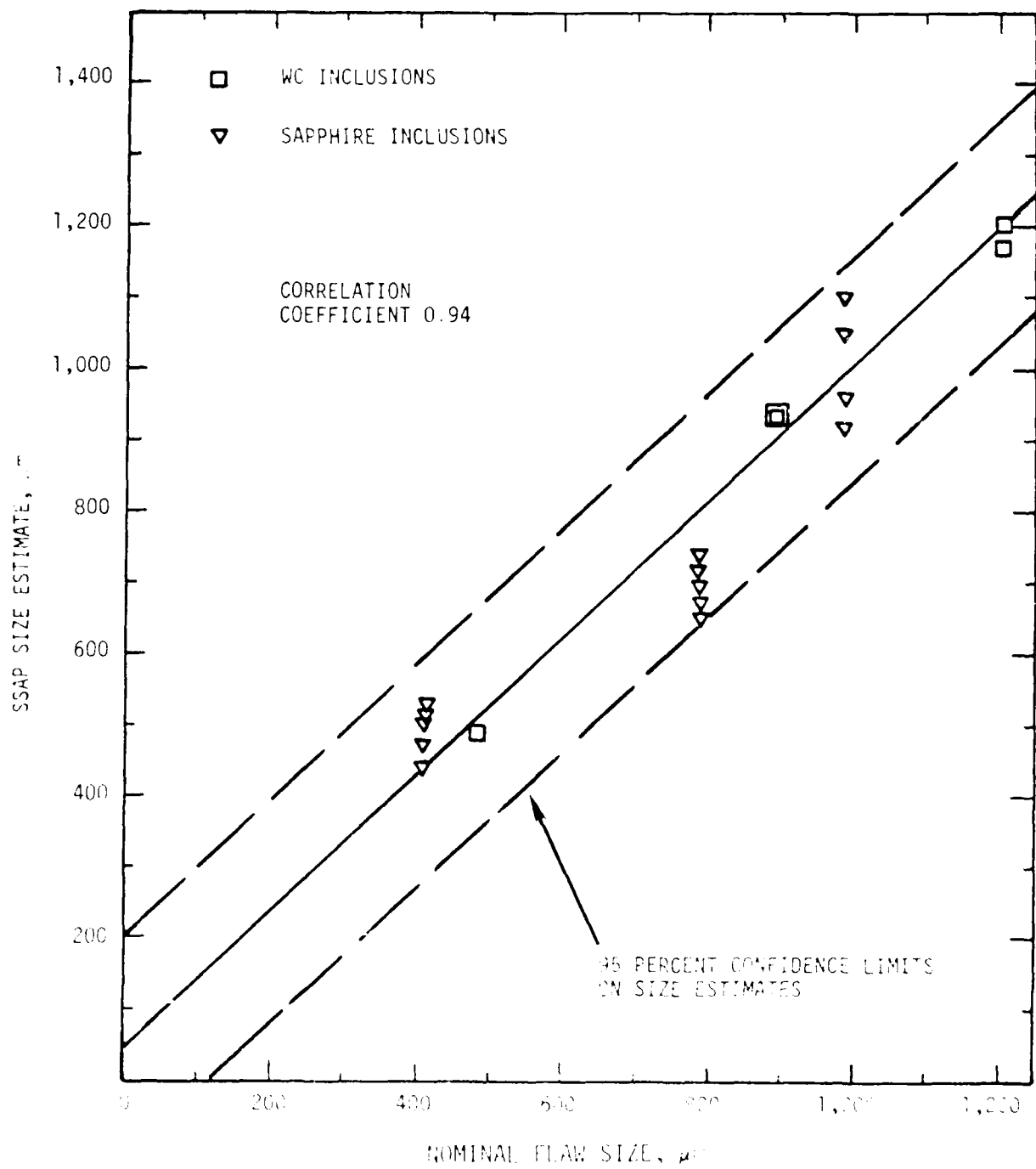
Figure 36. Correlation of Nominal Flaw Sizes With Estimates Obtained
by the Semiautomated Satellite Analysis Procedures (SSAP)

END

1.0

45
50

2.8

2.5

3.2

2.2

3.6

1.1

40

2.0

1.8

1.25

1.4

1.6
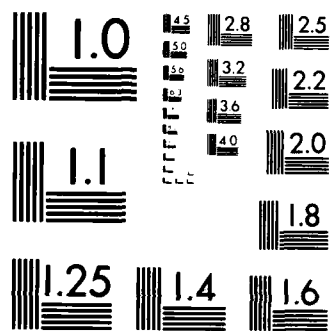
MICROCOPY RESOLUTION TEST CHART

NATIONAL BUREAU OF STANDARDS

8. CONCLUSIONS

The main program objective was to evaluate the supplemented BIT (Born inversion technique) in the forms developed at the Ames Laboratory and the Rockwell Science Center against 40 or more internal bulk flaws in titanium and IN100 alloys under simulated field (blind-test) conditions. Due to its sole reliance on the front-surface echo (R pulse), the BIP (Born inversion procedures) yield essentially the same result for voids and inclusions when the same transducer is used. The Born diameter estimates (D) were determined to be independent of not only flaw composition, but also shape, size, and orientation. Instead, the size estimates were determined to be directly related to the period of the incident ultrasonic wave (T). Each transducer yields a different Born diameter according to the relationship $D = 1.95T$, where D is in micrometers and T is in nanoseconds.

The BIA (Born inversion algorithm) expects two pulses of comparable amplitude from the flaw which is assumed to be a weak scatterer (Born flaw). The algorithm correctly treats the first half-cycle of the impulse response of a real flaw as the front-surface echo, but mistakes its third half-cycle for a back-surface echo (S_i in Figure C-5) or a creeping-wave return (S_e in Figure C-1). Thus, short-period reflected pulses give rise to small Born diameters and long-period reflected pulses yield large size estimates. For this reason, the BIP results could not be reproduced with different transducers. Unless there was a transducer available for transmitting ultrasonic waves with a period equal to the separation σ_e between the associated reflected and externally scattered pulses (coincidence rule, $T = \sigma_e$), the Born diameter was unreliable. This means that of the transducers used to obtain the ten flaw waveforms shown in Figures C-1 and C-5, only the transducer used on flaw 01 was "proper" for acquiring the Born inversion data. For the other nine flaws, the effective transducer center frequency had to be lowered by at least 50 percent in order to obtain reliable Born diameters.

Presorting of the three standard-frequency transducers for acquiring the Born inversion data was done by applying the qualitative SST (spectrum splicing technique) to the deconvolved flaw spectra obtained with the available transducers. A transducer whose bandwidth encompassed more than one of the flaw's resonance peaks was ruled inappropriate for acquiring Born inversion data. Efficient appropriate transducers were available for 24 of the 36 flaws that were detected in the diffusion-bonded test specimens.* The correlation of the resulting Born diameters with the nominal flaw dimensions was barely significant (correlation coefficient 0.81). The size estimates were accurate only to within 370 μm (see Figure 32). One certain way to improve the reliability and accuracy of the Born size estimates is to include non-standard as well as standard frequency transducers in the measurement protocol. This is not practical.

---

*The BIP broke down completely for the 12 sapphire inclusions that could not be detected with the required low-frequency transducers.

The sensitivities/insensitivities of and the frequencies preferred by the five techniques incorporated into the primary and additional flaw characterization procedures are summarized in Table 31. The amplitude- and phase-comparison techniques were used to classify the flaw as either strong or weak. The SST used this information in determining the most appropriate transducer(s) for acquiring the Born inversion data for a given flaw. The BIP and the SPOT (satellite-pulse observation technique) use different information to obtain the size estimate. There is a great deal of flaw information thrown away by the BIP. By the time the effective transducer center frequency is lowered so that $T = \sigma_e$, the ESP (external satellite pulse) can no longer be distinguished from the ringdown of the R pulse. In contrast to the BIP, the SPOT is sensitive to Z (acoustical impedance of flaw) and d, but insensitive to T as long as the frequency of the incident wave is high ($f_r > 4$ MHz). It is concluded that multiple measurements made with waves of different mode, period, and incidence angle and no less than three physical models for ultrasound-flaw interactions (one for voids and the other two for weakly and strongly scattering inclusions) are necessary to solve the inverse problem for flaw type and size in an unambiguous manner.

Table 31

COMPARISON OF THE FIVE ULTRASONIC TECHNIQUES APPLIED
TO THE TEST FLAWS

Technique	Sensitive To	Insensitive To	Preferred Frequency Range
Amplitude comparison (qualitative)	d[1], Z[2]	T[3]	N.A.[4]
Phase comparison (qualitative)	Z	d, T	N.A.
Spectrum splicing (qualitative)	d, Z	T	Low to high
Born inversion (quantitative)	T	Z, d	Born frequency
Satellite pulse (quantitative)	Z, d	T	Medium to high

[1] Flaw diameter
[2] Acoustical impedance of flaw
[3] Wave period
[4] Not applicable

Only high-fidelity transducers that emphasized the important physical variables involved in the flaw-ultrasound interaction process were included in the SPOT measurement protocol. Space-time-frequency analyses of the information obtained "on the spot" about the flaw over the 4 to 8 MHz frequency range resulted in a significantly better characterization of the test flaws than has been possible with the BIP. All of the 42 detected flaws were sized by noting the separation of the ESP from the specularly reflected pulse. Internal satellite pulses in the case of the five WC inclusions provided confirmatory size estimates. The six real flaws were too small for determination of their shape and orientation. The size estimates for these flaws were conservative. The sizing errors for the 36 flaws in the diffusion-bonded specimens were such that merely 100 μm need to be added to the SPOT estimate in order to be almost sure that the actual flaw is not larger than this conservative size estimate.

The satellite pulses can be best enhanced by the deconvolution process if the front-surface echo [i.e., the first three half-cycles in $y(t)$] is used as the reference waveform. Unlike the results of doublet-separation (σ) measurements, the results of resonance-peak-separation (p or P) measurements can be averaged during specimen scanning. Thus, satellite pulses can best be detected by analyzing the spatially averaged magnitude spectra $H(f)$ for the degree and extent of modulation. As long as the R-S_i doublet of inclusion 11 (drawn with a heavy line in the uppermost trace of Figure C-6) does not leave the gate, its magnitude spectrum (see upper right trace in Figure D-1) is time invariant. The essence of SSAP (semiautomated satellite analysis procedures) is that the peak separation P_i can be determined automatically while the accurate assessment of the doublet separation σ_i (= $1/P_i$) requires a judgment by the examiner. It can be concluded that the semiautomated satellite analysis procedures:

- Must be supplemented by techniques to classify the flaw as strong or weak.

- Do not require the examiner to interpret the flaw waveform directly from the instrument screen.

- Yield more precise size estimates than the SPOT.

- Make more complete use of the available flaw information than the Born inversion procedures.

- Are better candidates for automated application than the Born inversion procedures.

REFERENCES

1. Thompson, R. B. and Gray, T. A., "Range of Applicability of Inversion Algorithms," in Review of Progress in Quantitative Nondestructive Evaluation, Volume 1, 233-249, Plenum Press, New York, 1982.

2. Addison, R. C., Ultrasonic Test Bed for Quantitative NDE, Technical Report No. AFWAL-TR-82-4075, Materials Laboratory, Air Force Wright Aeronautical Laboratories, Wright-Patterson Air Force Base, Ohio, July 1982.

3. Lee, D. A., "Ill-Posed and Well-Posed Problems in Inverse Elastodynamic Scattering for Nondestructive Evaluation," Journal of Nondestructive Evaluation, Volume 2, Nos. 3-4, 161-172, 1981.

4. Lee, D. A., Moran, T. J., and Crane, R. L., "Practical Considerations for Estimating Flaw Sizes From Ultrasonic Data," Materials Evaluation, Volume 42, No. 8, 1150-1158, 1984.

5. Tittmann, B. R. and Cohon, E. R., "Analysis of Ultrasonic Wave Scattering for Characterization of Defects in Solids: I. Spherical Inclusions and Reciprocity," Journal of Nondestructive Evaluation, Volume 3, No. 3, 175-192, 1982.

6. Cohen-Tenoudji, F., Tittmann, B. R., Ahlberg, L. A., and Quentin, G., "Experimental Measurements of Scattering From Bulk Flaws," in Review of Progress in Quantitative Nondestructive Evaluation, Volume I, 173-179, Plenum Press, New York, 1982.

7. Gruber, G. J., Hendrix, G. J., and Mueller, T. A., "Development of a Quantitative Flaw Characterization Module - A Status Report," in Review of Progress in Quantitative Nondestructive Evaluation, Volume 3A, 309-321, Plenum Press, New York, 1984.

8. Ahlberg, L. A., Elsley, R. K., Graham, L. J., and Richardson, J. M., "Long Wavelength Ultrasonic Characterization of Inclusions in Silicon Nitride," in Proceedings of the Review of Progress in Quantitative Nondestructive Evaluation, Report No. AFWAL-TR-80-4078, 656-662, July 1980.

9. Kwun, H., Singh, G. P., Fujisawa, K., Froes, F. H., and Eylon, D., "Feasibility of Inclusion Detection and Characterization in Titanium Powder Compacts Using Ultrasonics," NDT International, Volume 17, No. 2, 73-79, April 1984.

10. Cohen-Tenoudji, F., Ahlberg, L. A., and Tittmann, B. R., "The Role of Creep Rays in the Scattering from Spheroidal Cavities and Inclusions in Solids," in IEEE Ultrasonics Symposium Proceedings, 853-858, 1981.

11. Rose, J. H. and Krumhansl, J. A., "Determination of Flaw Characteristics From Ultrasonic Scattering Data," <u>Journal of Applied Physics</u>, Volume 54, No. 4, 2951-2952, April 1979.

12. Thompson, D. O. and Wormley, S. J., "Long and Intermediate Wavelength Flaw Reconstruction," in <u>Review of Progress in Quantitative Nondestructive Evaluation</u>, Volume 4B, Plenum Press, New York, 1985.

13. Gray, T. A., private communication, March 1982.

14. Franz, W. and Deppermann, K., "Theorie der Beugung am Zylinder unter Berücksichtigung der Kriechwellen," <u>Annalen der Physik, Series 6</u>, Volume 10, 361-373, June 1952.

15. Gruber, G. J., "Defect Identification and Sizing by the Ultrasonic Satellite-Pulse (Observation) Technique," <u>Journal of Nondestructive Evaluation</u>, Volume 1, No. 4, 263-276, 1980.

16. Harbold, M. L. and Steinberg, B. N., "Direct Experimental Verification of Creeping Waves," <u>Journal of the Acoustical Society of America</u>, Volume 45, 592-603, March 1969.

17. Pierce, A. D., <u>Acoustics: An Introduction to Its Physical Principles and Applications</u>, Chapter 9, McGraw-Hill, New York, 1981.

18. Khuri-Yakub, B. T., Kino, G. S, and Murakami, Y., "Ultrasonic Wave Scattering for Defect Characterization Applied to Ceramic Materials," in <u>Proceedings of 38th American Society for Nondestructive Testing Conference</u>, Denver, Colorado, October 1978.

19. Hsu, D. K., Rose, J. H., and Thompson, D. O., "Ultrasonic 3-D Reconstruction in Solids Using the Inverse Born Algorithm," in <u>Review of Progress in Quantitative Nondestructive Evaluation</u>, Volume 2B, 995-1018, Plenum Press, New York, 1983.

20. Chou, C. H., Khuri-Yakub, B. T., and Liang, K., "High-Frequency Bulk Wave Measurements of Structural Ceramics," in <u>Proceedings of Review of Progress in Quantitative Nondestructive Evaluation</u>, Report No. AFWAL-TR-80-4078, 663-670, July 1980.

21. Flax, L. and Überall, H., "Resonant Scattering of Elastic Waves from Spherical Solid Inclusions," <u>Journal of the Acoustical Society of America</u>, Volume 67, No. 5, 1432-1442, May 1980.

22. Bollig, G. and Langenberg, K., "Ultrasonic Defect Classification Using the Singularity Expansion Method," in <u>Review of Progress in Quantitative Nondestructive Evaluation</u>, Volume 1, 203-212, Plenum Press, New York, 1982.

23. Bhagat, P. K., Chimenti, D. E., Moran, T. J., and Shimin, K. D., "Effects of Deconvolution Procedures on Size Estimates in the Born Inversion Algorithm," in Review of Progress in Quantitative Nondestructive Evaluation, Volume 3A, 395-403, Plenum Press, New York, 1984.

24. Marsh, K. A. and Richardson, J. M., "The Automation of the Born Inversion for Ultrasonic Flaw Sizing," in Review of Progress in Quantitative Nondestructive Evaluation, Volume 2B, 975-987, Plenum Press, New York, 1983.

25. Gruber, G. J., "Implementation of Inverse-Scattering Algorithms for Characterizing Voids in Gas Turbine Rotor Discs," in New Procedures in Nondestructive Testing, editor P. Höller, Springer-Verlag Berlin and Heidelberg, 1983.

26. Rose, J. H., Thompson, D. O., and Thompson, R. B., Subcontract Proposal to Southwest Research Institute for a High Reliability Quantitative Flaw Characterization Module, Ames Laboratory, Iowa State University, March 1981.

27. Moran, T. J., private communication, June 1982.

28. Shambaugh, R. L., Quantitative Flaw Characterization Test Specimens, Technical Report No. PWA FR-17354 to Southwest Research Institute, Pratt & Whitney Aircraft Group, West Palm Beach, Florida, January 1983.

29. Moyzis, J. A. and Forney, D. M., "Increased Reliability - A Critical NDE Research Goal," in Review of Progress in Quantitative Nondestructive Evaluation, Volume 1, 7-11, Plenum Press, New York, 1982.

30. Moran, T. J., private communication, July 1984.

APPENDIX A

MAGNITUDE SPECTRA USED IN THE APPLICATION
OF THE SPECTRUM SPLICING TECHNIQUE
TO THE 42 TEST FLAWS
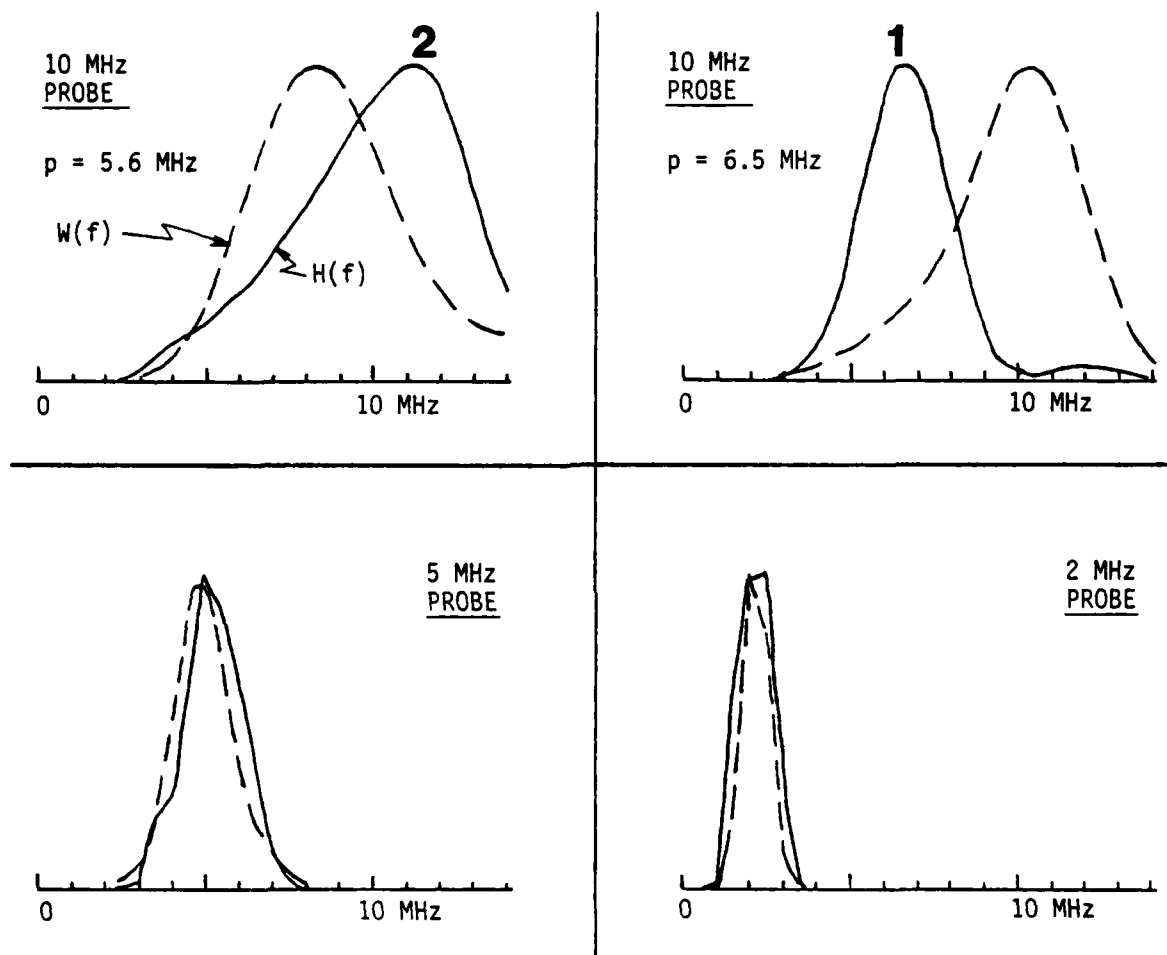
Figure A-1. Magnitude Spectra Obtained for Titanium Void <u>No. 01</u> <u>No. 01</u> with Four Longitudinal-Wave Transducers. $\overline{W(f)}$ = reference spectrum and H(f) = flaw spectrum.
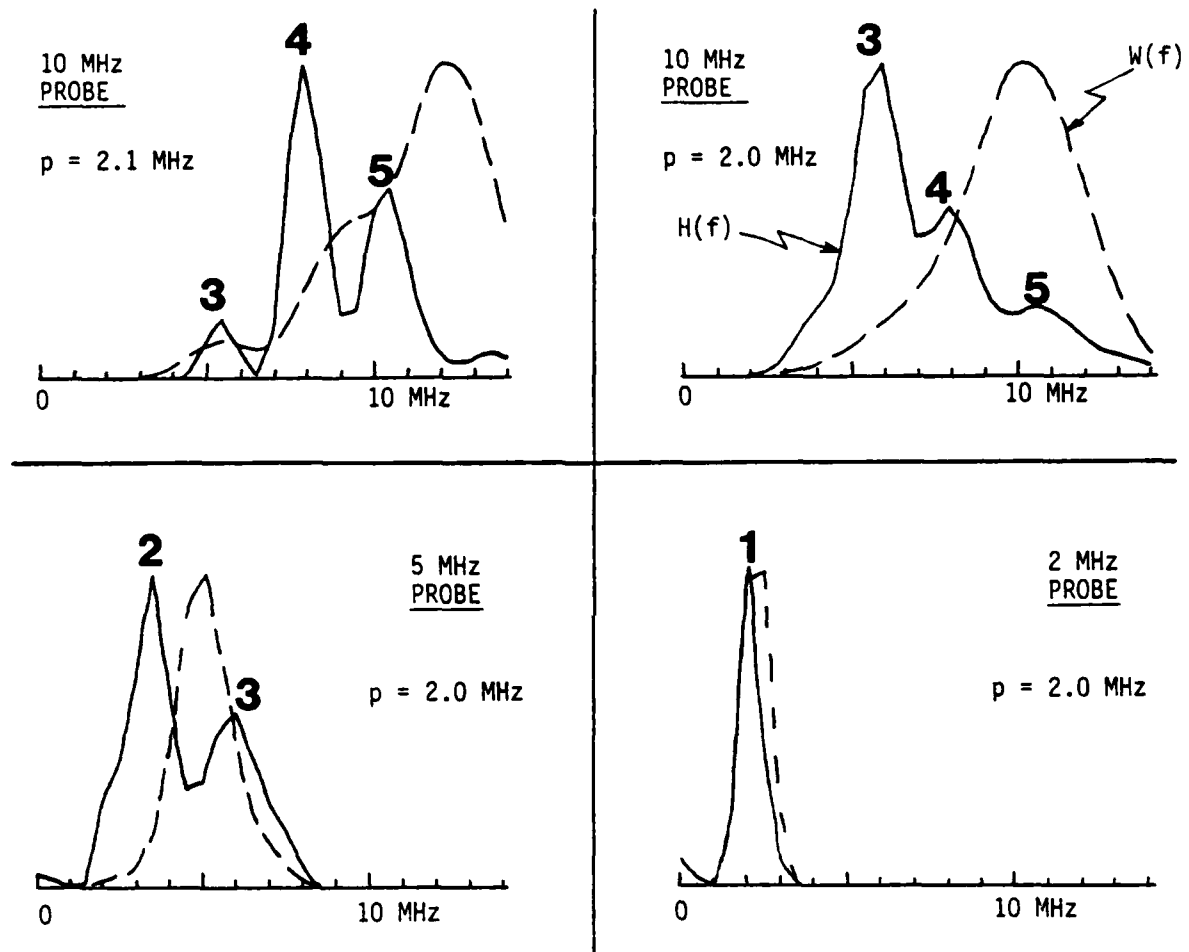
Figure A-2. Magnitude Spectra Obtained for Titanium Void No. 02
with Four Longitudinal-Wave Transducers

A-3
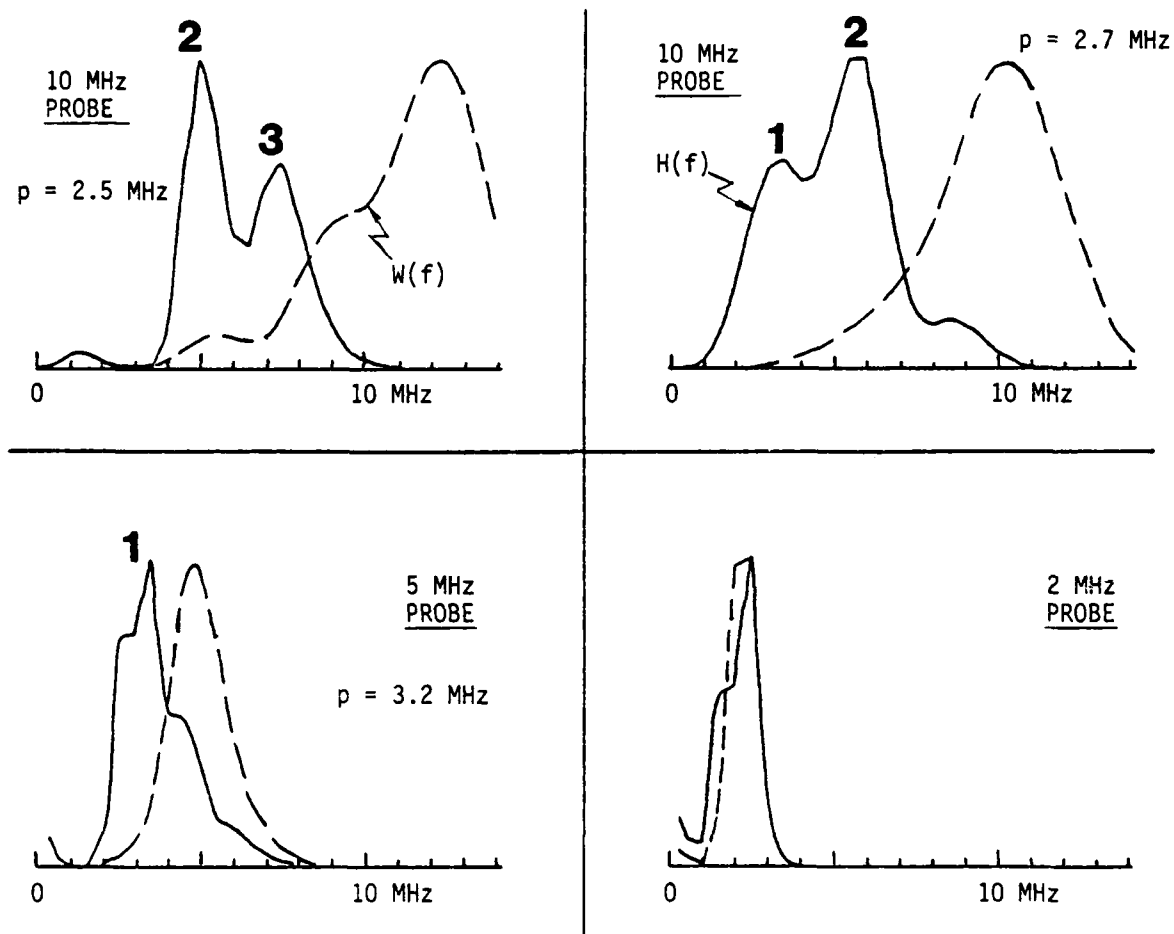
Figure A-3. Magnitude Spectra Obtained for Titanium Void No. 03
with Four Longitudinal-Wave Transducers
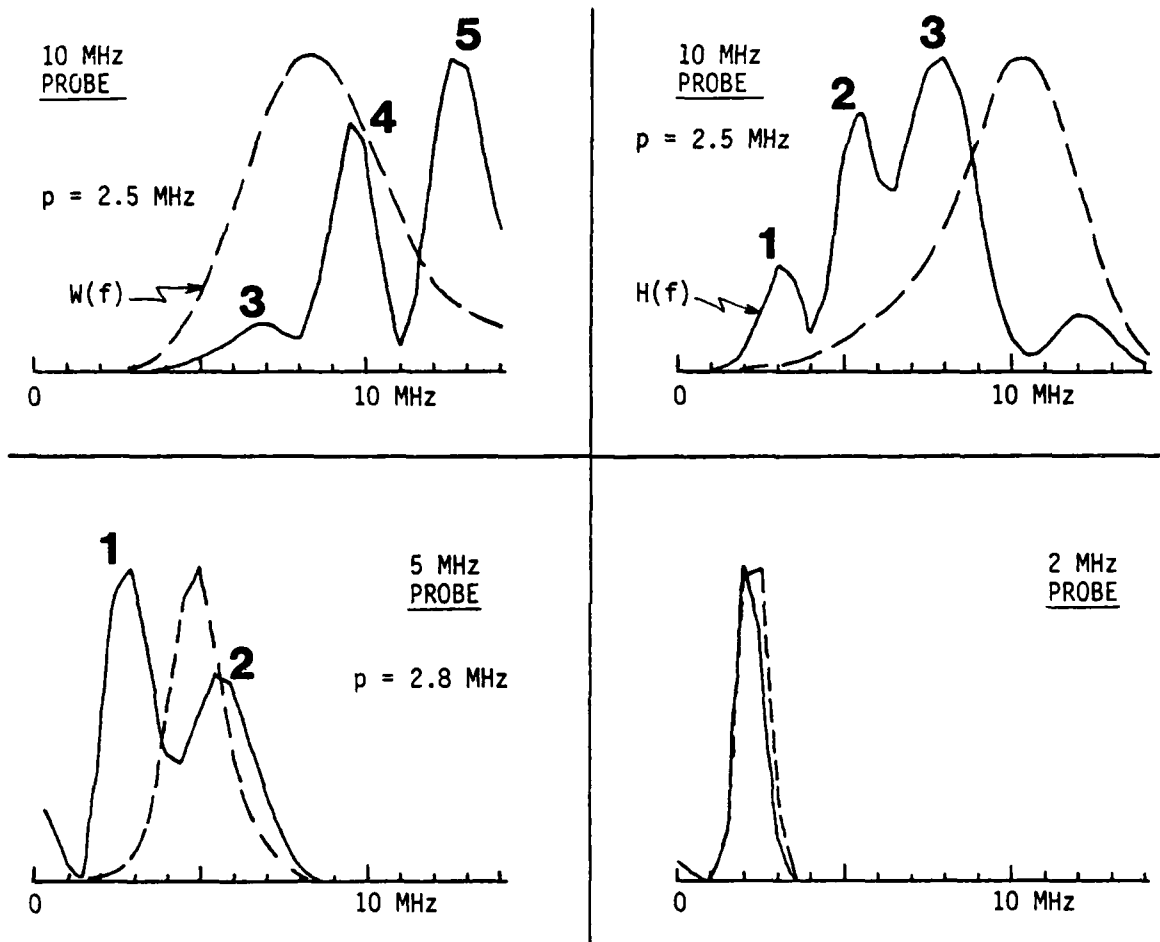
Figure A-4. Magnitude Spectra Obtained for Titanium Void No. 04 with Four Longitudinal-Wave Transducers
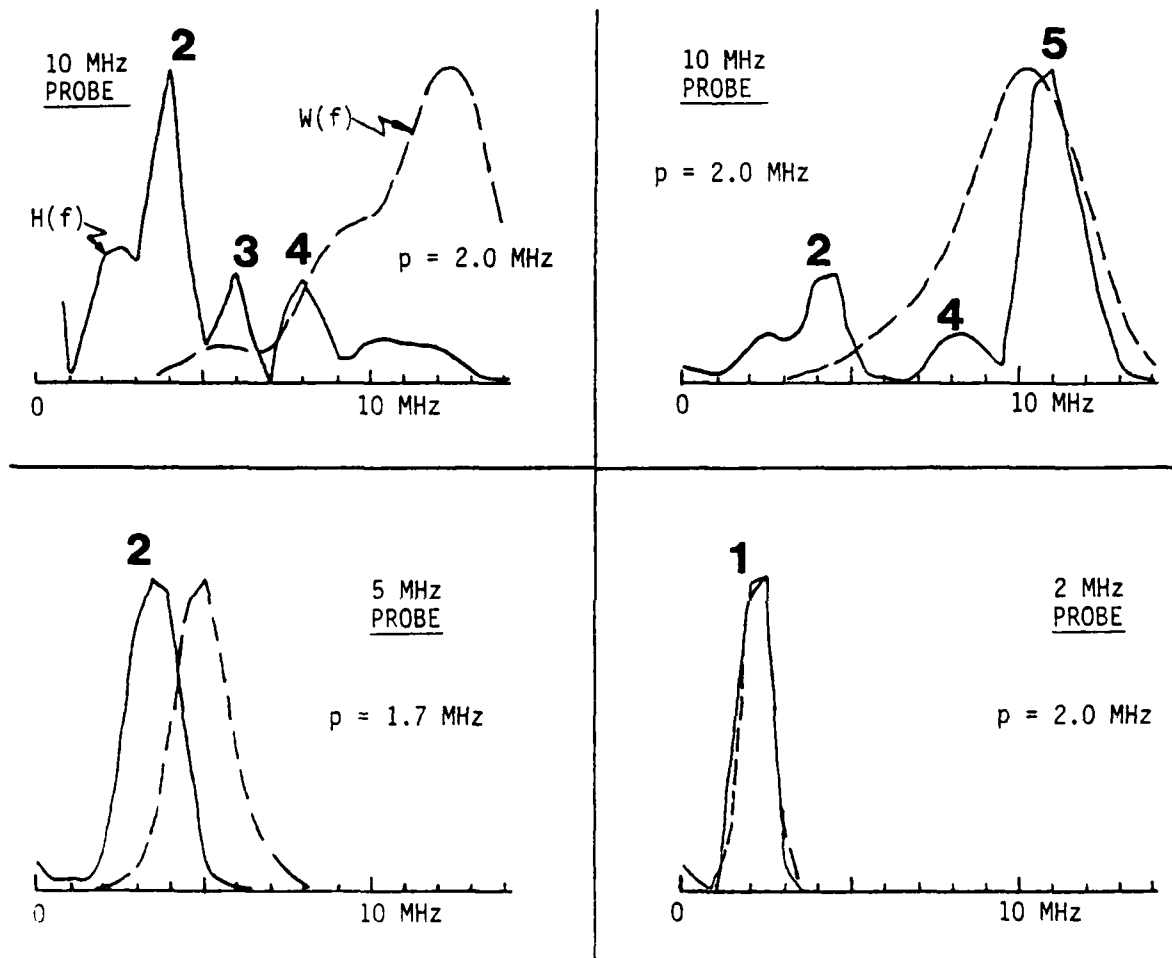
Figure A-5. Magnitude Spectra Obtained for Titanium Void No. 05
with Four Longitudinal-Wave Transducers
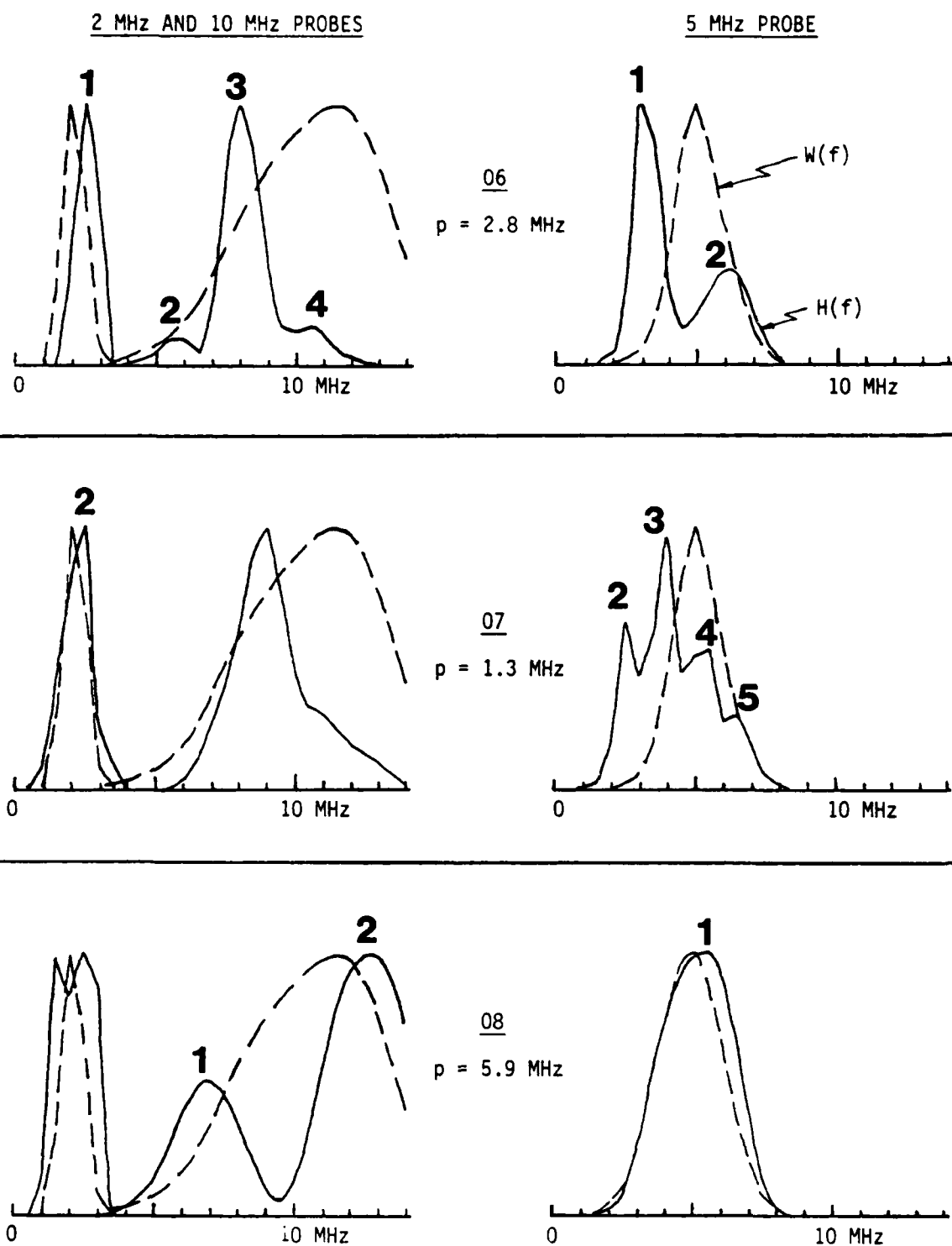
Figure A-6. Magnitude Spectra Obtained for IN100 Voids Nos. 06, 07, and 08 with Three Longitudinal-Wave Transducers

A-7

2 MHz AND 10 MHz PROBES   5 MHz PROBE
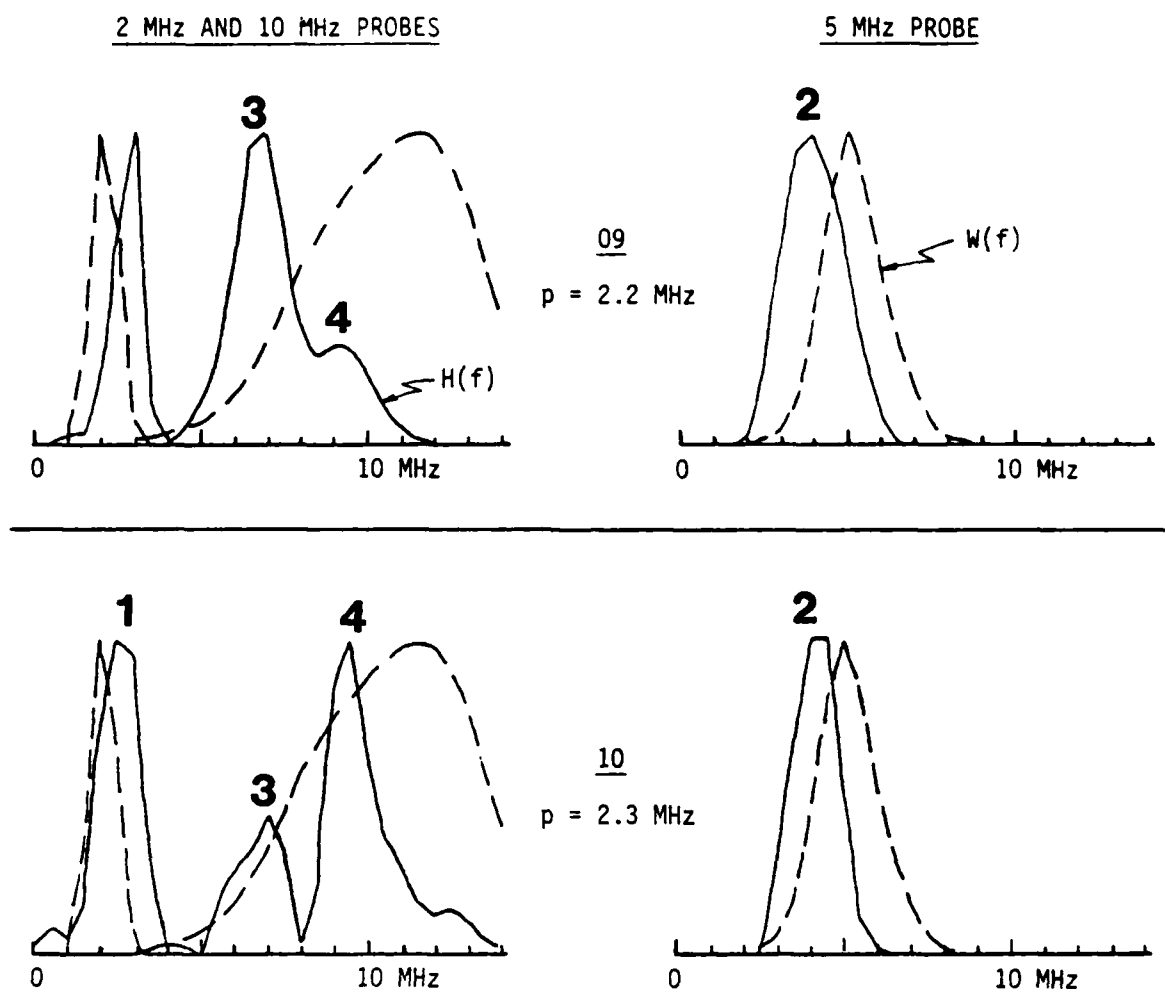
Figure A-7.   Magnitude Spectra Obtained for IN100 Voids Nos. 09
              and 10 with Three Longitudinal-Wave Transducers

A-8
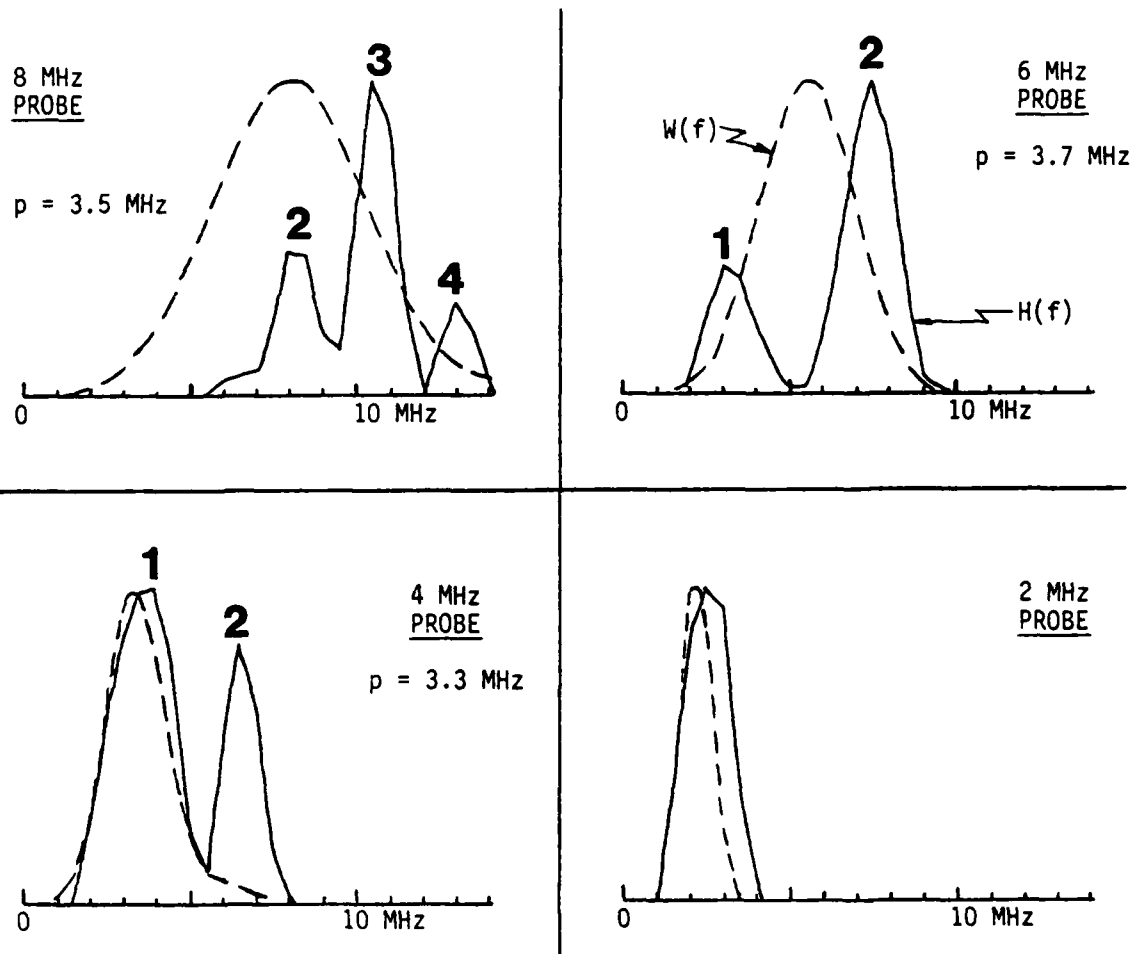
Figure A-8. Magnitude Spectra Obtained for Titanium Inclusion
No. 11 with Four Longitudinal-Wave Transducers
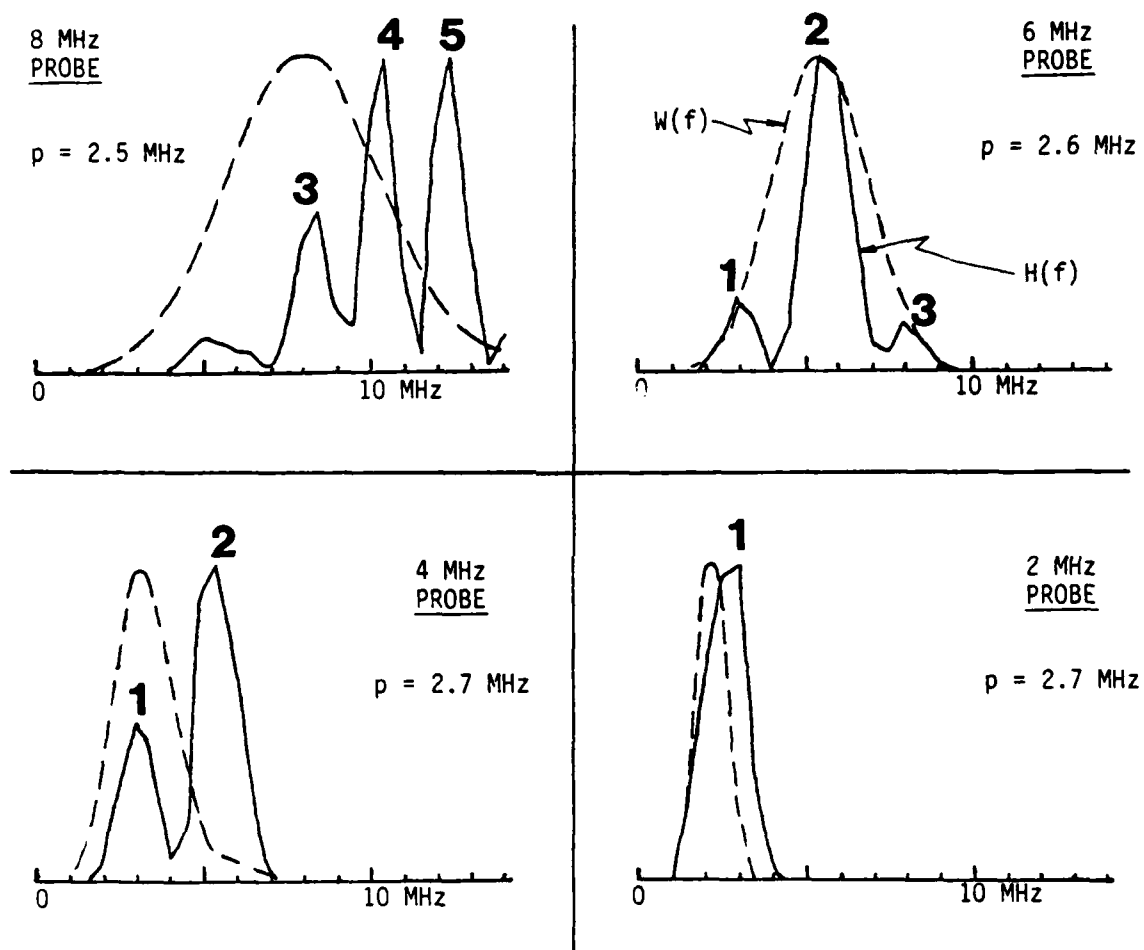
Figure A-9. Magnitude Spectra Obtained for Titanium Inclusion
No. 12 with Four Longitudinal-Wave Transducers

A-10
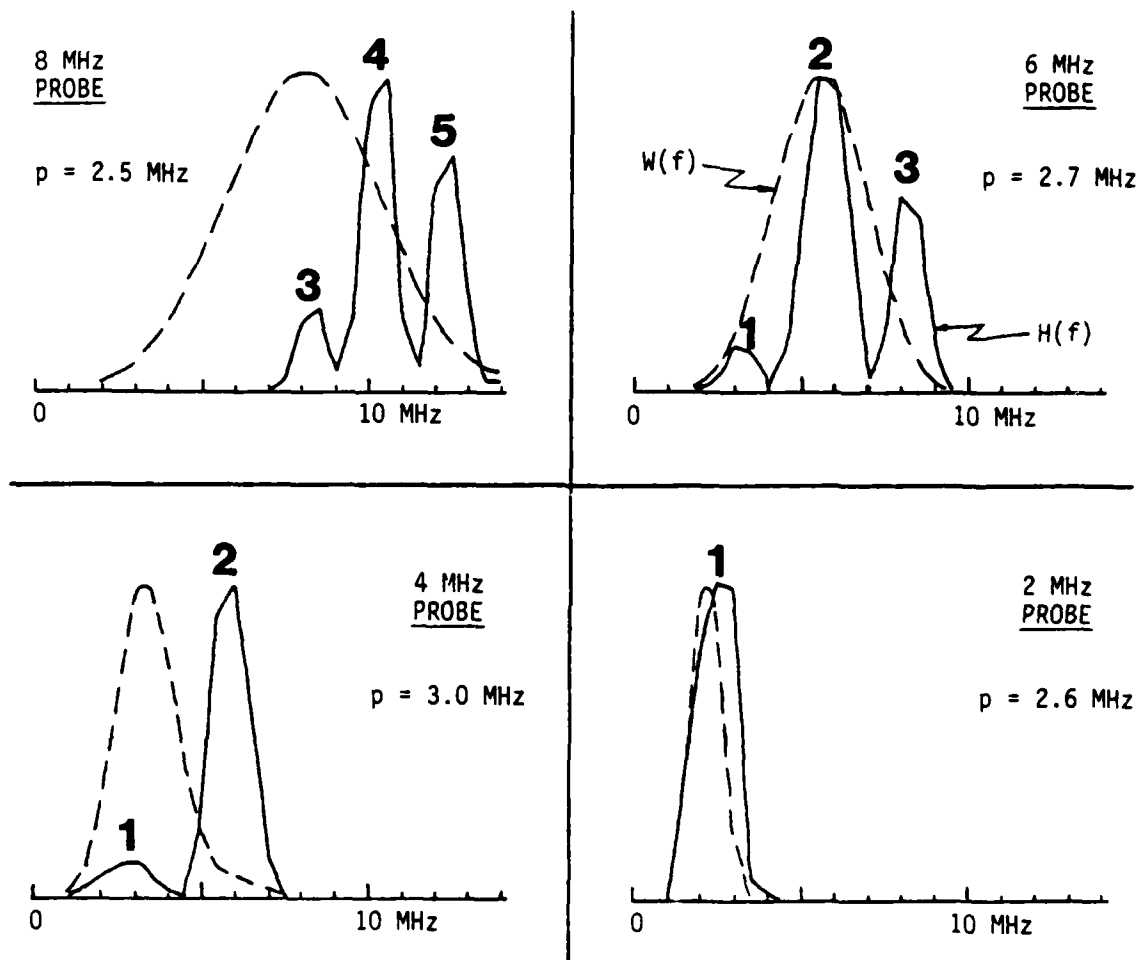
Figure A-10. Magnitude Spectra Obtained for Titanium Inclusion
No. 13 with Four Longitudinal-Wave Transducers
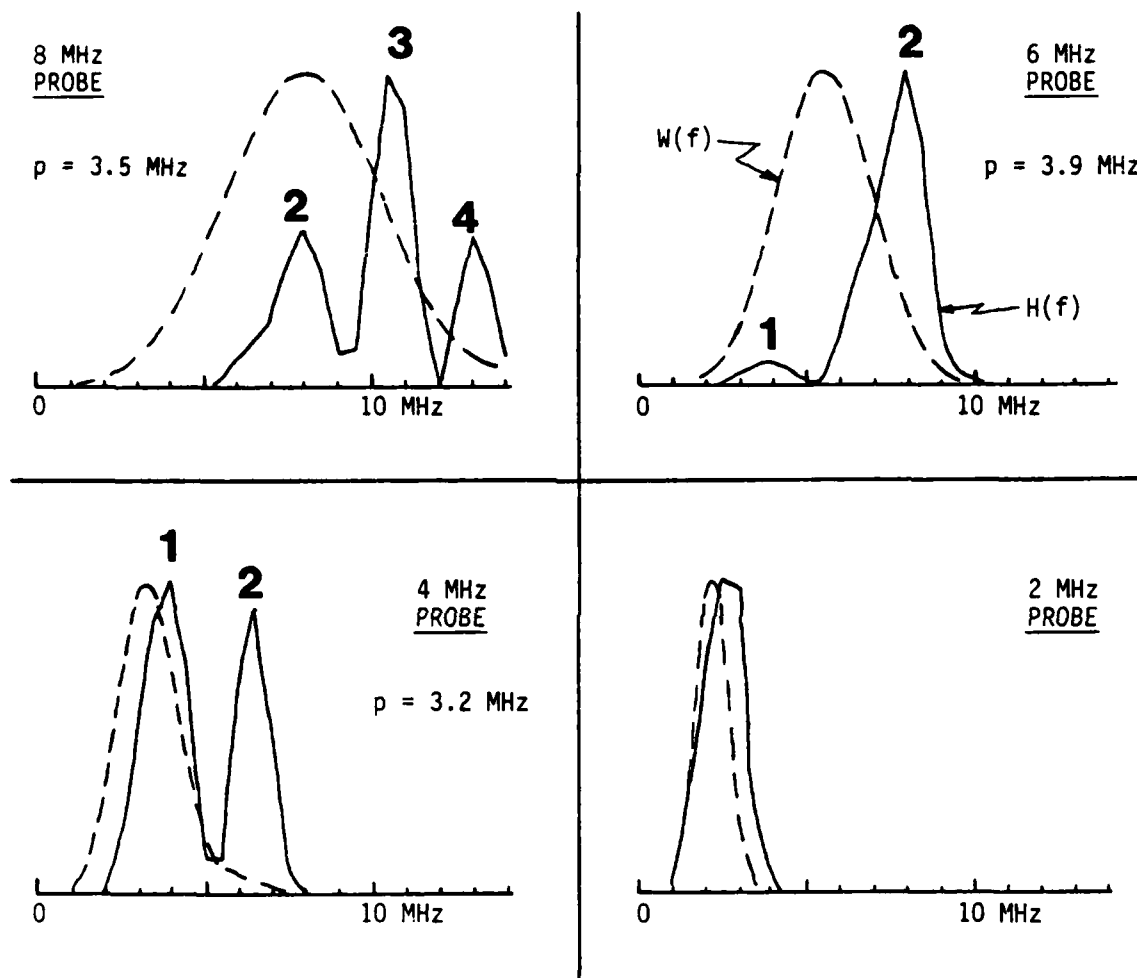
Figure A-11. Magnitude Spectra Obtained for Titanium Inclusion
No. 14 with Four Longitudinal-Wave Transducers
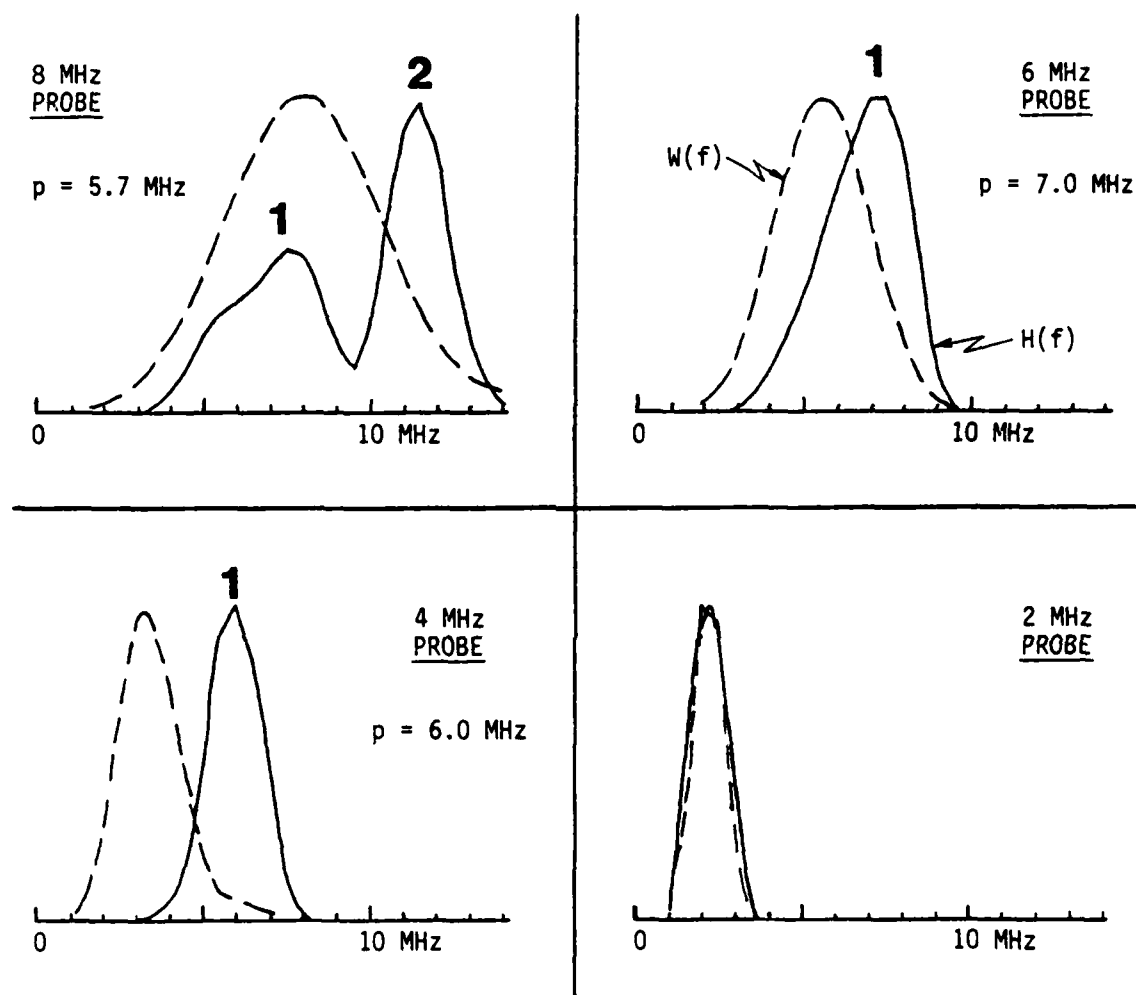
Figure A-12.   Magnitude Spectra Obtained for Titanium Inclusion
No. 15 with Four Longitudinal-Wave Transducers

A-13
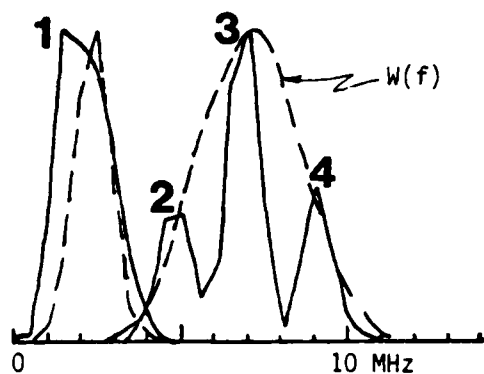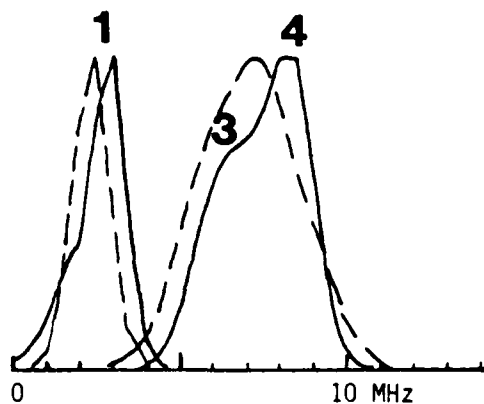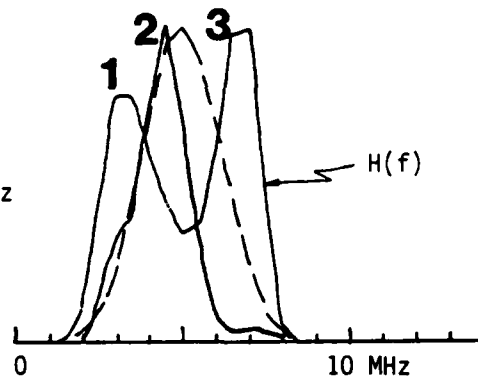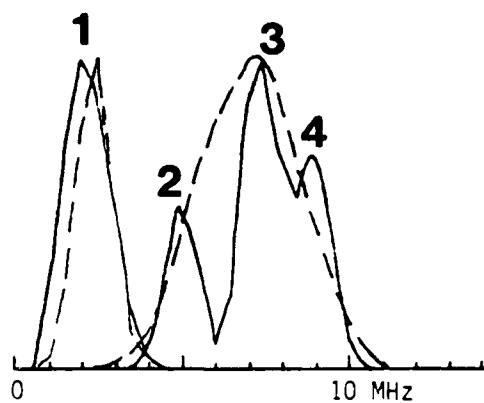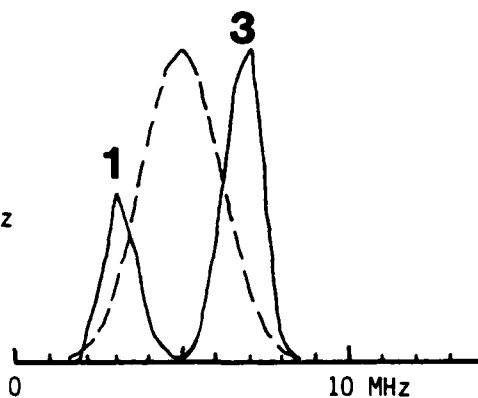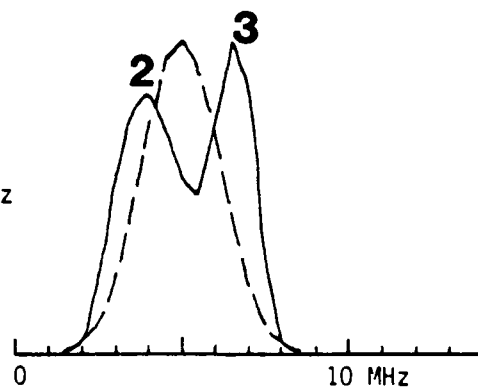
Figure A-13. Magnitude Spectra Obtained for IN100 Inclusions Nos. 22, 23, and 24 with Three Longitudinal-Wave Transducers
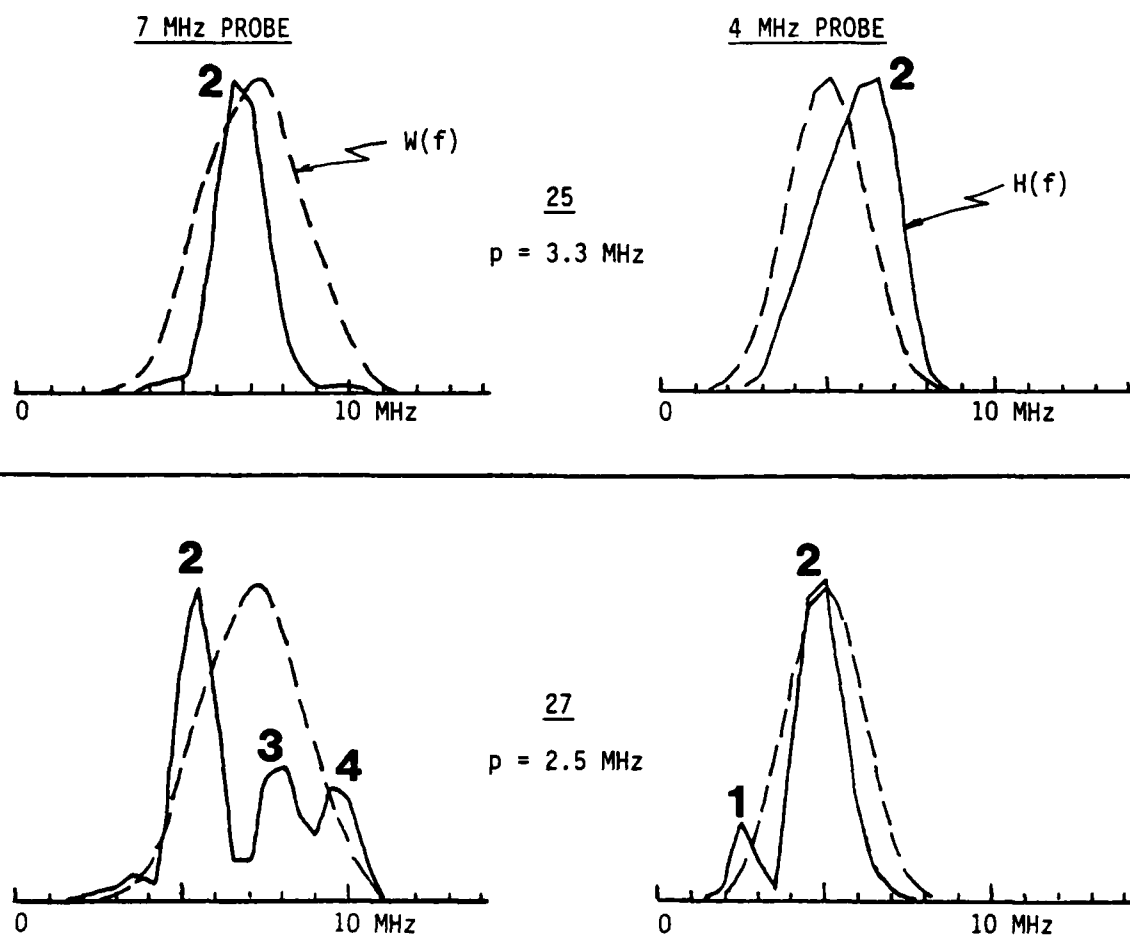
Figure A-14. Magnitude Spectra Obtained for IN100 Inclusions Nos. 25 and 27 with Three Longitudinal-Wave Transducers
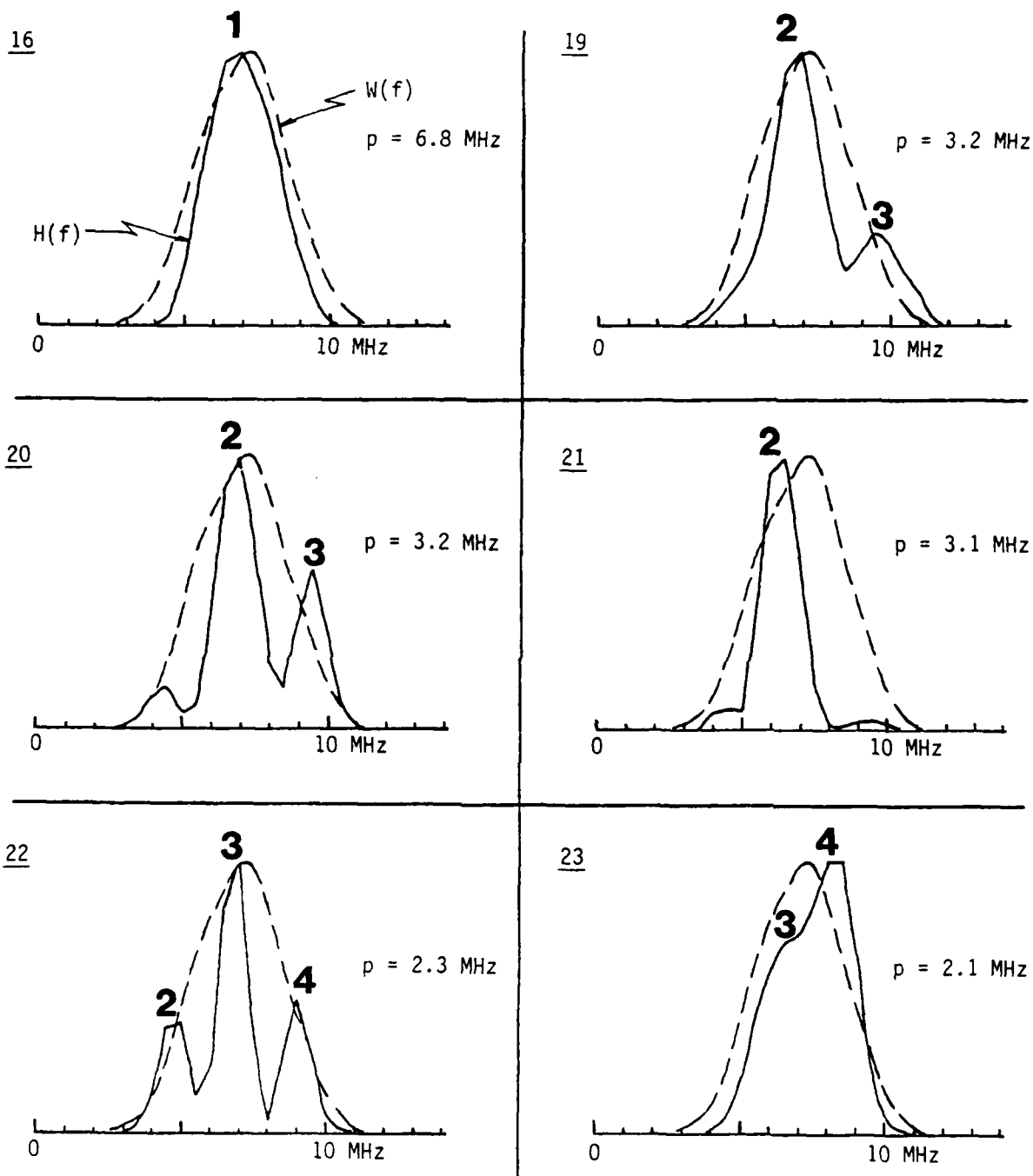
Figure A-15. Magnitude Spectra Obtained for IN100 Inclusions
Nos. 16, 19, 20, 21, 22, and 23 with a 7 MHz
Longitudinal-Wave Transducer

A-16
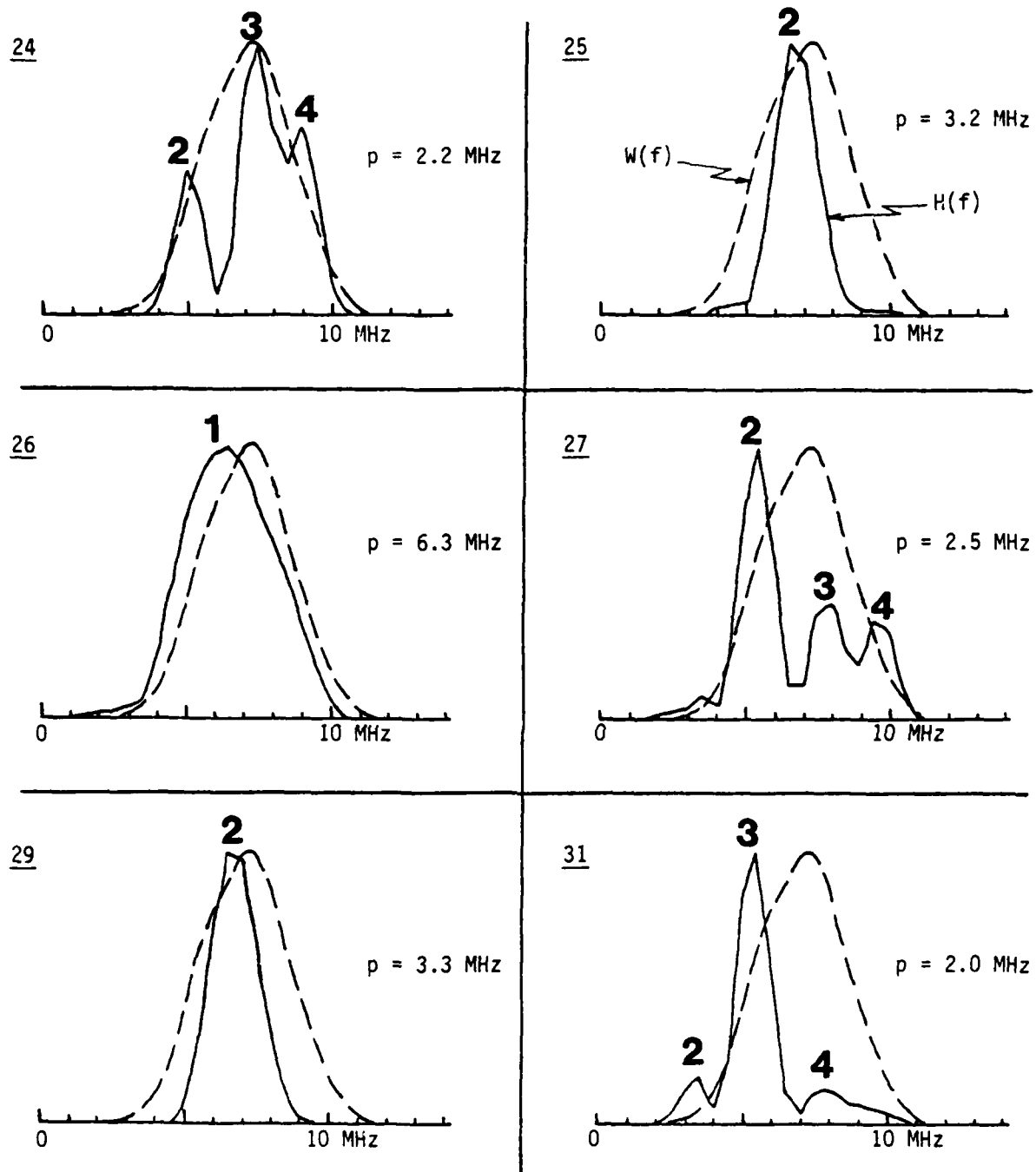
Figure A-16. Magnitude Spectra Obtained for IN100 Inclusions
Nos. 24, 25, 26, 27, 29, and 31 with a 7 MHz
Longitudinal-Wave Transducer

A-17
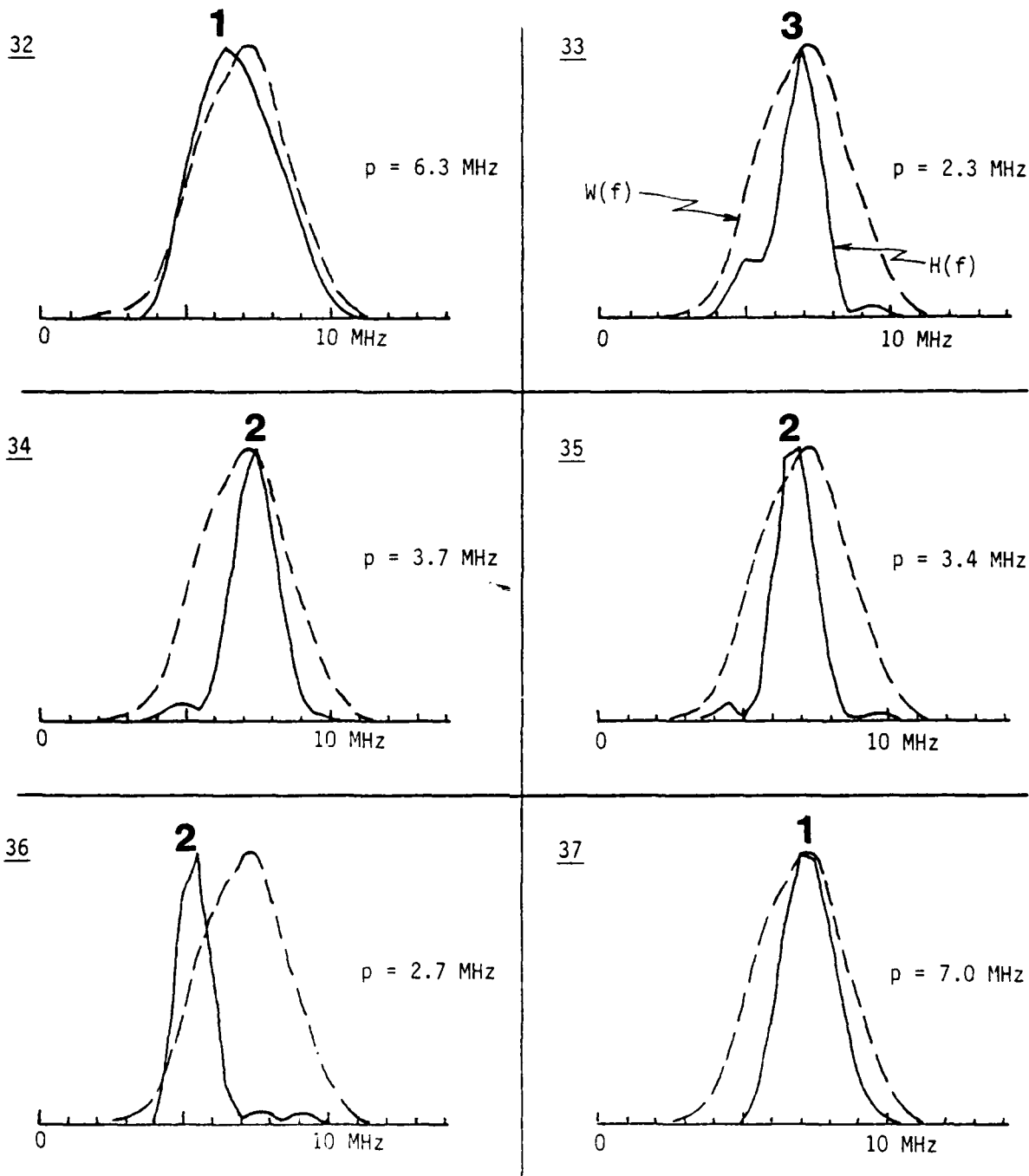
Figure A-17. Magnitude Spectra Obtained for IN100 Inclusions Nos. 32 through 37 with a 7 MHz Longitudinal-Wave Transducer
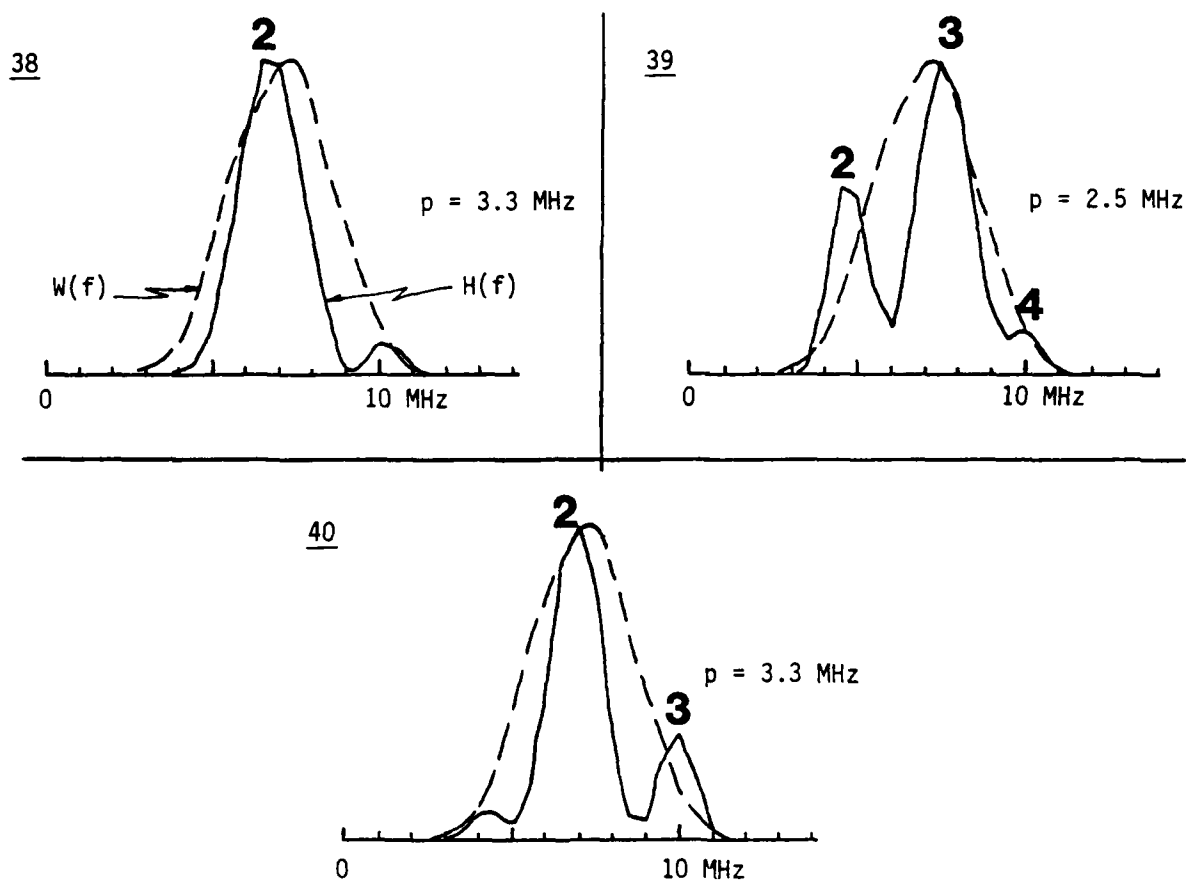
Figure A-18. Magnitude Spectra Obtained for IN100 Inclusions Nos. 38, 39, and 40 with a 7 MHz Longitudinal-Wave Transducer
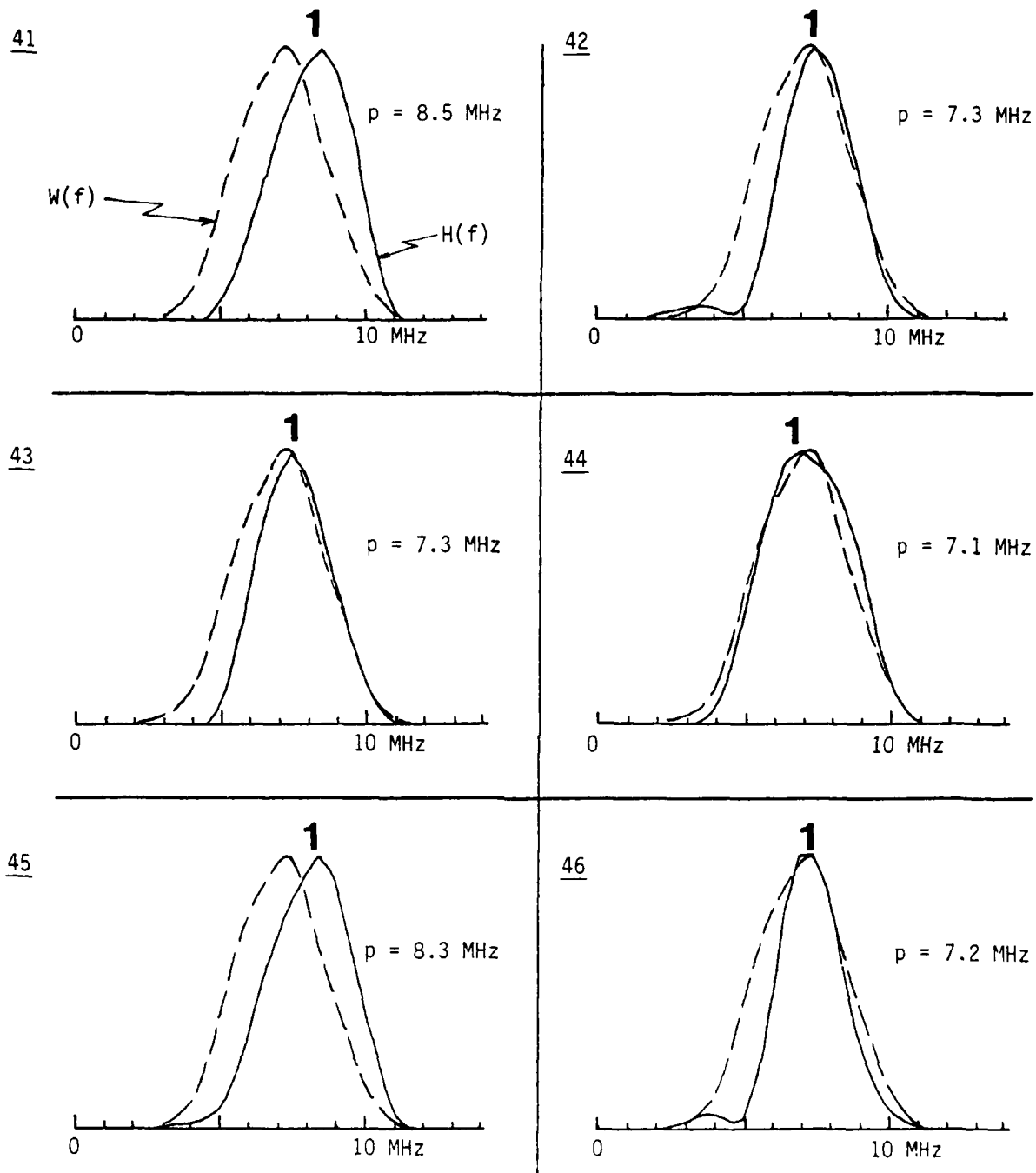
Figure A-19. Magnitude Spectra Obtained for IN100 Flaws Nos. 41 through 46 with a 7 MHz Longitudinal-Wave Transducer

APPENDIX B

AMPLITUDE SPECTRA (INPUT) AND CHARACTERISTIC FUNCTIONS
(OUTPUT) USED IN THE APPLICATION OF THE BORN INVERSION
TECHNIQUE TO SELECTED FLAWS

VOID 01 - 320 μm

AMPLITUDE SPECTRUM   CHARACTERISTIC FUNCTION

A(f)   J(r)

4 MHz   f* = 3.7 MHz   d* = 480 μm
PROBE
               MEAN FREQ.   BORN DIAM.

0   10 MHz   0   500 μm

                                               f* = 7.1 MHz

8 MHz   50%   50%   d* = 220 μm
PROBE

0   10 MHz   0   500 μm

VOID 02 - 1,000 μm

                                               d* = 1,030 μm
2 MHz
PROBE   f* = 1.8 MHz

0   10 MHz   0   500 μm
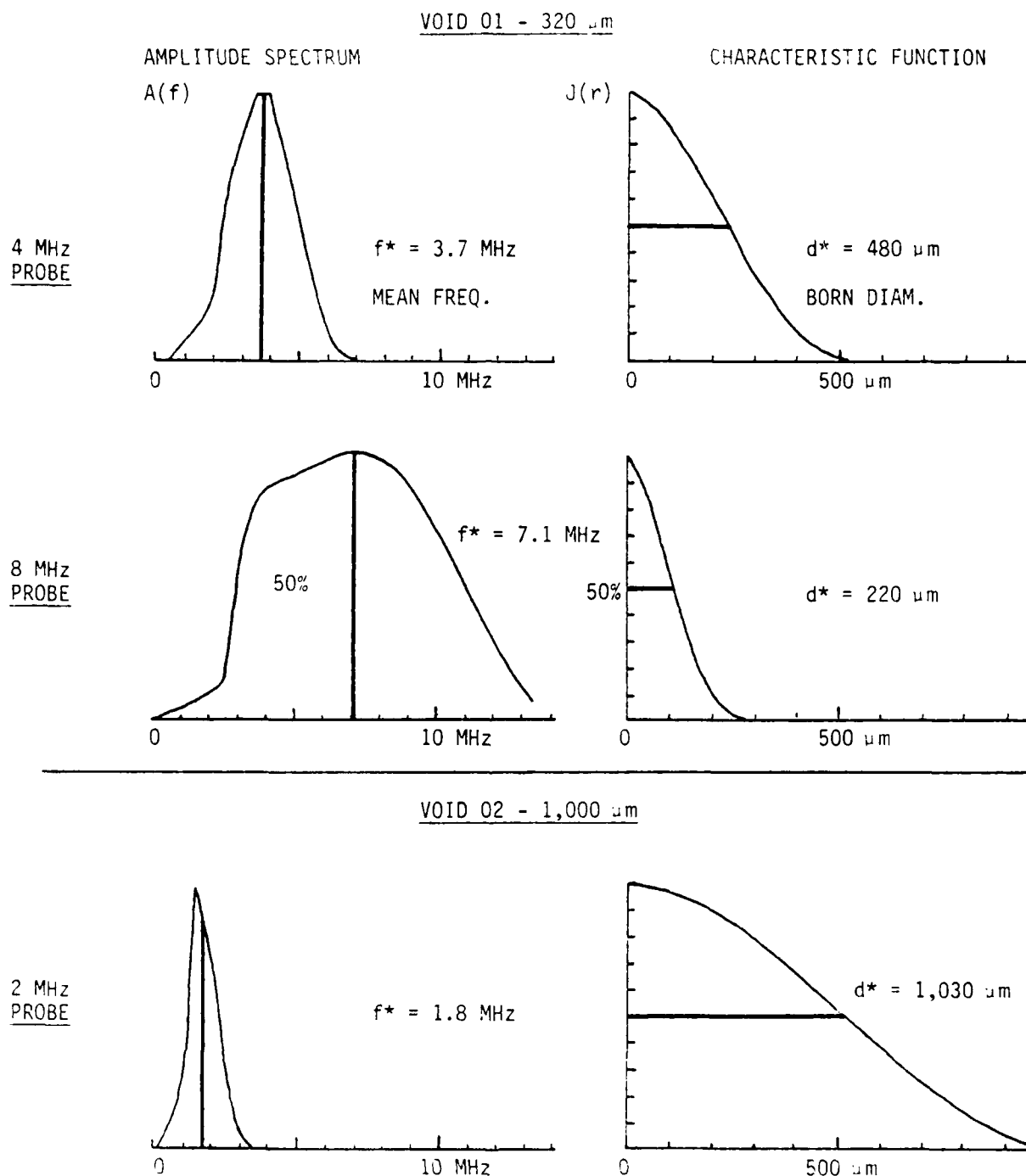
Figure B-1.   Input-Output Relationships Yielded by the Born Inversion
              Algorithm (BIA, Flaws 01 and 02).   Note that k*a*=0.92,
              0.80, and 0.96.

B-2

AMPLITUDE SPECTRUM   CHARACTERISTIC FUNCTION

A(f)   J(r)

4 MHz
PROBE   f* = 3.8 MHz   d* = 470 μm

                 MEAN FREQ.   BORN DIAM.

0   10 MHz   0   500 μm

VOID 03 - 600 μm

2 MHz
PROBE   f* = 1.9 MHz   d* = 980 μm

0   10 MHz   0   500 μm

4 MHz
PROBE   f* = 3.4 MHz   d* = 510 μm

0   10 MHz   0   500 μm
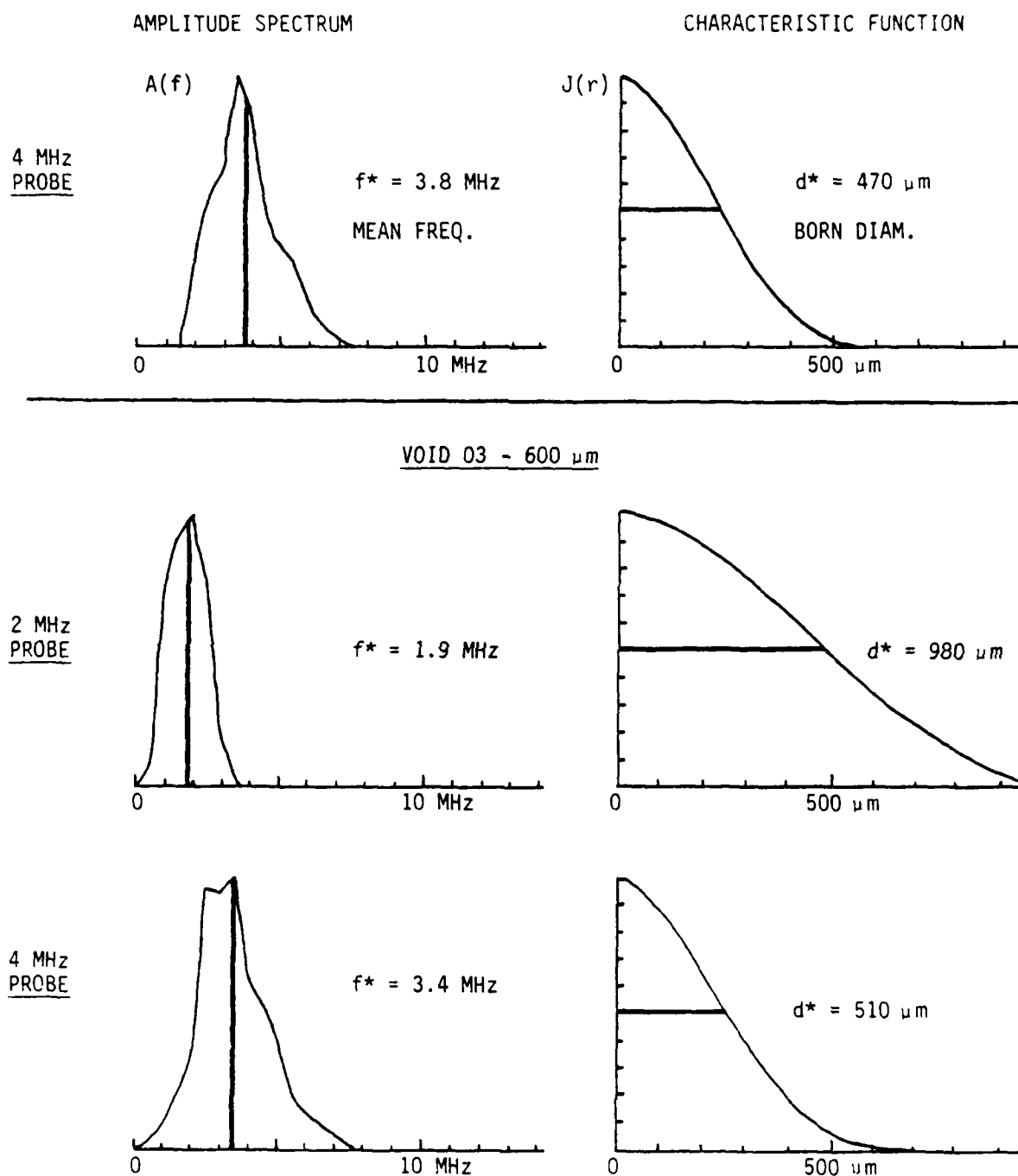
Figure B-2.   Input-Output Relationships Yielded by the BIA (Flaws 02
              and 03). Note that k*a*=0.92, 0.96, and 0.89.

B-3

VOID 04 - 780 μm

AMPLITUDE SPECTRUM   CHARACTERISTIC FUNCTION

A(f)   J(r)

                                              BORN DIAM.
                                               d* = 950 μm

2 MHz   f* = 1.8 MHz
PROBE
             MEAN FREQ.

0   10 MHz   0   500 μm

4 MHz
PROBE   f* = 3.2 MHz   d* = 520 μm

0   10 MHz   0   500 μm

VOID 05 - 1,230 μm

2 MHz
PROBE   f* = 1.8 MHz   d* = 1,000 μm
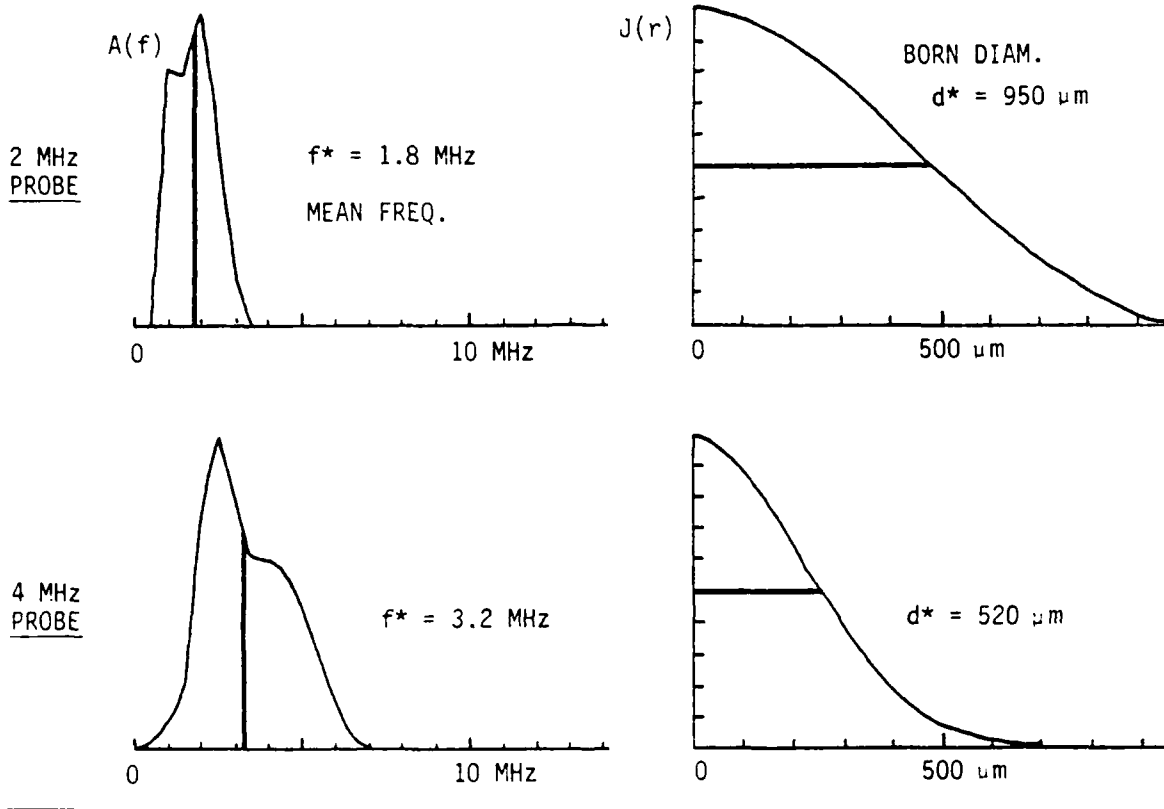
             10 MHz   0   500 μm
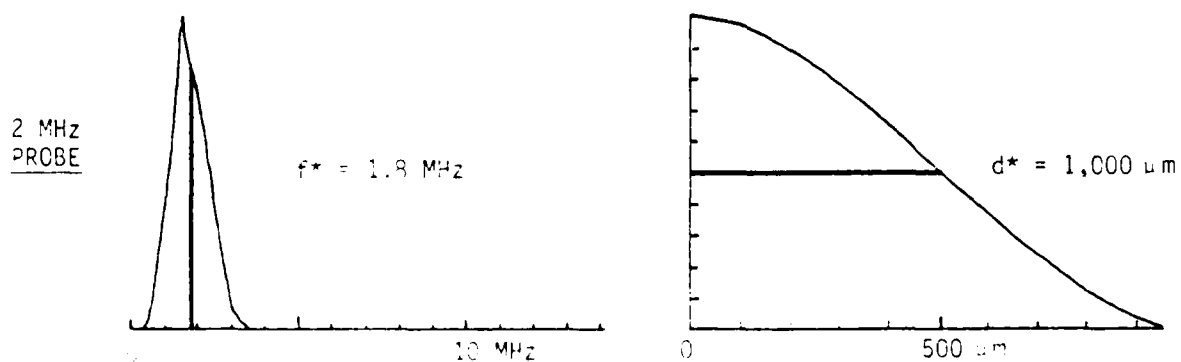
Figure B-3.   Input-Output Relationships Yielded by the BIA (Flaws 04
              and 05).   Note that k*a*=0.88, 0.86, and 0.93.

B-?

VOID 10 - 1,000 μm

AMPLITUDE SPECTRUM	CHARACTERISTIC FUNCTION

A(f)

J(r)

2 MHz
PROBE

BORN DIAM.

d* = 910 μm

f* = 2.0 MHz

MEAN FREQ.

0   10 MHz

0   500 μm

4 MHz
PROBE

f* = 4.0 MHz

d* = 460 μm

0   10 MHz

0   500 μm

INCLUSION 11 - 900 μm

2 MHz
PROBE

f* = 1.9 MHz

d* = 960 um

0   10 MHz
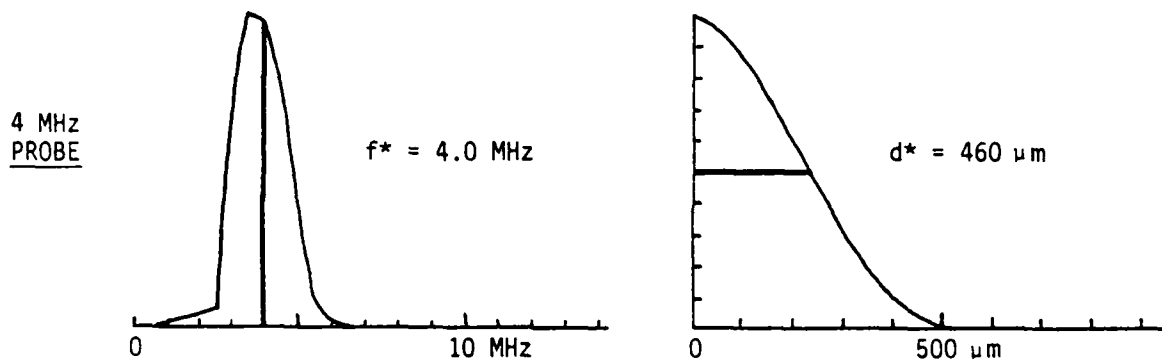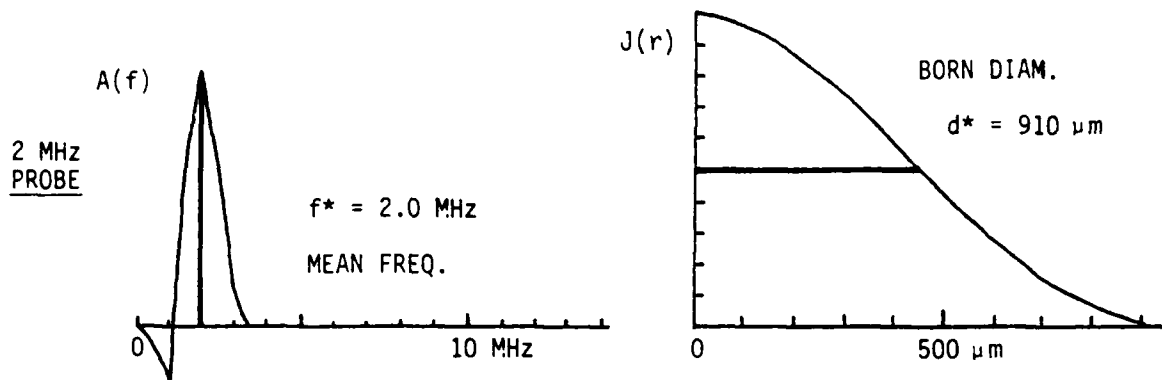
0   500 um
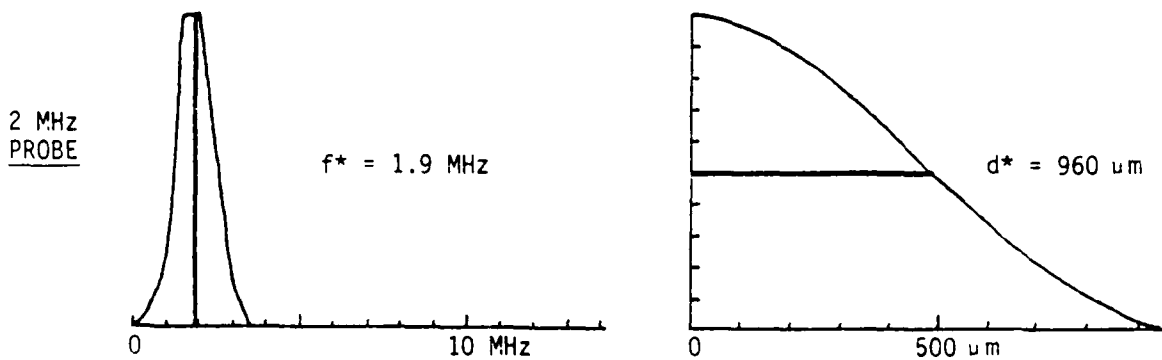
Figure B-4.   Input-Output Relationships Yielded by the BIA (Flaws 10
and 11).   Note that k*a*=0.94, 0.95, and 0.94.

AMPLITUDE SPECTRUM   CHARACTERISTIC FUNCTION
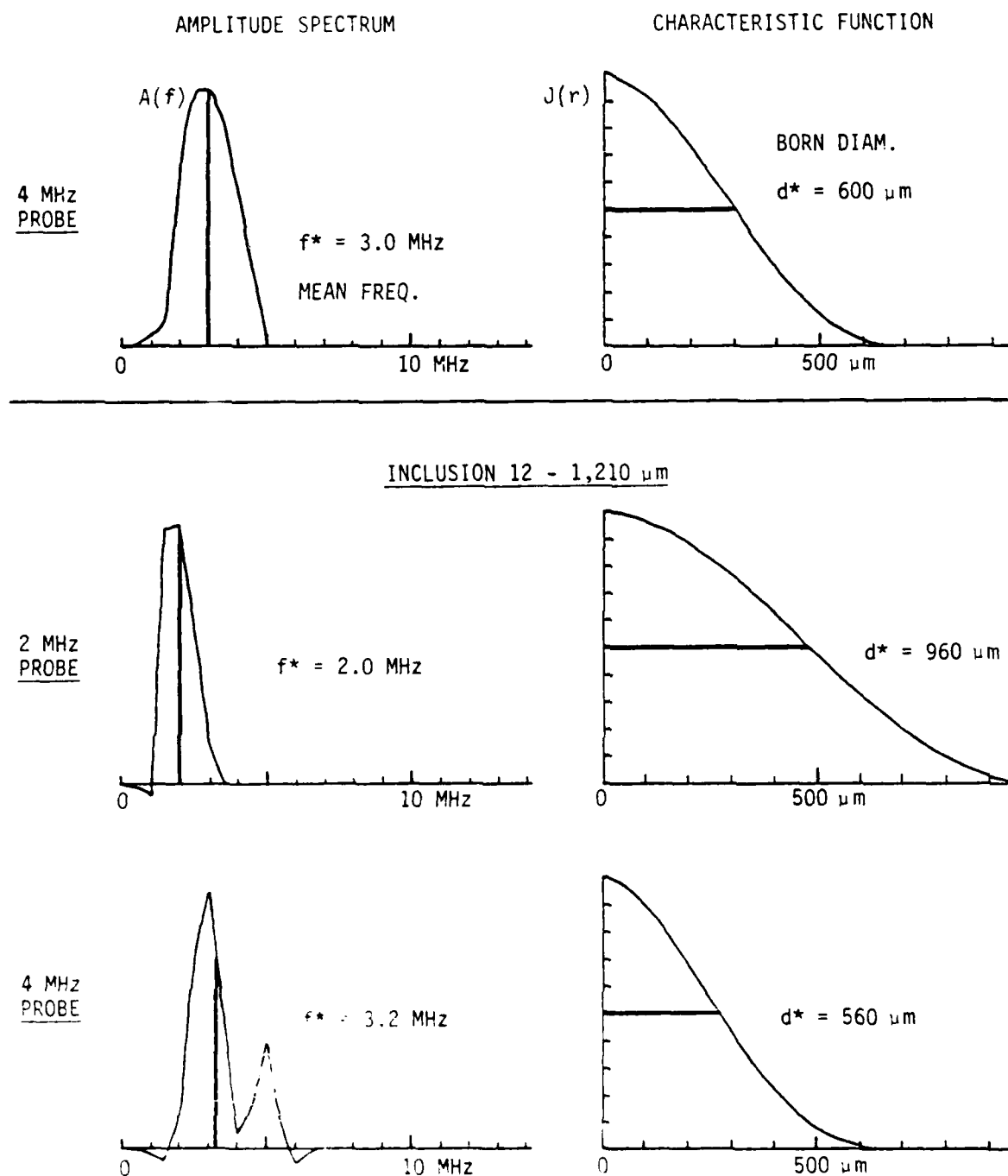
Figure B-5.   Input-Output Relationships Yielded by the BIA (Flaws 11
              and 12).   Note that k*a*=0.93, 0.99, and 0.92.

INCLUSION 16 - 410 μm

AMPLITUDE SPECTRUM   CHARACTERISTIC FUNCTION

A(f)   J(r)

7 MHz
PROBE   f* = 6.3 MHz   d* = 270 μm

               MEAN FREQ.   BORN DIAM.

0   10 MHz   0   500 μm

INCLUSION 22 - 990 μm

2 MHz
PROBE   f* = 1.6 MHz   d* = 1,030 μm

0   10 MHz   0   500 μm

5 MHz
PROBE   f* = 3.8 MHz   d* = 470 μm
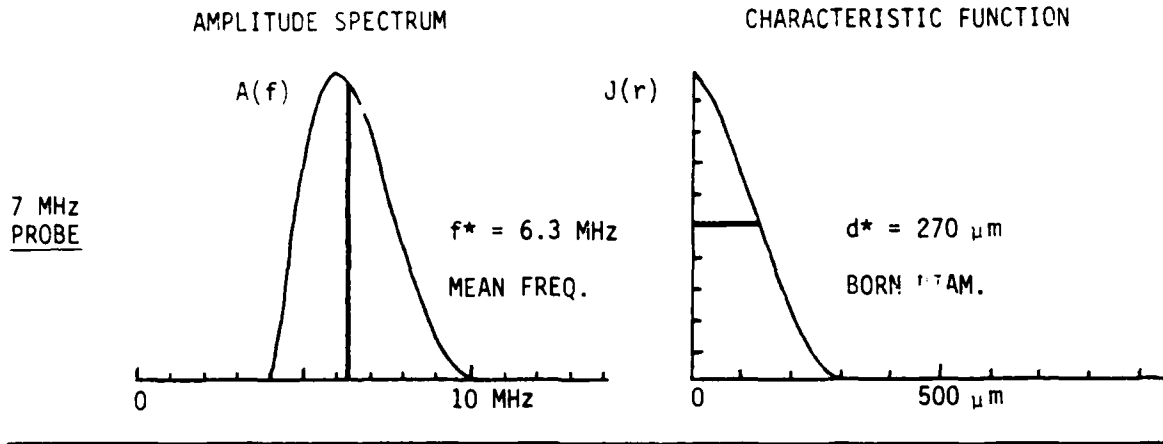
0   10 MHz   0   500 μm
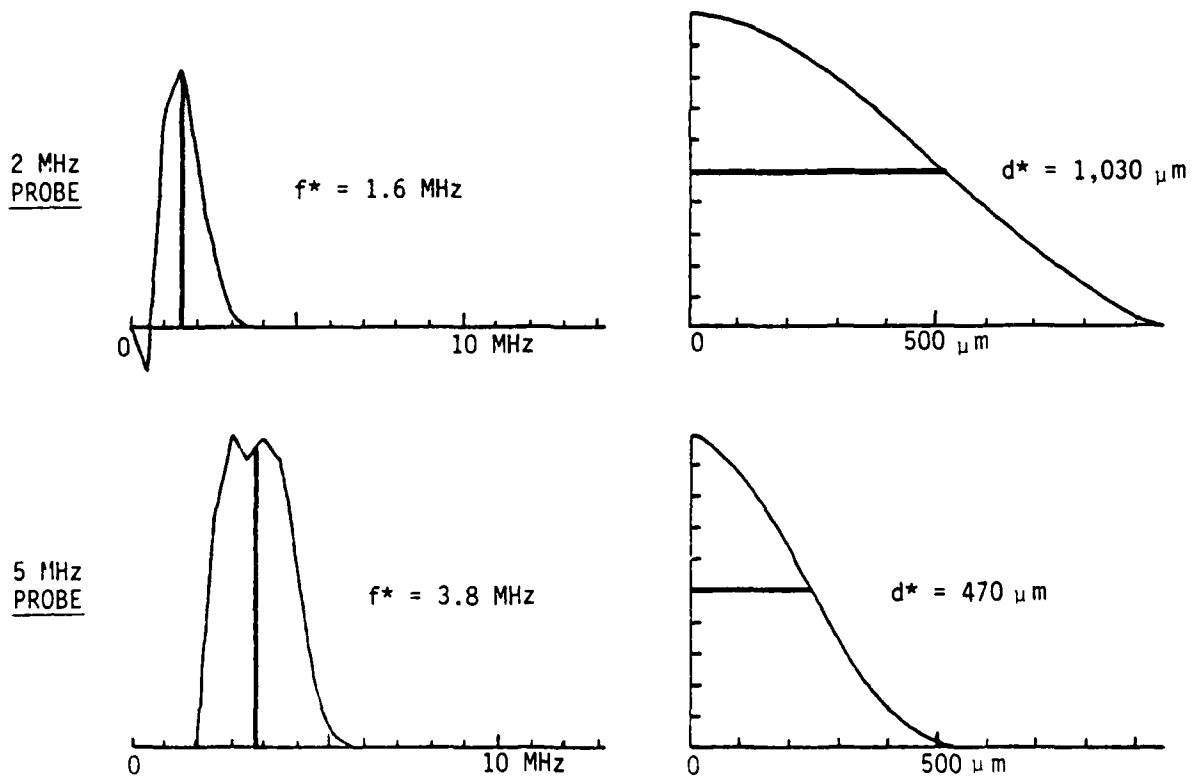
Figure B-6.   Input-Output Relationships Yielded by the BIA (Flaws 16
               and 22).   Note that k*a*=0.88, 0.85, and 0.92.

REAL FLAW 41 - 140 x 610 x 100 μm

AMPLITUDE SPECTRUM   CHARACTERISTIC FUNCTION

A(f)   J(r)

7 MHz
PROBE   f* = 6.6 MHz   d* = 270 μm

                         MEAN FREQ.   BORN DIAM.

0   10 MHz   0   500 μm

REAL FLAW 42 - 150 x 230 x 150 μm

7 MHz
PROBE   f* = 6.4 MHz   d* = 260 μm

0   10 MHz   0   500 μm

REAL FLAW 43

7 MHz
PROBE   f* = 6.7 MHz   d* = 260 μm

0   10 MHz   0   500 μm
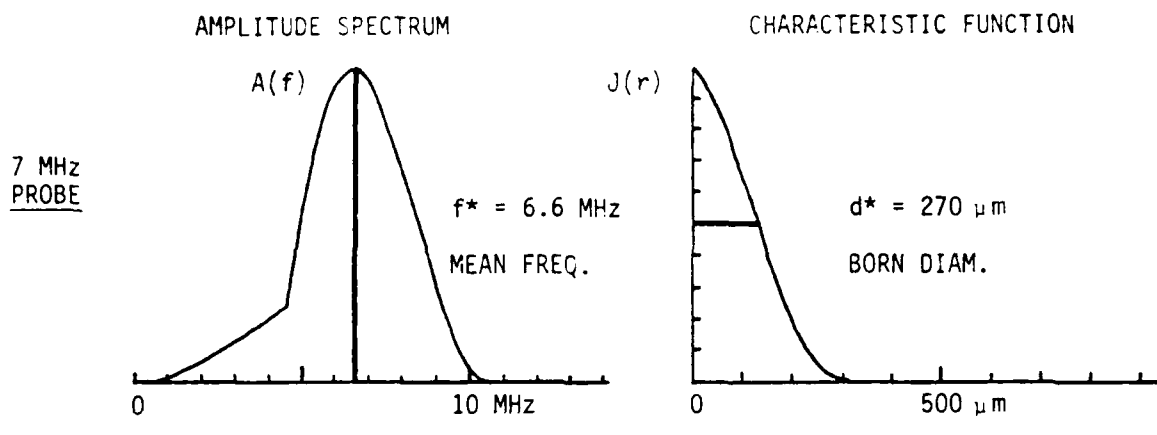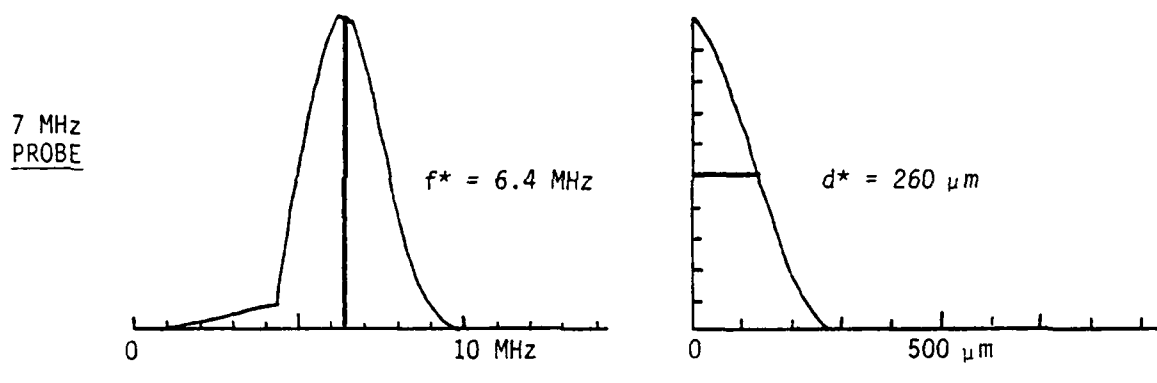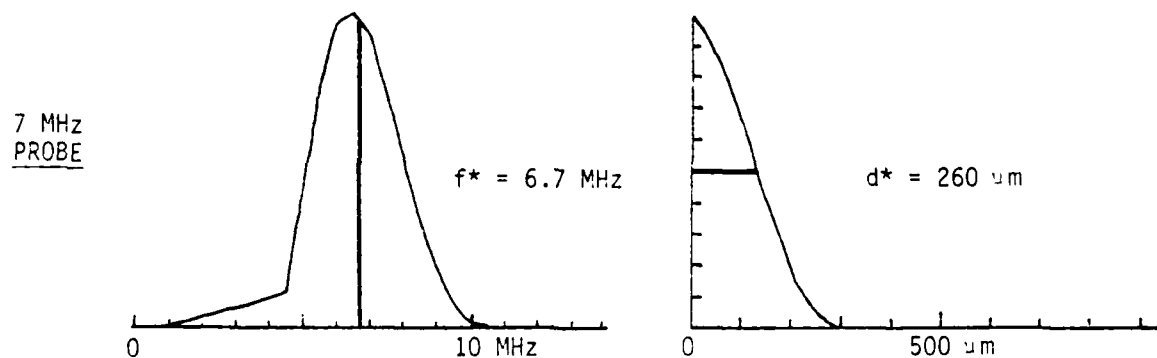
Figure B-7.   Input-Output Relationships Yielded by the BIA (Flaws 41
              through 43).   Note that k*a*=0.92, 0.86, and 0.90.

REAL FLAW 44 - 370 x 500 x 90 μm

AMPLITUDE SPECTRUM   CHARACTERISTIC FUNCTION

A(f)   J(r)

7 MHz
PROBE   f* = 6.0 MHz   d* = 290 μm

                         MEAN FREQ.   BORN DIAM.

0   10 MHz   0   500 μm

REAL FLAW 45

7 MHz
PROBE   f* = 6.3 MHz   d* = 270 μm

0   10 MHz   0   500 μm

REAL FLAW 46

7 MHz
PROBE   f* = 6.7 MHz   d* = 260 μm

0   10 MHz   0   500 μm
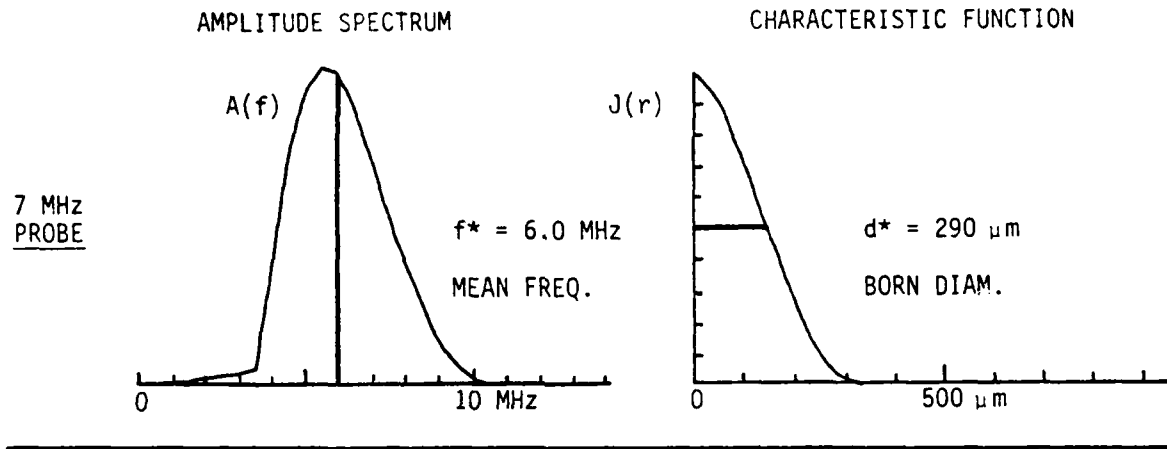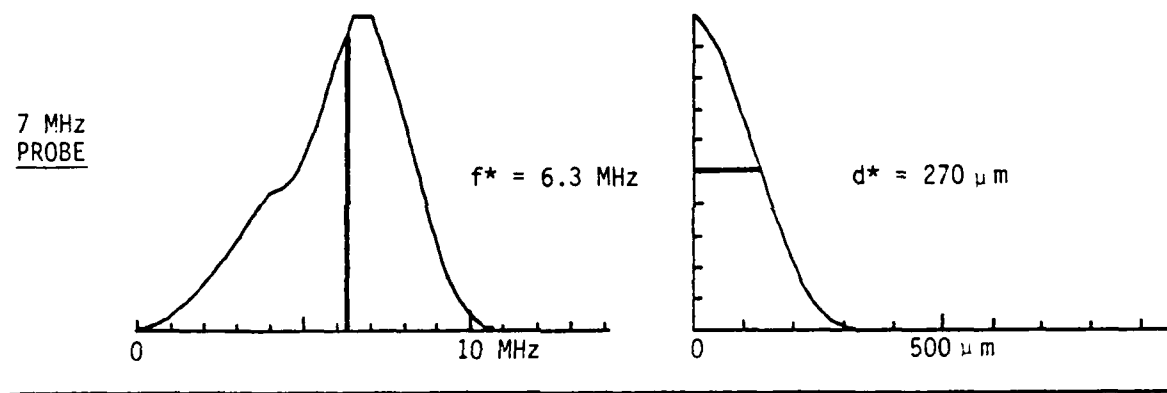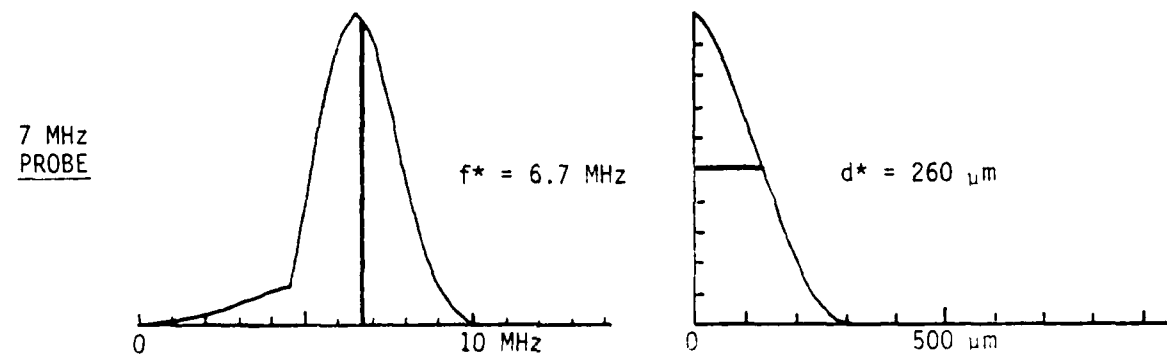
Figure B-8.   Input-Output Relationships Yielded by the BIA (Flaws 44
              through 46).   Note that k*a*=0.90, 0.88, and 0.90.

APPENDIX C

LONGITUDINAL- AND SHEAR-WAVE SIGNATURES
USED IN THE APPLICATION OF THE
SATELLITE-PULSE OBSERVATION TECHNIQUE
TO THE 42 TEST FLAWS

FLAW WAVEFORM
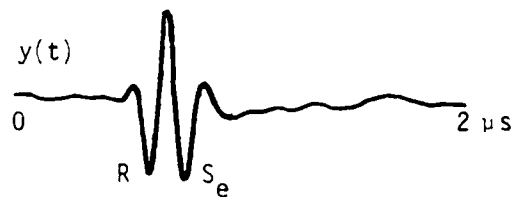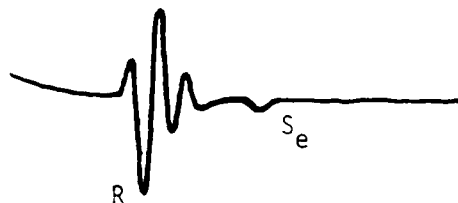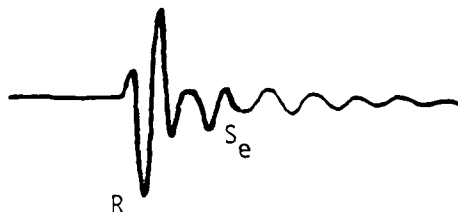
y(t)

0   2 μs

R S$_e$

VOID 01 - 320 μm

c_e = 150 ns   d = 330 μm

S$_e$

R

VOID 02 - 1,000 μm

c_e = 510 ns   d = 1,110 μm

S$_e$

R

VOID 03 - 600 μm

c_e = 285 ns   d = 620 μm

S$_e$

R

VOID 04 - 780 μm

σ_e = 375 ns   d = 820 μm

R   S$_e$

σ_e
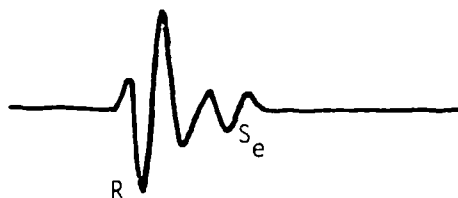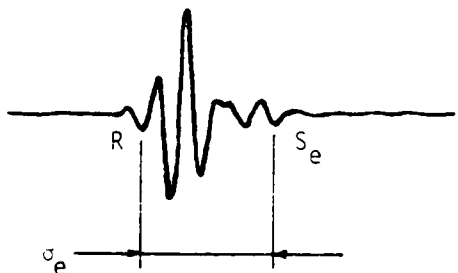
VOID 05 - 1,230 μm

c_e = 600 ns   d = 1,310 μm

Figure C-1.   Longitudinal-Wave Signatures of the Voids
in Titanium Specimen No. FML 97413

FLAW WAVEFORM
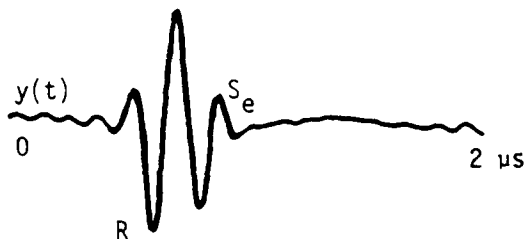
VOID 01 - 320 μm
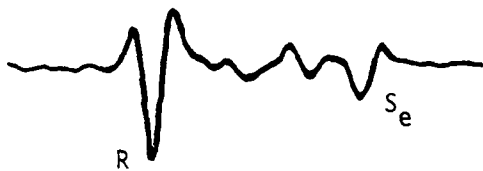
σ_e = 290 ns   d = 330 μm

VOID 02 - 1,000 μm

σ_e = 925 ns   d = 1,060 μm

VOID 03 - 600 μm

σ_e = 620 ns   d = 710 μm
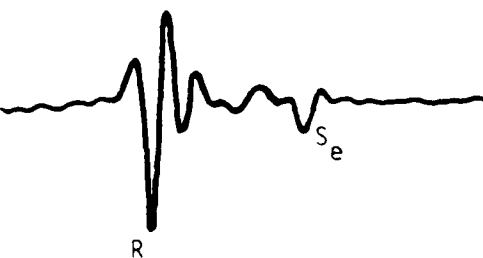
VOID 04 - 780 μm

σ_e = 670 ns   d = 770 μm
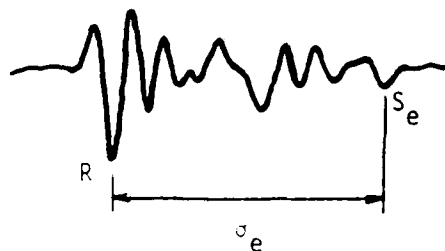
VOID 05 - 1,230 μm

σ_e = 1,205 ns   d = 1,390 μm

Figure C-2.   Shear-Wave Signatures of the Voids
in Titanium Specimen No. FML 97413
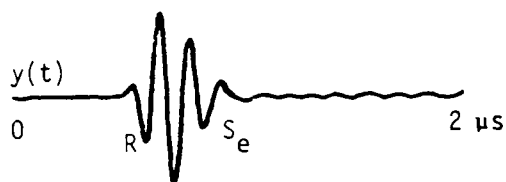
FLAW WAVEFORM

VOID 06 - 600 μm

σ_e = 260 ns   d = 570 μm

VOID 07 - 1,230 μm

σ_e = 525 ns   d = 1,150 μm
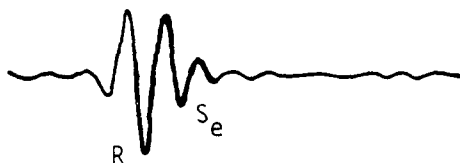
VOID 08 - 320 μm

σ_e = 160 ns   d = 350 μm
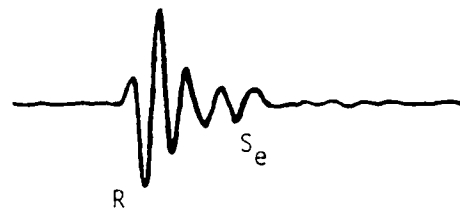
VOID 09 - 780 μm

σ_e = 405 ns   d = 880 μm
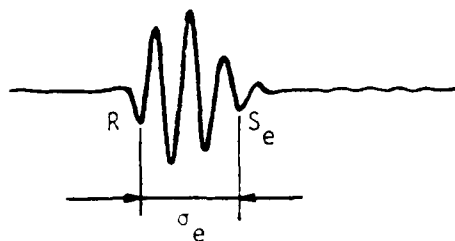
VOID 10 - 1,000 μm

σ_e = 445 ns   d = 970 μm

Figure C-3.   Longitudinal-Wave Signatures of the
Voids in IN100 Specimen No. FML 97414

C-4

FLAW WAVEFORM

VOID 06 - 600 μm

σ_e = 500 ns   d = 580 μm

VOID 07 - 1,230 μm

σ_e = 1,330 ns   d = 1,530 μm

VOID 08 - 320 μm

σ_e = 240 ns   d = 280 μm

VOID 09 - 780 μm

σ_e = 720 ns   d = 830 μm

VOID 10 - 1,000 μm

σ_e = 1,070 ns   d = 1,230 μm

Figure C-4. Shear-Wave Signatures of the Voids
in IN100 Specimen No. FML 97414

FLAW WAVEFORM
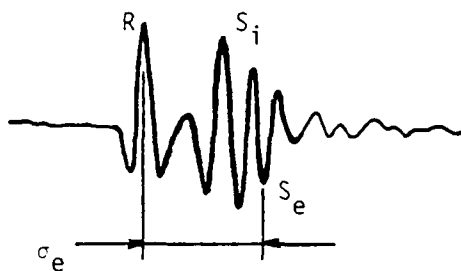
σ_i

R S_i

y(t)

0

2 μs

S_e

INCLUSION 11 - 900 μm

σ_i = 275 ns, σ_e = 425 ns

d = 910 μm   d = 930 μm

R S_i

S_e

σ_e

INCLUSION 12 - 1,210 μm

σ_i = 355 ns, σ_e = 540 ns

d = 1,170 μm   d = 1,180 μm

R S_i

S_e

INCLUSION 13 - 1,210 μm

σ_i = 340 ns, σ_e = 535 ns

d = 1,120 μm   d = 1,170 μm

R S_i

S_e

INCLUSION 14 - 900 μm

σ_i = 275 ns, σ_e = 430 ns

d = 910 μm   d = 940 μm

S_i

R

S_e

INCLUSION 15 - 480 μm

σ_i = 155 ns, σ_e = 220 ns

d = 510 μm   d = 480 μm
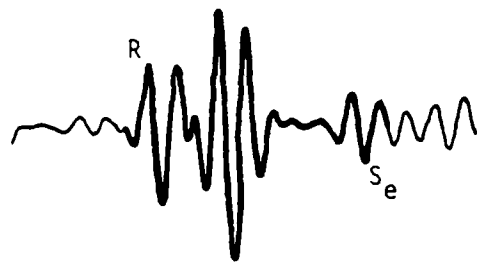
Figure C-5.   Longitudinal-Wave Signatures of the Inclusions
in Titanium Specimen No. FML 97416

FLAW WAVEFORM
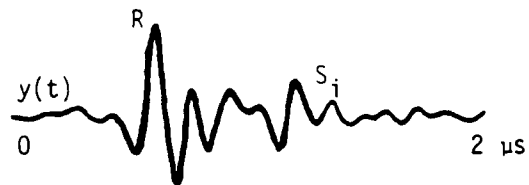
INCLUSION 11 - 900 μm

σ_i = 625 ns   d = 910 μm
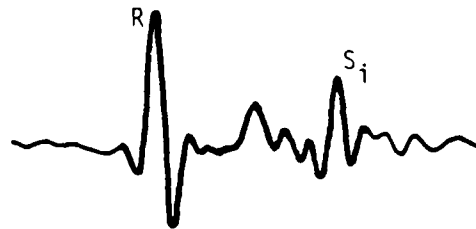
INCLUSION 12 - 1,210 μm

σ_i = 800 ns   d = 1,160 μm

INCLUSION 13 - 1,210 μm

σ_i = 800 ns   d = 1,160 μm

INCLUSION 14 - 900 μm

σ_i = 635 ns   d = 920 μm
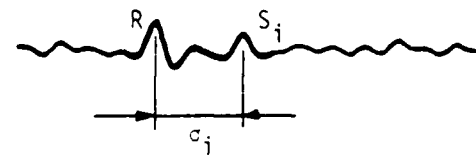
INCLUSION 15 - 480 μm

σ_i = 390 ns   d = 520 μm

Figure C-6.   Shear-Wave Signatures of the Inclusions
in Titanium Specimen No. FML 97416

FLAW WAVEFORM

INCLUSION 16 - 410 μm

σ_e = 205 ns   d = 450 μm

INCLUSION 19 - 790 μm

σ_e = 360 ns   d = 790 μm

INCLUSION 20 - 790 μm

σ_e = 360 ns   d = 790 μm

INCLUSION 21 - 790 μm

σ_e = 380 ns   d = 830 μm

INCLUSION 22 - 990 μm

σ_e = 510 ns   d = 1,110 μm
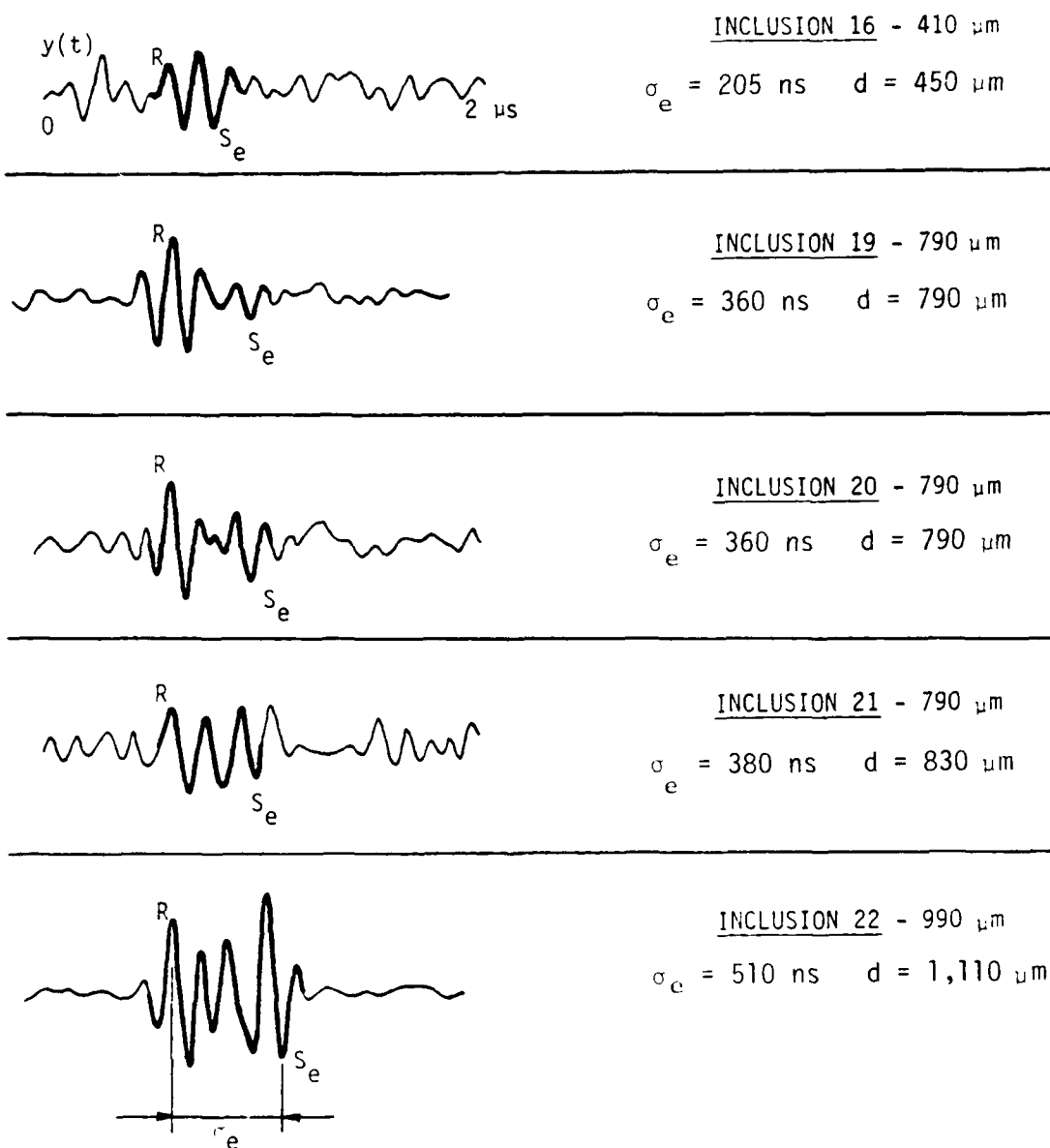
Figure C-7.   Longitudinal-Wave Signatures of the Inclusions
in IN100 Specimen Nos. FML 97474-1 through -3

FLAW WAVEFORM
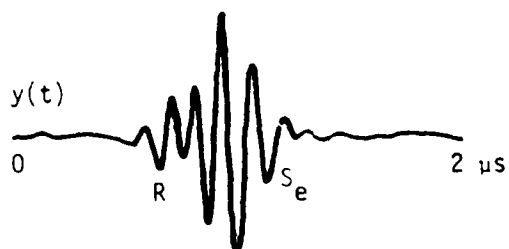
INCLUSION 23 - 990 μm
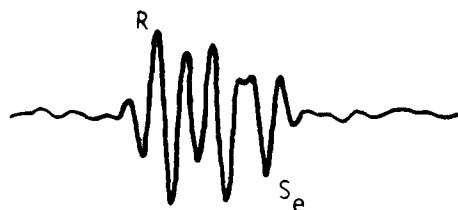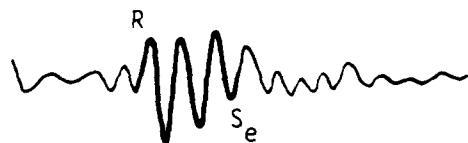
σ_e = 480 ns   d = 1,050 μm

INCLUSION 24 - 990 μm

σ_e = 470 ns   d = 1,030 μm

INCLUSION 25 - 790 μm

σ_e = 360 ns   d = 790 μm
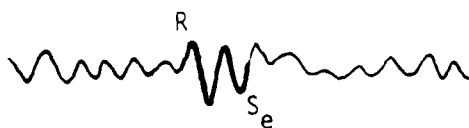
INCLUSION 26 - 410 μm
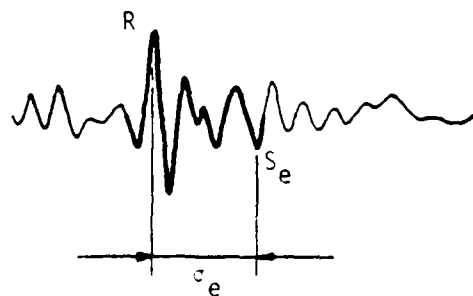
σ_e = 200 ns   d = 440 μm

INCLUSION 27 - 990 μm

σ_e = 450 ns   d = 980 μm

Figure C-8.   Longitudinal-Wave Signatures of the Inclusions
in IN100 Specimen Nos. FML 97474-3 and -4

FLAW WAVEFORM
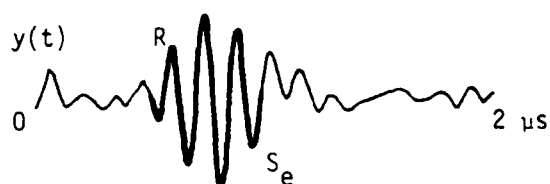
INCLUSION 29 - 790 μm
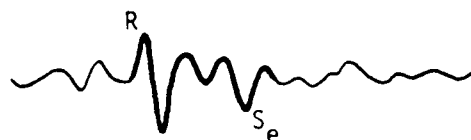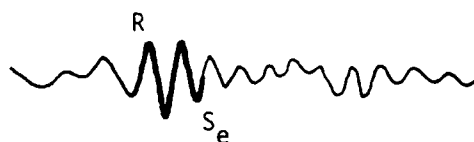
σ_e = 355 ns   d = 770 μm

INCLUSION 31 - 990 μm

σ_e = 450 ns   d = 980 μm

INCLUSION 32 - 410 μm

σ_e = 200 ns   d = 440 μm
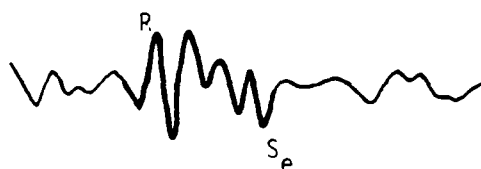
INCLUSION 33 - 990 μm

σ_e = 485 ns   d = 1,060 μm
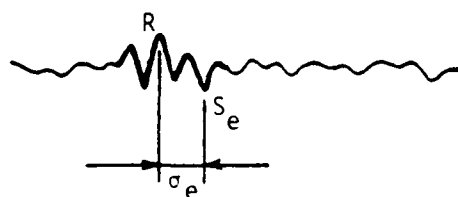
INCLUSION 34 - 410 μm

σ_e = 200 ns   d = 440 μm

Figure C-9.   Longitudinal-Wave Signatures of the Inclusions
in IN100 Specimen Nos. FML 97474-5 through -7

FLAW WAVEFORM
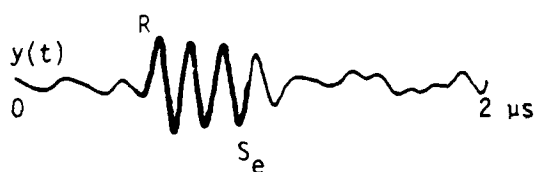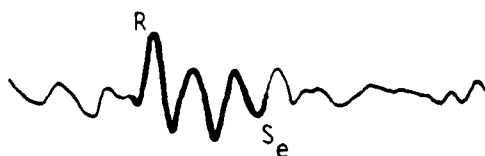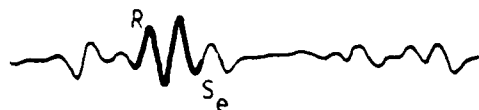
$y(t)$ R

S_e 2 μs
0

INCLUSION 35 - 790 μm

σ_e = 360 ns   d = 790 μm

R

S_e

INCLUSION 36 - 990 μm

σ_e = 460 ns   d = 1,000 μm

R

S_e

INCLUSION 37 - 410 um

σ_e = 190 ns   d = 410 μm

R

S_e

INCLUSION 38 - 790 μm

σ_e = 355 ns   d = 770 μm

R

S_e

INCLUSION 39 - 990 um

σ_e = 465 ns   d = 1,010 μm

R

S_e

σ_e
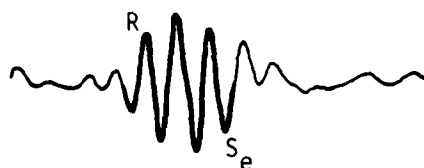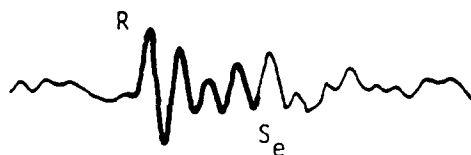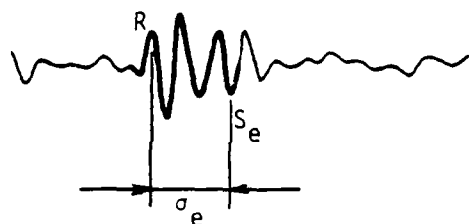
INCLUSION 40 - 790 μm
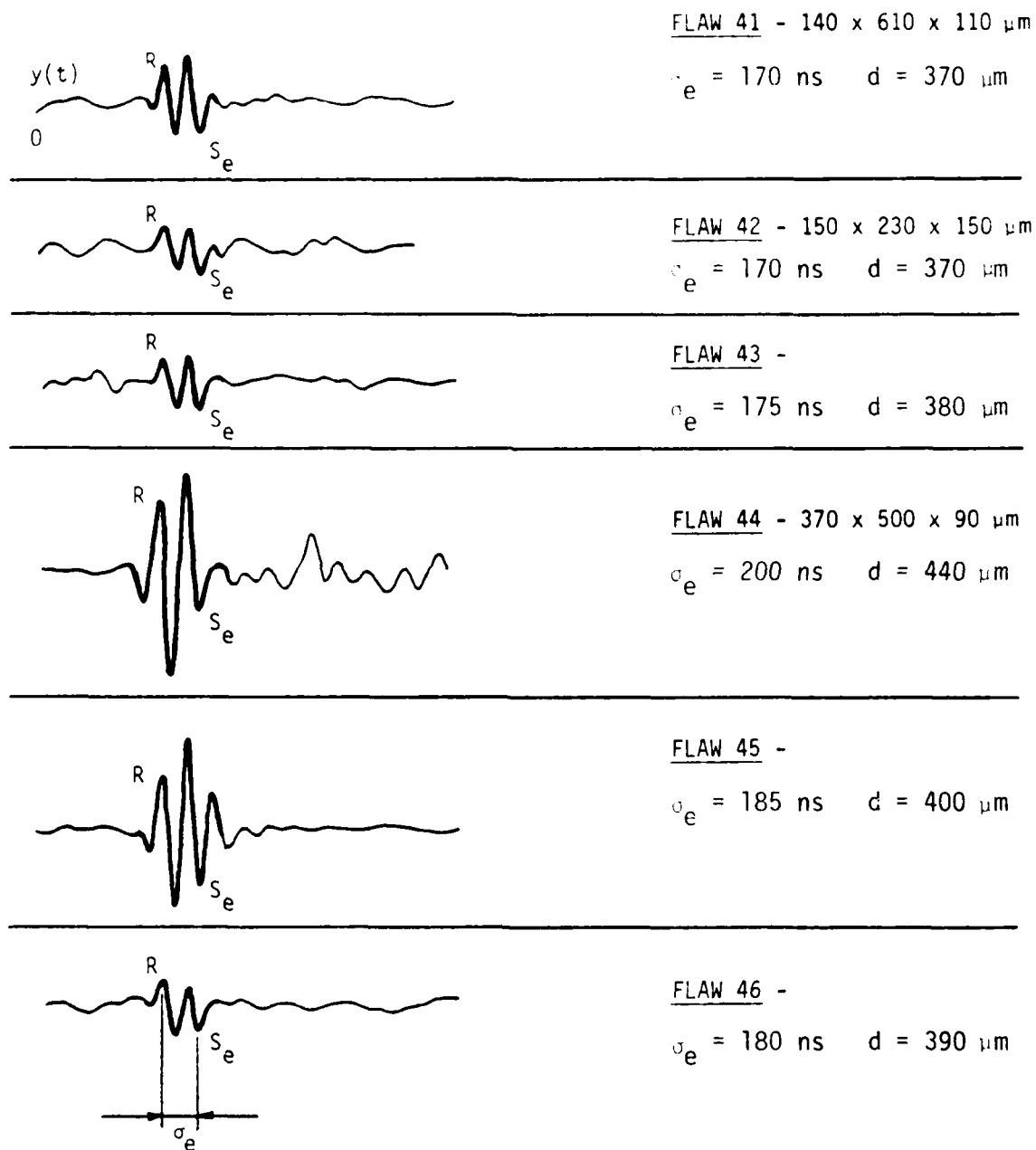
σ_e = 355 ns   d = 770 μm

Figure C-10.   Longitudinal-Wave Signatures of the Inclusions
in IN100 Specimen Nos. FML 97474-7 and -8

FLAW WAVEFORM
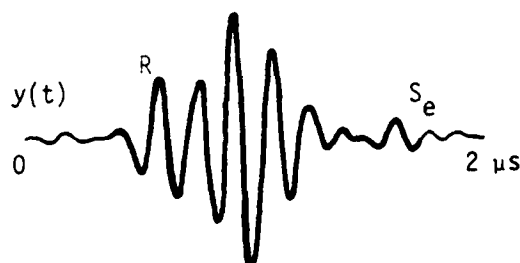
INCLUSION 22 - 990 μm

σ_e = 1,050 ns   d = 1,210 μm

INCLUSION 23 - 990 μm

σ_e = 970 ns   d = 1,120 μm
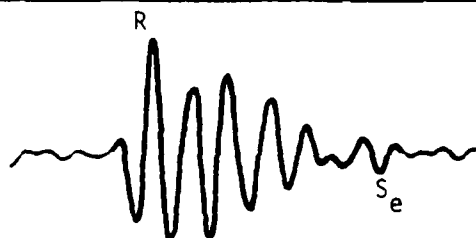
INCLUSION 24 - 990 μm

σ_e = 1,005 ns   d = 1,160 μm
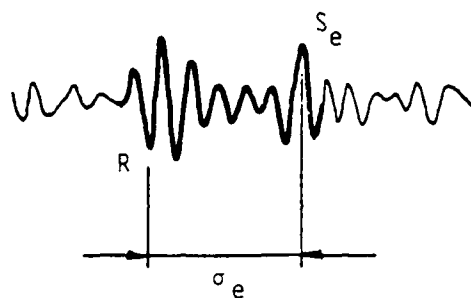
INCLUSION 25 - 790 μm

σ_e = 685 ns   d = 790 μm

Figure C-11.   Shear-Wave Signatures of the Inclusions
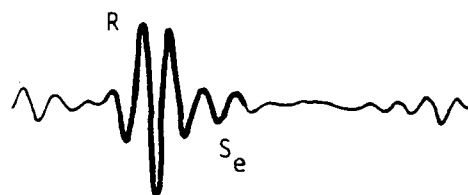in IN100 Specimen Nos. FML 97474-3 and -4

FLAW WAVEFORM
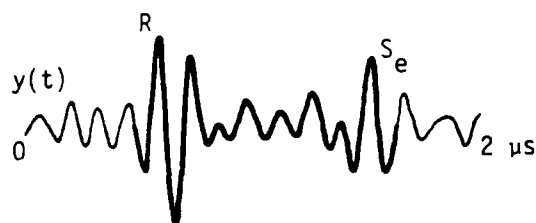
INCLUSION 27 - 990 μm

σ_e = 940 ns   d = 1,080 μm

INCLUSION 29 - 790 μm

σ_e = 660 ns   d = 760 μm

INCLUSION 31 - 990 μm

σ_e = 930 ns   d = 1,070 μm

INCLUSION 33 - 990 μm

σ_e = 805 ns   d = 930 μm
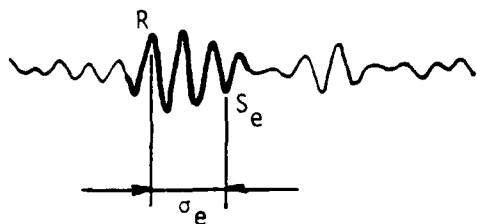
INCLUSION 34 - 410 μm

σ_e = 325 ns   d = 370 μm

Figure C-12.   Shear-Wave Signatures of the Inclusions
in IN100 Specimen Nos. FML 97474-4 through -7
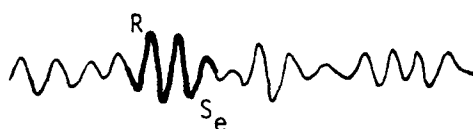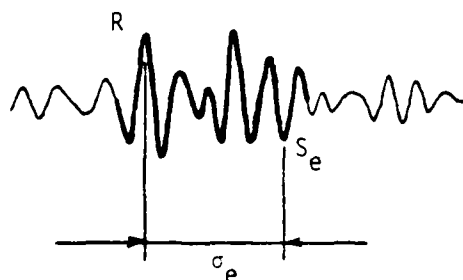
Figure C-13. Shear-Wave Signatures of the Inclusions in IN100 Specimen Nos. FML 97474-7 and -8

FLAW WAVEFORM

FLAW 41 - 140 x 610 x 110 μm

σ_e = 170 ns   d = 370 μm

FLAW 42 - 150 x 230 x 150 μm
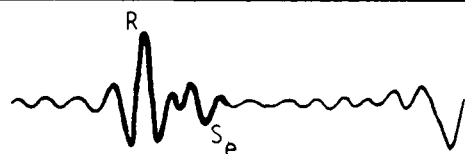
σ_e = 170 ns   d = 370 μm

FLAW 43 -

σ_e = 175 ns   d = 380 μm

FLAW 44 - 370 x 500 x 90 μm

σ_e = 200 ns   d = 440 μm

FLAW 45 -

σ_e = 185 ns   d = 400 μm

FLAW 46 -

σ_e = 180 ns   d = 390 μm

Figure C-14.   Longitudinal-Wave Signatures of the Real Flaws
in IN100 Specimen Nos. FML 97600-1 and -2

FLAW WAVEFORM

$y(t)$

R

S_e

0   2 µs

FLAW 41 - 140 x 610 x 110 µm

σ_e = 340 ns   d = 390 µm

R

S_e

FLAW 42 - 150 x 230 x 150 µm

σ_e = 350 ns   d = 400 µm

R

S_e

FLAW 43 -

σ_e = 275 ns   d = 320 µm

R

S_e

FLAW 44 - 370 x 500 x 90 µm

σ_e = 320 ns   d = 370 µm

R

S_e

FLAW 45 -

σ_e = 210 ns   d = 240 µm

R

S_e

σ_e
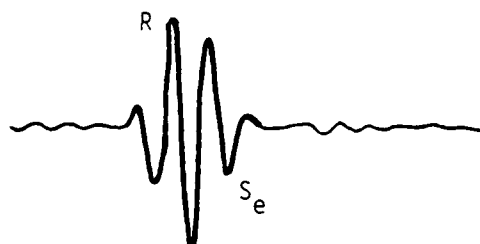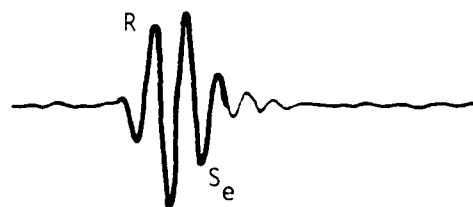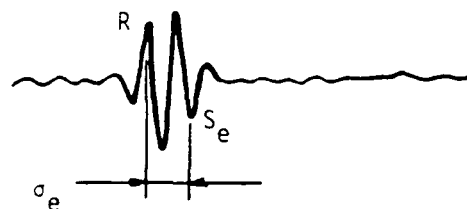
FLAW 46 -

σ_e = 190 ns   d = 220 µm

Figure C-15.   Shear-Wave Signatures of the Real Flaws in
IN100 Specimen Nos. FML 97600-1 and -2

APPENDIX D

LONGITUDINAL- AND SHEAR-WAVE PROFILES
USED IN THE APPLICATION OF THE
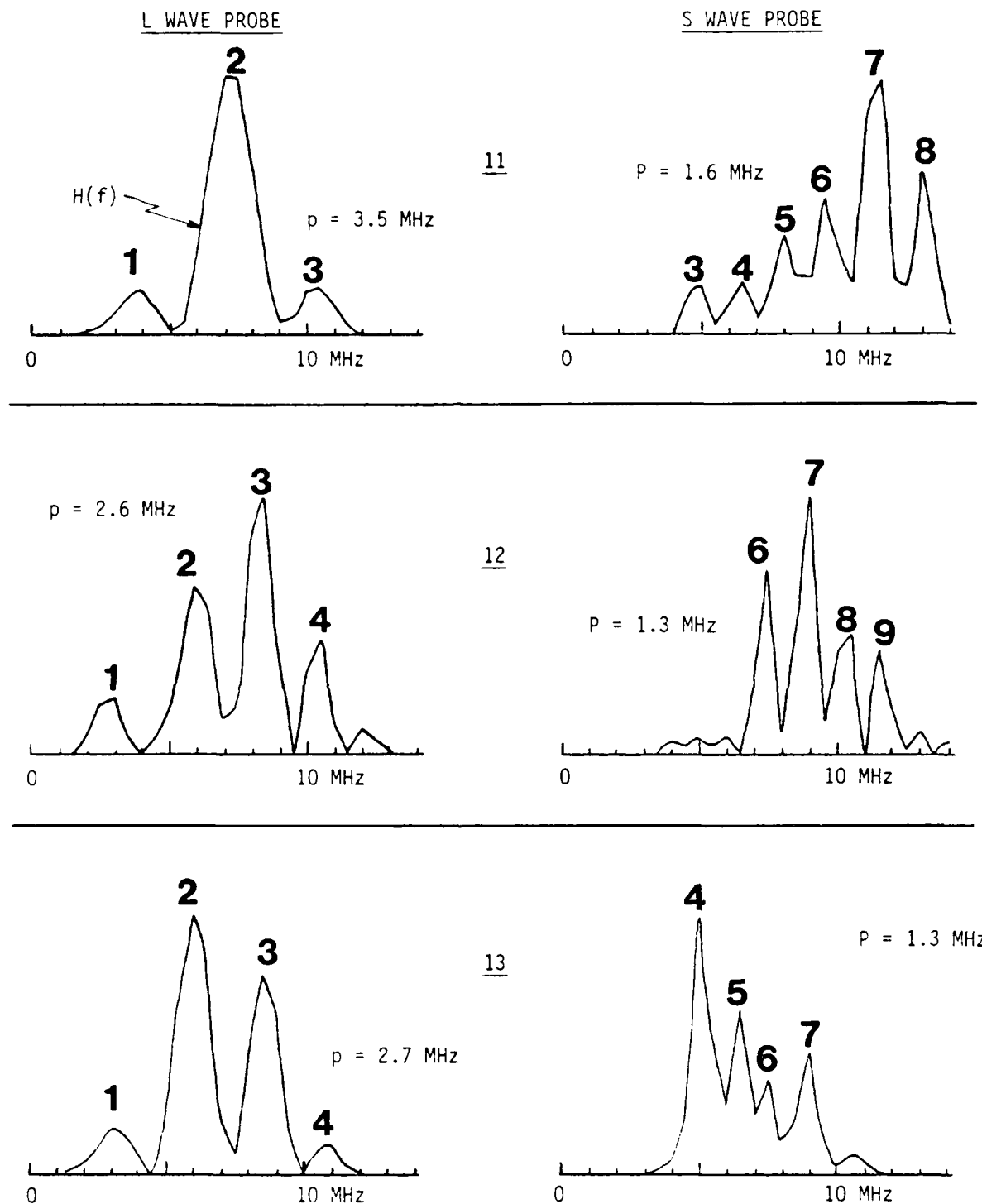SEMIAUTOMATED SATELLITE ANALYSIS PROCEDURES
TO THE 32 DETECTED INCLUSIONS

L WAVE PROBE   S WAVE PROBE

H(f)

p = 3.5 MHz   11   P = 1.6 MHz

1 2 3   3 4 5 6 7 8

0   10 MHz   0   10 MHz

p = 2.6 MHz   12   P = 1.3 MHz

1 2 3 4   6 7 8 9

0   10 MHz   0   10 MHz

2 3   4 5
1   4   6 7
p = 2.7 MHz   P = 1.3 MHz

0   10 MHz   0   10 MHz

Figure D-1. Longitudinal- and Shear-Wave Profiles of the Inclusions
             in Titanium Specimen No. FML 97416 (Flaws 11 through 13)
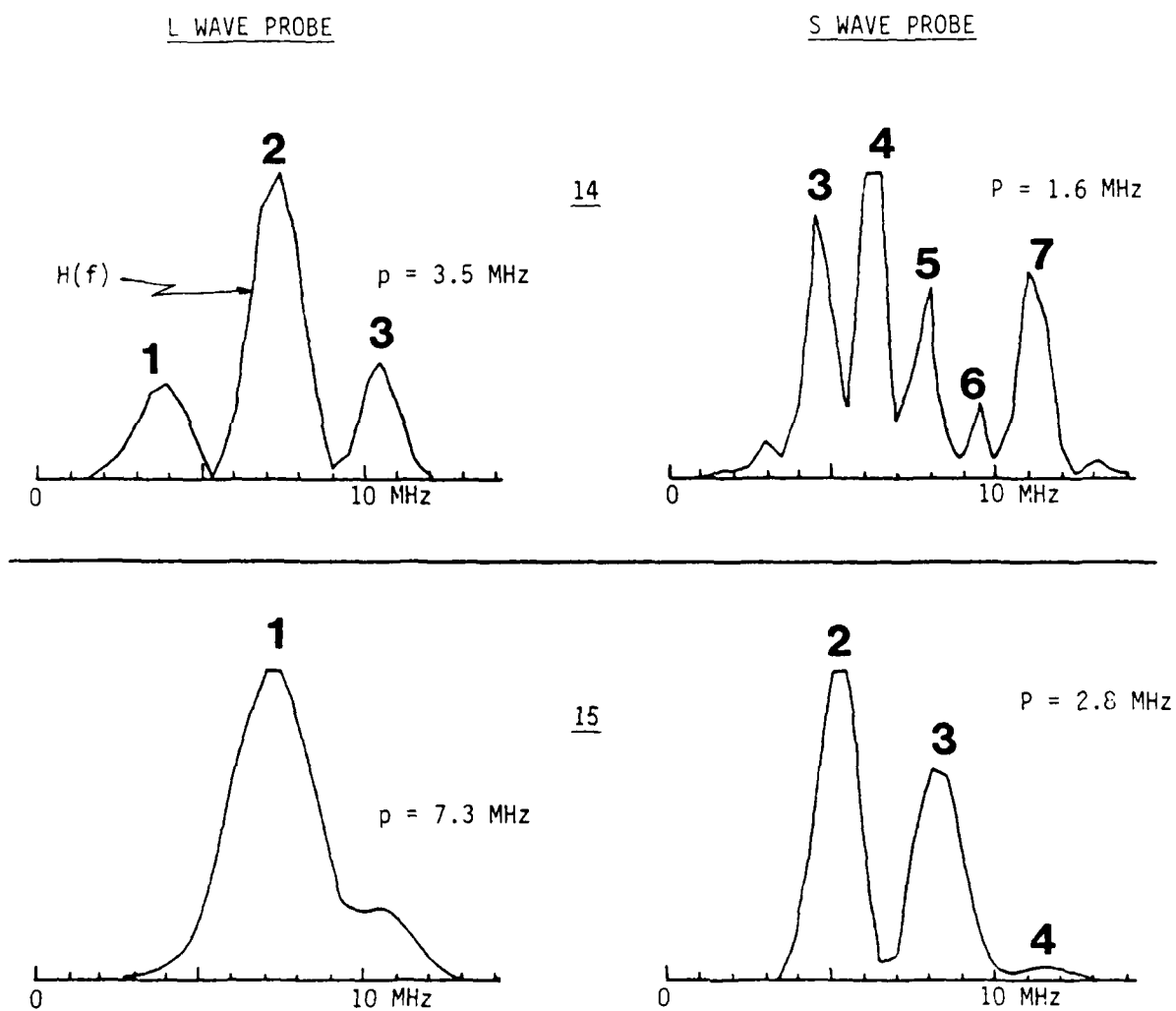
Figure D-2. Longitudinal- and Shear-Wave Profiles of the Inclusions
in Titanium Specimen No. FML 97416 (Flaws 14 and 15)
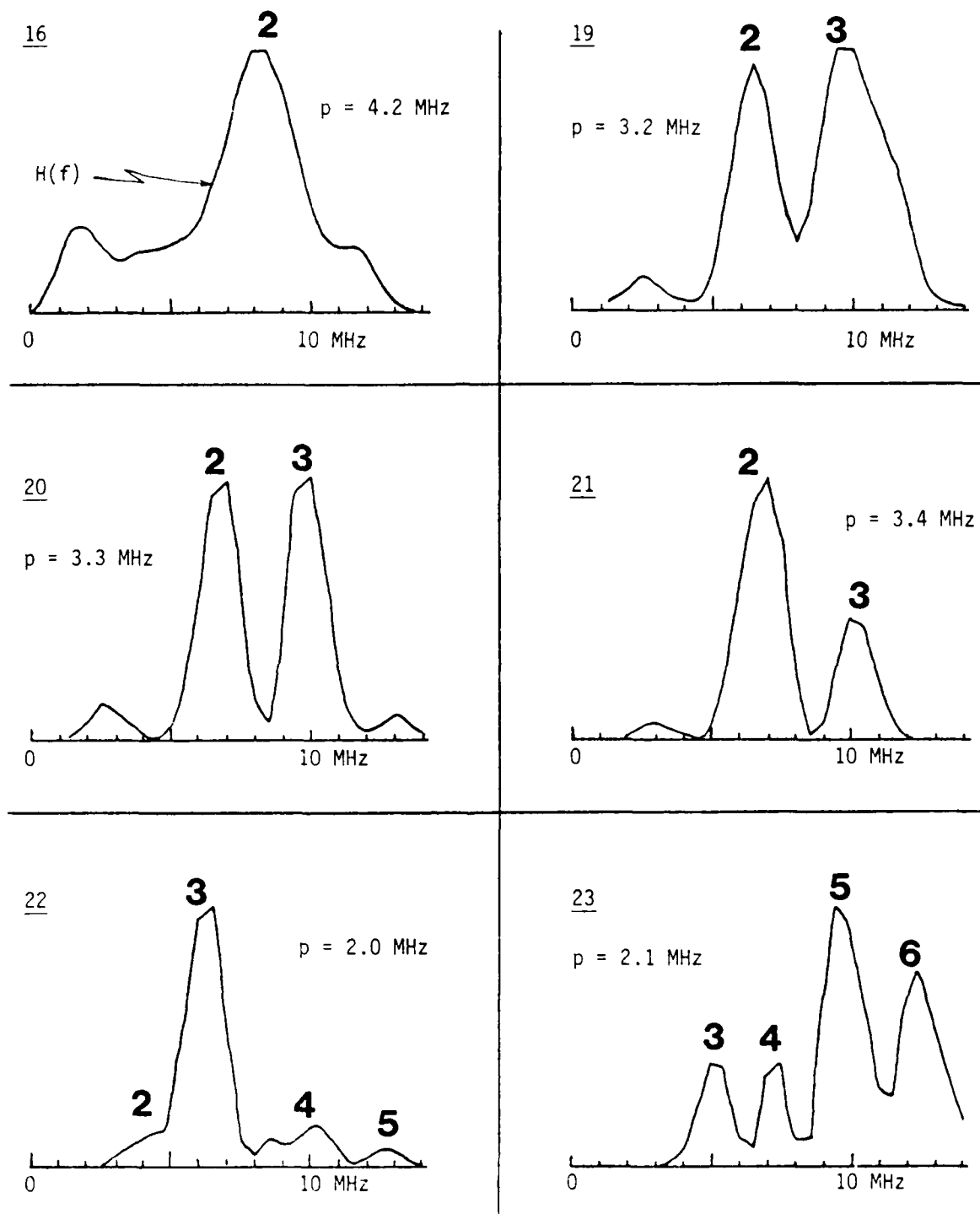
Figure D-3.   Longitudinal-Wave Profiles of the Inclusions in
              IN100 Specimen Nos. FML 97474-1 through -8
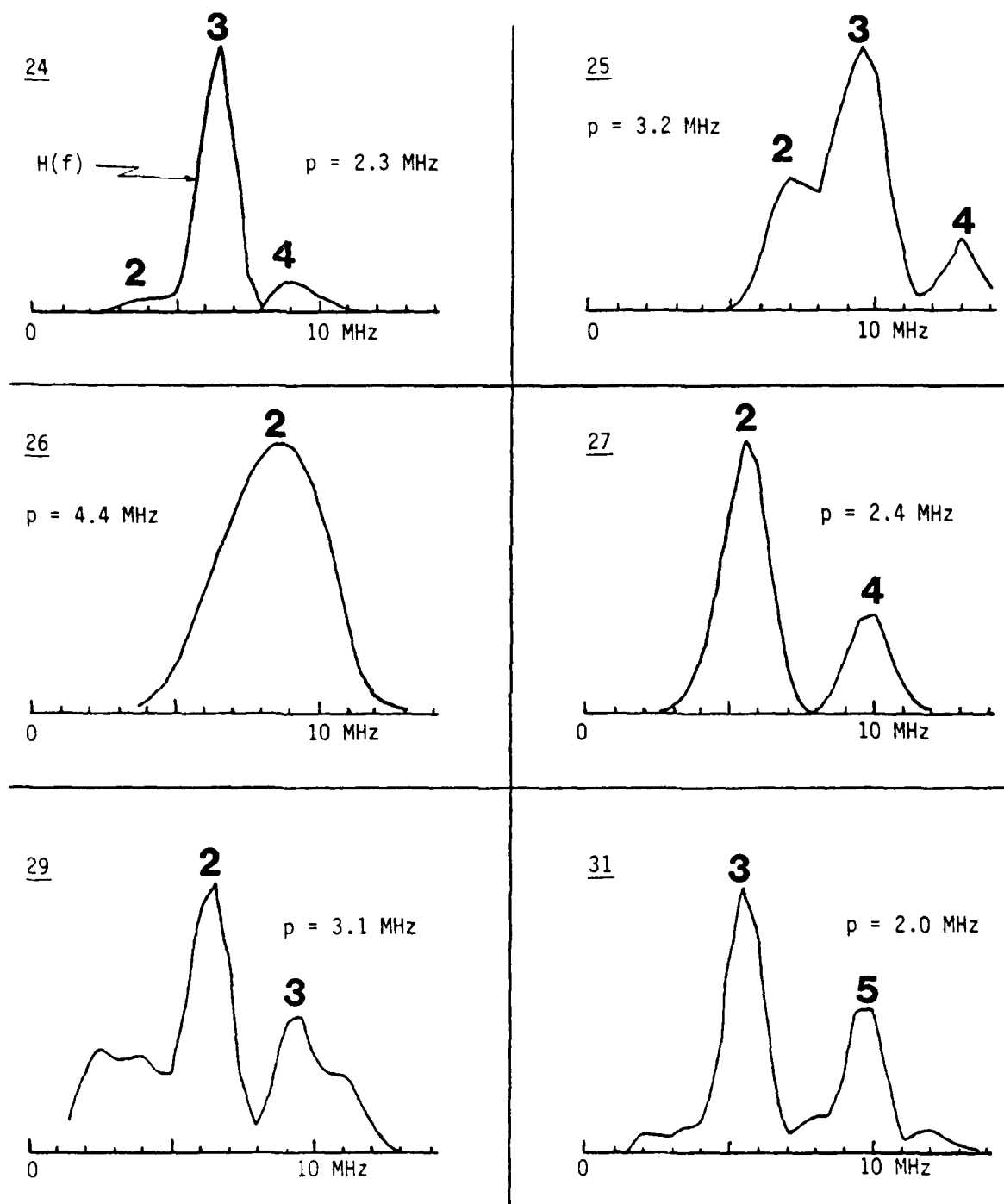   (Flaws 16 through 23)

Figure D-4. Longitudinal-Wave Profiles of the Inclusions
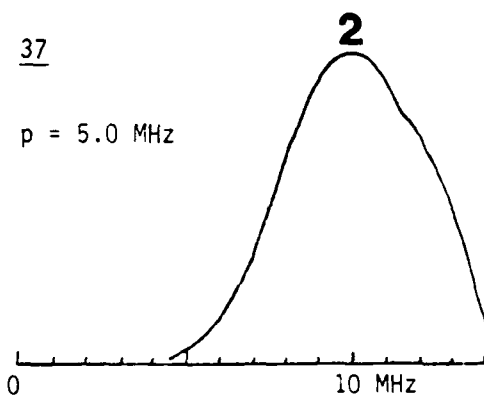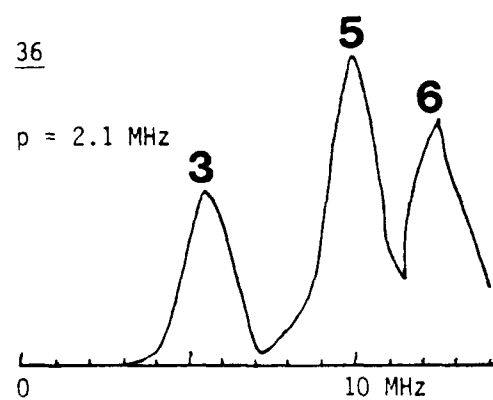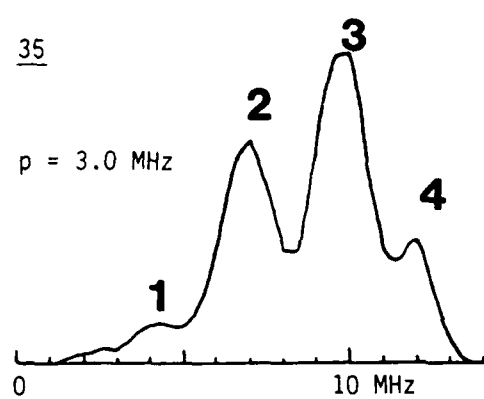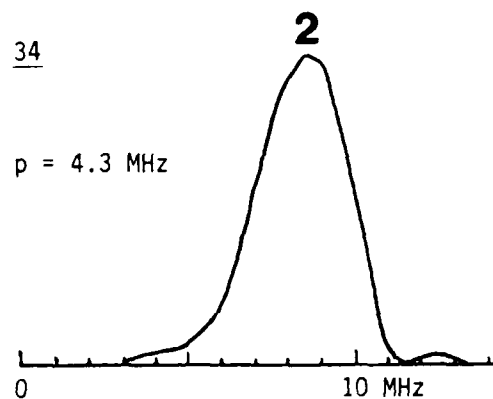in IN100 Specimen Nos. FML 97474-1 through -8
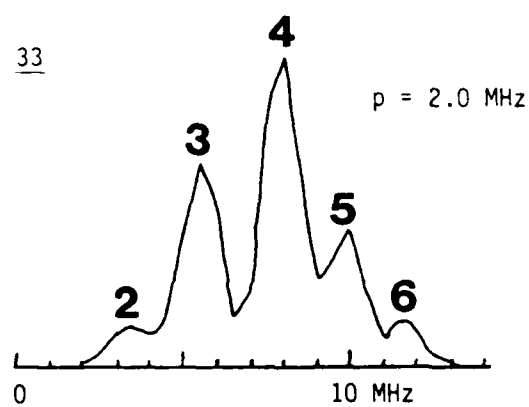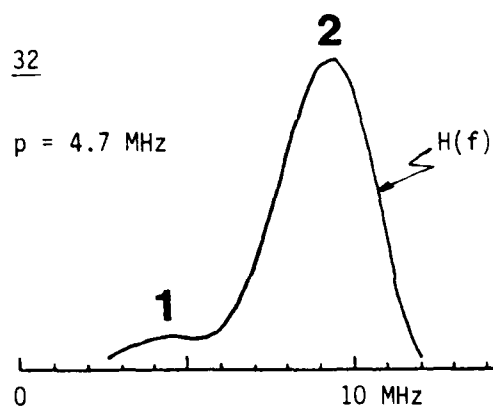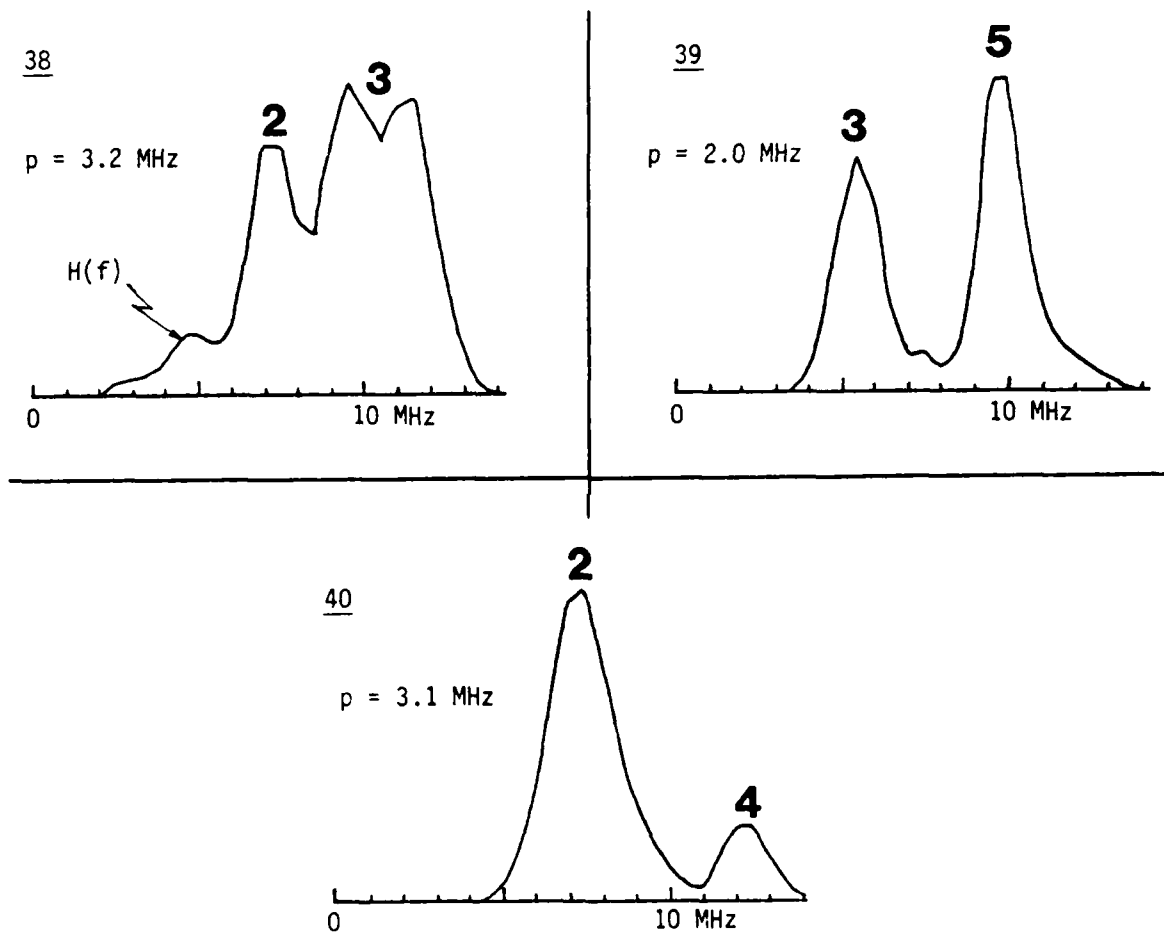(Flaws 24 through 31)

Figure D-5. Longitudinal-Wave Profiles of the Inclusions in IN100 Specimen Nos. FML 97474-1 through -8 (Flaws 32 through 37)

Figure D-6. Longitudinal-Wave Profiles of the Inclusions
in IN100 Specimen Nos. FML 97474-1 through -8
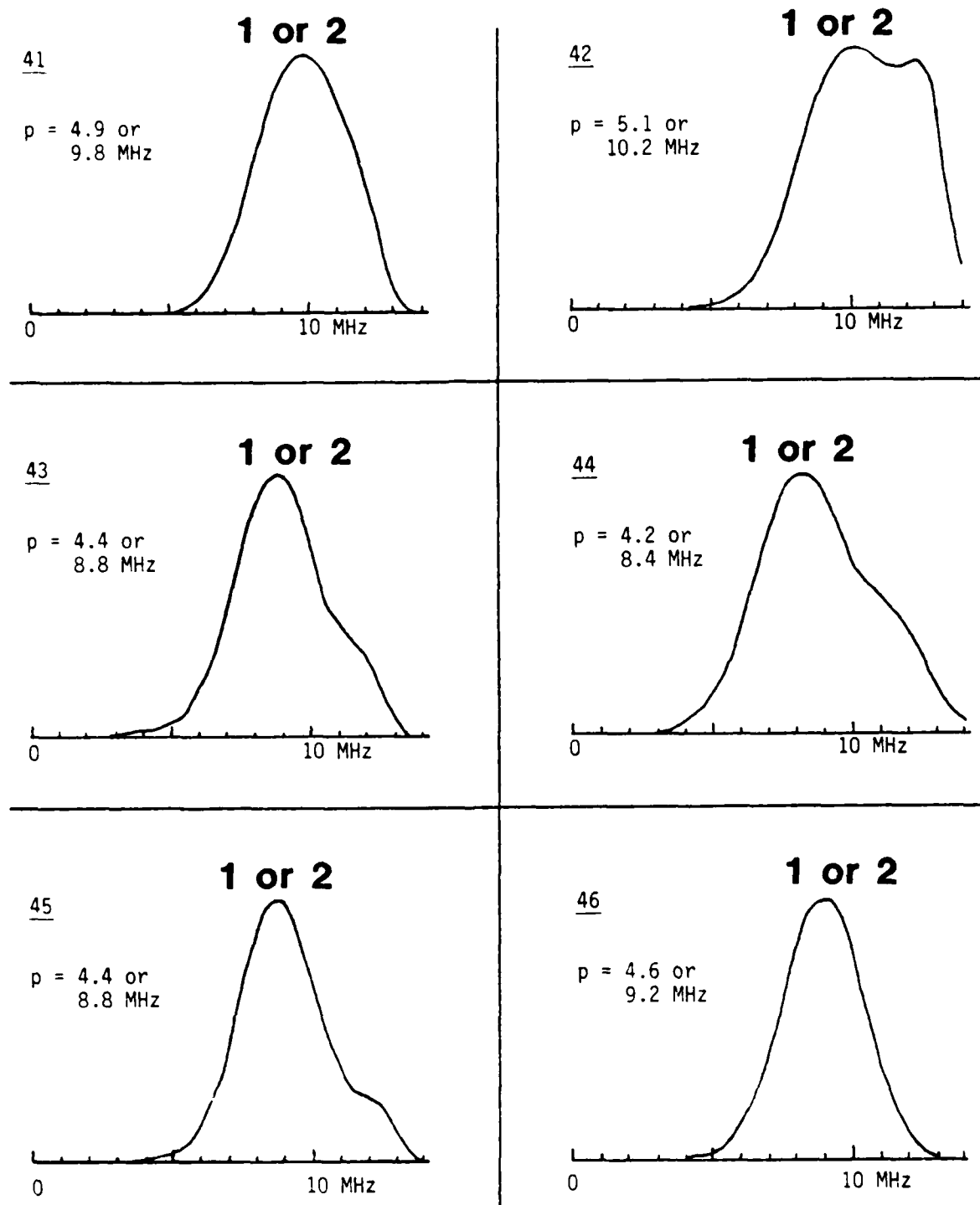(Flaws 38 through 40)

41   **1 or 2**

p = 4.9 or
    9.8 MHz

0   10 MHz

42   **1 or 2**

p = 5.1 or
    10.2 MHz

0   10 MHz

43   **1 or 2**

p = 4.4 or
    8.8 MHz

0   10 MHz

44   **1 or 2**

p = 4.2 or
    8.4 MHz

0   10 MHz

45   **1 or 2**

p = 4.4 or
    8.8 MHz

0   10 MHz

46   **1 or 2**

p = 4.6 or
    9.2 MHz

0   10 MHz

Figure D-7.   Longitudinal-Wave Profiles of the Real Flaws in
IN100 Specimen Nos. FML 97600-1 and -2 (Flaws 41
through 46)

D-8

END

FILMED

8-85

DTIC